

ADA 081241

LEVEL *xy*

(12)
5c



DEVELOPMENT OF THE A-6/CIRCULATION CONTROL WING
FLIGHT DEMONSTRATOR CONFIGURATION

by

Robert J. Englar

DTIC
ELECTE
FEB 27 1980

DDC FILE COPY

APPROVED FOR PUBLIC RELEASE:
DISTRIBUTION UNLIMITED

DTNSRDC/ASED-79/01

January 1979

DAVID
W.
TAYLOR
NAVAL
SHIP
RESEARCH
AND
DEVELOPMENT
CENTER

BETHESDA
MARYLAND
20084

UNCLASSIFIED

SECURITY CLASSIFICATION OF THIS PAGE (When Data Entered)

REPORT DOCUMENTATION PAGE		READ INSTRUCTIONS BEFORE COMPLETING FORM
1. REPORT NUMBER DTNSRDC/ASED-79/01	2. GOVT ACCESSION NO.	3. RECIPIENT'S CATALOG NUMBER
4. TITLE (and Subtitle) DEVELOPMENT OF THE A-6/CIRCULATION CONTROL WING FLIGHT DEMONSTRATOR CONFIGURATION		5. TYPE OF REPORT & PERIOD COVERED Final Report, Sep 1975-Jul 1978
7. AUTHOR(s) Robert J. Englar		6. PERFORMING ORG. REPORT NUMBER
9. PERFORMING ORGANIZATION NAME AND ADDRESS David W. Taylor Naval Ship R&D Center Aviation & Surface Effects Department Bethesda, Maryland 20084		8. CONTRACT OR GRANT NUMBER(s)
11. CONTROLLING OFFICE NAME AND ADDRESS Naval Material Command MAT 08T23 Washington, D.C. 20360		10. PROGRAM ELEMENT, PROJECT, TASK AREA & WORK UNIT NUMBERS Program Element 62241N Task Area ZF 41.221.001 Work Unit 1660-605
14. MONITORING AGENCY NAME & ADDRESS (if different from Controlling Office) 11 Jan 79 12 157		12. REPORT DATE January 1979
		13. NUMBER OF PAGES 148
		15. SECURITY CLASS. (of this report) UNCLASSIFIED
16. DISTRIBUTION STATEMENT (of this Report) APPROVED FOR PUBLIC RELEASE: DISTRIBUTION UNLIMITED		15a. DECLASSIFICATION/DOWNGRADING SCHEDULE
17. DISTRIBUTION STATEMENT (of the abstract entered in Block 20, if different from Report)		
18. SUPPLEMENTARY NOTES		
19. KEY WORDS (Continue on reverse side if necessary and identify by block number) STOL Aircraft A-6 Aircraft High Lift Systems Tangential Blowing Circulation Control Flight Demonstrator Aircraft Boundary Layer Control (CCW)		
20. ABSTRACT (Continue on reverse side if necessary and identify by block number) Wind tunnel investigations were conducted on a 1/8.5-scale model of the A-6/Circulation Control Wing/flight demonstrator aircraft in order to confirm the high lift capability of the concept, to improve lifting and control surfaces and to provide supporting data to assure safety of flight and adequate handling of the full-scale aircraft. The best configuration developed during these investigations produced a 2.2-fold increase in $C_{L_{max}}$ → C sub L max → (Continued on reverse side)		

Accession For	
NTIS GRA&I	
DDC TAB	
Unannounced	
Justification	
By	
Distribution/	
Availability Codes	
Dist.	Avail and/or special
A	

DD FORM 1 JAN 73 1473

EDITION OF 1 NOV 65 IS OBSOLETE
S/N 0102-LF-014-6601

UNCLASSIFIED

SECURITY CLASSIFICATION OF THIS PAGE (When Data Entered)

387695

$$C_{sub L \max}$$

SECURITY CLASSIFICATION OF THIS PAGE (When Data Entered)

over the conventional A-6A high lift configuration. This CCW configuration was compromised to simplify testbed aircraft modifications, reduce construction costs, and provide a larger range of parameters obtainable during flight testing, yet in the final configuration, still provided trimmed aerodynamic CL_{max} double that of the standard A-6A. Additional studies included: Reynolds number and slot height variations, operation in ground effect, stall and stall hysteresis, effect of lifting surface imperfection, additional drag generators, flow field at the tail surface, and longitudinal stability levels with aft c.g. shift. Data from the present flight demonstrator and predict its STOL performance and longitudinal flying qualities.

4

[The page contains several faint, illegible markings and stamps.]

UNCLASSIFIED

SECURITY CLASSIFICATION OF THIS PAGE(When Data Entered)

TABLE OF CONTENTS

	Page
LIST OF FIGURES.....	iv
LIST OF TABLES.....	viii
NOTATION.....	ix
ABSTRACT.....	1
ADMINISTRATIVE INFORMATION.....	1
INTRODUCTION.....	1
TWO-DIMENSIONAL AIRFOIL INVESTIGATIONS.....	3
THREE-DIMENSIONAL MODEL, EXPERIMENTAL APPARATUS AND PROCEDURE.....	5
RESULTS AND DISCUSSION.....	7
LIFTING SURFACE IMPROVEMENT AND ADDITIONAL MODIFICATIONS.....	7
Additional Modifications.....	8
Slot Height Variation.....	10
Reynolds Number Effects.....	12
Coanda Surface Imperfections.....	13
Final Lifting Surface Configuration.....	14
HORIZONTAL STABILIZER DEVELOPMENT.....	14
Wing Downwash and Dynamic Pressure at the Tail.....	15
Phase I Horizontal Stabilizer Development.....	17
Aft Center-of-Gravity Movement.....	18
Phase II Horizontal Stabilizer Modifications.....	19
Phase III Horizontal Stabilizer Modifications.....	20
Phase IV Horizontal Stabilizer Modifications.....	21
Final Horizontal Tail Configuration.....	21
TRIMMED AERODYNAMIC DATA.....	22
GROUND EFFECT.....	25
DRAG GENERATION.....	26
POST STALL AND STALL HYSTERESIS.....	28
SPLITTER FLAP.....	29
LATERAL AND DIRECTIONAL CHARACTERISTICS.....	30
CONCLUSIONS AND RECOMMENDATIONS.....	30

	Page
REFERENCES.....	33
APPENDIX - MODEL, EXPERIMENTAL APPARATUS, AND TECHNIQUE.....	35

LIST OF FIGURES

1 - Basic Circulation Control Aerodynamics and Parameters.....	51
2 - Three-View of the A-6A Aircraft.....	52
3 - Proposed Circulation Control Wing Configurations.....	53
4 - NACA 64A008.4/CCW Two-Dimensional Airfoil Geometry and Parameters.....	54
5 - NACA 64A008.4/CCW Airfoil Static Pressure Distribution at $\alpha_{geo} = 6$ Degrees.....	55
6 - Two-Dimensional Lift Characteristics of the NACA 64A008.4/CCW Airfoil.....	56
7 - 1/8.5-Scale A-6/CCW Model Modifications.....	57
8 - 1/8.5-Scale Model Installed in 8- by 10-Foot North Subsonic Tunnel, Phase I.....	58
9 - Trailing Edge Modification, and Cotton Tuft Showing Jet Turning (Wind Off).....	58
10 - A-6A/CCW Lifting Surface Improvement, Tail Off, $C_{\mu} = 0.263$	59
11 - Details of Wing Flow Fences.....	60
12 - A-6/CCW Tail-Off Aerodynamic Characteristics, Phase I.....	62
13 - Phase II Lifting Surface Modifications.....	63
14 - Slat Leading Edge Radius Increase.....	64
15 - Effect of Increase in Wing Slat Leading Edge Radius.....	65
16 - Conversion to Phase III Lifting Surface Configuration.....	66
17 - Phase III Final Wing Configuration Aerodynamic Characteristics, Tail-Off.....	67

	Page
18 - Comparison of Tail-Off $C_{l_{max}}$ and Stall Angle for Various Configurations.....	68
19 - Lift Augmentation as a Function of Momentum Coefficient.....	69
20 - Phase V Modification to the Wing Trailing Edge.....	70
21 - A-6/CCW Phase II Left Wing Slot Height Expansion.....	71
22 - Momentum Coefficient as a Function of Slot Height, Pressure Ratio, and Dynamic Pressure.....	72
23 - Effect of Slot Height Variation on Lift Coefficient (Phase I).....	73
24 - Effect of Slot Height Variation as a Function of $C_{\mu} V_j / 2V_{\infty}$ (Phase I).....	74
25 - Effect of Variation in Dynamic Pressure and C_{μ} (Phase I).....	75
26 - Effect of Reynolds Number Variation at Constant Momentum Coefficient and Velocity Ratio.....	76
27 - Momentum Coefficient as a Function of Dynamic Pressure and Pressure Ratio (Phase I).....	77
28 - Effect of Slat Step Fairing and Transition Strips.....	78
29 - Effect of Coanda Surface Imperfections (Phase I).....	79
30 - Tufts Showing Downwash Angle in Vicinity of Horizontal Tail, $\alpha_g = 12$ deg, $q = 25$ psf.....	80
31 - Measured Downwash Angle at Horizontal Tail Quarter Chords (Phase I).....	81
32 - Tail Dynamic Pressure Measurement (Phase I).....	84
33 - Horizontal Tail Configurations (Phase I).....	85
34 - Effect of Various Tail Configurations on Pitching Moment (Phase I, $C_{\mu} = 0.10$).....	88
35 - Effect of Various Tail Configurations on Pitching Moment (Phase I, $C_{\mu} = 0.20$).....	89
36 - Tail-Off Pitching Moment for the A-6/CCW Phase I Configuration of Figure 12, but with $X_{cg} = 0.35\bar{c}$	90

	Page
37 - Effect of Aft Center-of-Gravity Shift (Configuration 63, Phase I).....	91
38 - Horizontal Stabilizer Configurations (Phase II).....	92
39 - Horizontal Tail Development, $C_{\mu} = 0.10$ (Phase II).....	93
40 - Horizontal Tail Development, $C_{\mu} = 0.30$ (Phase II).....	94
41 - Horizontal Tail Development (Phase III).....	95
42 - Horizontal Stabilizer Configurations (Phase III).....	96
43 - Horizontal Stabilizer Configurations (Phase IV).....	99
44 - Horizontal Tail Development, $C_{\mu} = 0$ (Phase IV).....	100
45 - Effect of Center-of-Gravity Location on Unblown Longitudinal Stability.....	101
46 - Trimmed CL_{max} and Required Tail Incidence for Optimum Phase I Configuration.....	102
47 - Trimmed Aerodynamic Data for the Final Phase II Configuration.....	103
48 - Lift and Drag Coefficient Variation with Blowing (Phase II).....	104
49 - Tail Incidence Required to Trim Final Phase II Configuration.....	105
50 - Aerodynamic Data for Final Phase III Configuration.....	106
51 - Tail Incidence Required to Trim Final Phase III Configuration.....	108
52 - Trim Lift-to-Drag Ratio for the Final Phase III Configuration.....	109
53 - Effect of Tail Incidence on the Phase IV Configuration, $C_{\mu} = 0$	110
54 - Effect of Tail Incidence on Final Phase IV Configuration Drag Polars.....	111
55 - Trimmed Lift and Drag Data for Final Phase IV Configuration.....	112

	Page
56 - Tail Incidence Required to Trim Final Phase IV Configuration.....	113
57 - Lift-to-Drag Ratio for the Final Phase IV Configuration, Unblown.....	114
58 - Effect of GAC-6RA Tail Deflection on Final Phase V Flight Demonstrator Configuration.....	115
59 - Trimmed Aerodynamic Data for Phase V A-6/CCW Flight Demonstrator Configuration.....	117
60 - Tail Incidence Required to Trim Phase V Flight Demonstrator Configuration.....	118
61 - Trim Lift-to-Drag Ratio for the Phase V Flight Demonstrator Configuration.....	119
62 - Ground Plane Installation in Phase II.....	120
63 - Tuft Photographs of Flow Over Ground Plane in Phase II.....	121
64 - Trimmed Aerodynamic Data for Final Phase II Configuration in Ground Effect.....	123
65 - Ground Effect on Trimmed Maximum Lift for the Final Phase II Configuration.....	125
66 - Ground Effect on Trimmed Lift for Final Phase II Configuration.....	126
67 - Ground Effect on Pitching Moment for Final Phase II Configuration.....	127
68 - Drag Generated by Final Phase I Configuration.....	128
69 - Effects of Landing Gear, Pylons, Stores, and Wing Tip Speed Brakes on Lift (Phase I).....	131
70 - Effects of Fuselage Speed Brakes on Pitching Moments (Phase II).....	132
71 - Post-Stall and Stall Hysteresis Effects on Lift (Phase III).....	133
72 - Post-Stall and Stall Hysteresis Effects on Drag and Pitch, $C_{\mu} = 0.10$ (Phase III).....	134

	Page
73 - Post-Stall and Stall Hysteresis Effects on Drag and Pitch, $C_{\mu} = 0.30$ (Phase III).....	135
74 - Effect of Trailing Edge Splitter Flap on the Final Phase IV CCW Configuration (Yaw Jets Removed).....	136
75 - Comparison of the CCW and Splitter Flap Phase V Configurations.....	137
A.1 - 1/8.5-Scale A-6/CCW Model in Phase I Configuration.....	138
A.2 - 1/8.5-Scale A-6/CCW Model in Phase III Configuration.....	140
A.3 - A-6/CCW Test Setup and Instrumentation.....	143
A.4 - Static Calibration of Slot Height as a Function of Duct Pressure (Phase I).....	144
A.5 - Coanda Nozzle Efficiency (Phase I).....	145
A.6 - Measured and Isentropic Weight Flow as Functions of Slot Height and Pressure Ratio.....	146

LIST OF TABLES

1 - Geometric Characteristics of the Grumman A-6A.....	40
2 - Phase I Test Program Summary.....	43
3 - Phase II Test Program Summary.....	46
4 - Phase III Test Program Summary.....	47
5 - Phase IV Test Program Summary.....	48
6 - Phase V Test Program Summary.....	49
7 - 1/8.5-Scale A-6/CCW Model Trailing Edge Parameters, Blowing Off.....	50

NOTATION

A_j	Jet slot area
B.L.	Butt line, spanwise distance from aircraft centerline
b	Wing span
b'	Spanwise distance along slot from end
b_T	Horizontal tail span
C, c	Wing chord length
C_D, C_d	Aircraft or section drag coefficient
C_{DE}	Aircraft equivalent drag coefficient, $C_D + C_\mu$
C_L, C_ℓ	Aircraft or section lift coefficient
C_{M_x}, C_{m_x}	Aircraft or section pitching-moment coefficient; x subscript indicates moment center in fraction of MAC
C_{noz}	Slot nozzle coefficient, $\dot{m}_{meas}/\dot{m}_{calc}$
C_P	Pressure coefficient, $(P-P_\infty)/q$
C_R	Chord at wing or tail root
C_T, \bar{C}_T	Horizontal stabilizer chord and MAC
C_{TE}	Chord of horizontal stabilizer extended trailing edge
C_{TIP}	Chord at wing or tail tip
C_μ	Jet momentum coefficient
\bar{c}	Wing mean aerodynamic chord (MAC)
F.S.	Fuselage station, horizontal distance aft of aircraft nose
h	Jet slot height
h_{AV}	Jet slot height at mid-slot
h_g	Distance of aircraft center of gravity above ground when $\alpha = 0$ deg
i_s, i_s	Horizontal stabilizer incidence

L/D	Aircraft lift-to-drag ratio
ℓ_H	Horizontal distance from wing to horizontal stabilizer 0.25 MAC points
ℓ_V	Horizontal distance from wing to vertical stabilizer 0.25 MAC points
\dot{m}	Jet mass efflux
P	Static pressure
P_d, P_D	Plenum (duct) total pressure
P_{D_2}	Total pressure at middle of left wing plenum
P_∞	Freestream static pressure
q	Freestream dynamic pressure
q_T	Dynamic pressure at the horizontal tail (stabilizer)
q_u	Tunnel uncorrected dynamic pressure
R, r	Leading or trailing edge radius
R	Universal gas constant
R_e	Reynolds number based on MAC
S	Wing planform area
T_d	Plenum (duct) total temperature
T_j	Jet static temperature
V_j	Isentropic jet velocity
V_S, V_{STALL}	Aircraft stall velocity
V_∞	Freestream velocity
$W.L.$	Waterline station
$W.S.$	Wing station, distance from aircraft centerline
\dot{w}	Jet slot weight flow
x	Longitudinal distance from leading edge or nose

x_{cg}	Center-of-gravity distance aft of leading edge
y	Spanwise distance from aircraft centerline
α	Corrected angle of attack
α_g, α_{GEO}	Geometric uncorrected angle of attack
α_{STALL}	Stall angle of attack
α_T	Angle of attack at the horizontal tail (stabilizer)
β	Angle of sideslip
γ	Ratio of specific heats
δ_f, δ_{FLAP}	Flap deflection angle
δ_{rud}	Rudder deflection angle
δ_s, δ_{SLAT}	Slat deflection angle
δ_{SP}	Spoiler (flaperon) deflection angle
δ_{TE}	Deflection angle of horizontal stabilizer trailing edge extension
ϵ	Downwash angle or tunnel blockage correction factor
ρ	Jet or freestream density
ψ	Angle of yaw
Subscripts	
av	Average value
calc	Calculated isentropic value
max	Maximum value
meas	Measured value
nom	Nominal value
TRIM	Trimmed value, $C_M = 0$

ABSTRACT

Wind tunnel investigations were conducted on a 1/8.5-scale model of the A-6/Circulation Control Wing flight demonstrator aircraft in order to confirm the high lift capability of the concept, to improve lifting and control surfaces and to provide supporting data to assure safety of flight and adequate handling of the full-scale aircraft. The best configuration developed during these investigations produced a 2.2-fold increase in $C_{L_{max}}$ over the conventional A-6A high lift configuration. This Circulation Control Wing configuration was compromised to simplify testbed aircraft modifications, reduce construction costs, and provide a larger range of parameters obtainable during flight testing, yet in the final configuration, still provided trimmed aerodynamic $C_{L_{max}}$ double that of the standard A-6A. Additional studies included: Reynolds number and slot height variations, operation in ground effect, stall and stall hysteresis, effect of lifting surface imperfection, additional drag generators, flow field at the tail surface, and longitudinal stability levels with aft center-of-gravity shift. Data from the present studies should provide an adequate base upon which to construct the full-scale flight demonstrator and predict its STOL performance and longitudinal flying qualities.

ADMINISTRATIVE INFORMATION

The work represented by the studies reported herein was funded by the Naval Material Command (MAT 08T23) under Program Element 62241N, Task Areas WF41.421.20Z, WF41.421.091, ZF41.400.001, and ZF41.421.001 and David W. Taylor Naval Ship Research and Development Center (DTNSRDC) Work Units 1660-600, 1660-601, and 1660-605. The two-dimensional wind tunnel investigations were conducted during September and November of 1975. The A-6/Circulation Control Wing investigations were conducted in five phases: Phase I - December 1975 through February 1976; Phase II - March through April 1976; Phase III - December 1976 through February 1977; Phase IV - June through July 1977; Phase V - June through July 1978.

INTRODUCTION

In response to the current interest in Short Takeoff and Landing (STOL) and Vertical/Short Takeoff and Landing (V/STOL) aerodynamics, a number of powered lift concepts are undergoing development in the aerospace community

in an attempt to derive maximum lifting benefits from various combinations of advanced lifting surfaces augmented by engine bleed or thrust. Many of these concepts are quite complex; and while they might be successfully integrated into such aircraft as advanced STOL transports, they are often not compatible with high performance fighter and attack configurations. A more feasible concept for these aircraft is a high lift system which can be simply incorporated into conventional wing trailing edge structure and powered by bleed air from existing turbine engines without major modifications or relocation. Technology developed at DTNSRDC since 1968 has led to the Circulation Control Wing (CCW), a STOL high lift concept offering this potential.^{1-5*}

The basic aerodynamics of the circulation control concept involve the adherence of a thin tangentially ejected jet sheet to the rounded trailing edge of an otherwise conventional airfoil. This phenomenon, frequently identified as the Coanda effect, is produced by a balance of centrifugal force and reduced static pressure in the jet sheet, shown schematically in Figure 1. Lift augmentation due to boundary layer control occurs at lower blowing coefficients (C_μ); $\Delta C_L / C_\mu$ can be as high as 70 for C_μ of 0.05 or less. However, high lift capability is achieved due to supercirculation, where control of the airfoil stagnation points by the jet sheet produces lift coefficients considerably higher than those predicted by potential flow. Due to the lack of a sharp trailing edge and the associated Kutta condition, this circulation control is achieved at lower momentum coefficients than the somewhat similar tangentially blown flap (see References 3 and 6 for comparison). Although the CCW does not generate the same ultra-high lift coefficient as those concepts which employ large vertical thrust components (such as jet flaps, upper surface blowing, and externally blown flaps), the concept is promising for high performance fighter and attack aircraft where available C_μ may be low and where engine placement on or below the wing is not practical.

Based on the potential of the Circulation Control Wing and the more than doubling of $C_{L_{max}}$ produced by the CCW on a three-dimensional aircraft

*A complete listing of references is given on page 33.

configuration during earlier investigations,^{2,5} a flight test program is being undertaken to demonstrate the STOL performance of the concept on a full-scale testbed aircraft. The Grumman A-6A (Figure 2 and Table 1.) was chosen as the flight demonstrator because of the excellent aerodynamic configuration, relative simplicity of trailing edge modifications, availability of a test aircraft, twin engines with additional bleed ports available, and predicted STOL performance gains with CCW. Goals of the program are (1) to demonstrate maximum obtainable lift augmentation from the CCW powered by bleed air, (2) to evaluate stability, control, and handling characteristics in the STOL regime, and (3) to develop the technology to the point of reducing the risk of application to future STOL configurations. The present wind tunnel investigations were undertaken to develop the lifting surface and to provide the supporting trim, stability, control, and handling data to assure safety in flight of the A-6/CCW flight demonstrator.

TWO-DIMENSIONAL AIRFOIL INVESTIGATIONS

A two-dimensional (2-D) model of the A-6 wing-fold-line airfoil section (NACA 64A008.4 Modified) was constructed for wind tunnel investigation to optimize both leading and trailing edge parameters for maximum lift augmentation prior to modification of a three-dimensional model. In order to convert the sharp trailing edge of the cruise airfoil into the rounded trailing edge, a number of configurations were considered, as shown in Figure 3. The extended configuration appeared least complicated in terms of a bolt-on, fixed deployment modification for the demonstrator aircraft. In addition, the extended configuration displayed a slight chord increase when deflected rather than the chord loss of the rotating flap configuration. The 25.025-in. airfoil section shown in Figure 4 was constructed with a 3-ft span and installed in a 3- x 8-ft two-dimensional test section inserted in the DTNSRDC 8- x 10-Foot South Subsonic Wind Tunnel. Trailing edge slot-height-to-chord and radius-to-chord ratios shown in the figure are based on values found to be quite effective on similar airfoils.¹⁻⁵ Lift and pitching moment were determined by static pressure integration at the model centerline; drag was measured by wake rake one chord length

downstream of the trailing edge. Data were nondimensionalized in the 2-D investigations by the undeflected cruise chord C , corresponding to the undeflected planform areas S in the three-dimensional investigations. Two-dimensionality was controlled by tangential blowing from the tunnel walls using test techniques very similar to those employed in References 4 and 7. However, incidence shown in the present two-dimensional data has not yet been corrected for the induced downwash due to slight three-dimensionality, as discussed in Reference 7. The effective incidence, therefore, should be reduced by approximately the increments shown in Figure 24 of Reference 4. Variations in slat gap, slat angle, jet slot height, trailing edge shape, airfoil incidence, and momentum coefficient were conducted to determine leading and trailing edge parameters required for maximum lift augmentation.

A characteristic "saddle-back" pressure distribution is shown in Figure 5 for geometric incidence of 6 deg. The very high suction peak downstream of the slot is typical of the CCW airfoil, and the high section C_l results from the supercirculation induced by blowing. Figure 6 presents lift as a function of blowing and geometric incidence for the airfoil at a velocity of approximately 155 to 160 ft/sec ($q = 30$ psf) and Reynolds Number of 1.9×10^6 . A lift coefficient of almost 6.5 was achieved by the airfoil with 37.5-deg slat deflection, but was limited at higher incidences due to upper surface flow separations on both the slat and main airfoil. This was corrected on the main airfoil by the addition of the small radius (see Figure 4) to the lower surface of the airfoil so that the sharp corner just aft of the slat gap was eliminated. Separation on the slat was controlled somewhat by additional deflection, but net lift was not greatly improved due to the reduction in the vertical force component on the slat as it was tilted forward. An increase in slat leading edge radius should eliminate the flow separation. Note that the lift performance of the A-6/CCW airfoil (only 8.4 percent thick) is very similar to the 64A-212/CCW airfoil in Reference 4 as long as flow separation does not occur. High lift generation appears to be more a matter of leading edge flow control under this high supercirculation than basic airfoil characteristics aft of the leading edge. The above results were sufficiently high to warrant modification of a three-dimensional model with the trailing edge parameters of the two-dimensional model and provisions for additional leading edge investigations.

THREE-DIMENSIONAL MODEL, EXPERIMENTAL APPARATUS, AND PROCEDURE

A 1/8.5-scale model of the A-6A, as tested in Reference 8, was borrowed from Grumman Aerospace Corporation and the wing was modified to resemble the two-dimensional CCW section. The airfoil sections varied from NACA 64A009 MOD at Wing Station (WS) 33.0 (approximately the wing-body juncture), to NACA 64A005.9 MOD at the wing tip. The original semi-Fowler flap was replaced with the rounded CCW trailing edge, which covered the same span as the flap--from WS 55.5 to WS 270.0. Figure 7 shows the basic model layout, including some additional modifications made to the wing leading edge and horizontal stabilizer in later portions of the program. Geometric characteristics of the full-scale A-6A are given in Table 1. A detailed description of the model design rationale, modification, test procedure, and data reduction is provided in the Appendix.

The model was mounted on a single point strut at Fuselage Station 260.4 (0.253 τ) on the centerline of the 8- x 10-Foot North Subsonic Wind Tunnel. Figure 8 shows this installation, the air supply lines, engine inlet and exhaust fairings, the standard horizontal stabilizer, and some long tufts used for preliminary flow visualization. Additional trailing edge detail, inboard and outboard flow fences, and cotton tufts showing the turning of the jet sheet are shown in Figure 9. A turning angle of more than 180 deg from the slot was achieved, and sufficient energy remained in the jet so that it carried forward on the lower surface to the slat gap, turned the corner there, and exited onto the upper surface of the wing. Although this photo is taken without tunnel freestream velocity, the capability of the jet to influence wing circulation is apparent.

Over 760 hours of wind tunnel investigations were conducted in five phases to confirm the CCW potential on the A-6 and to provide a data base for the flight test. The basic objectives of each phase are listed below, with detailed test programs provided as Tables 2, 3, 4, 5, and 6.

PHASE I

- Lifting surface development; Reynolds number and slot height variation; and tail-off lift, drag, and pitch data.
- Horizontal tail improvement for longitudinal trim; trimmed force data.

- Effects of landing gear, pylons, external fuel tanks, wing tip drag brakes.
- Lateral directional characteristics including spoiler and rudder power at zero sideslip, and sideslip effects.

PHASE II

- Wing and horizontal stabilizer simplification to reduce modification cost; tail-off and trim data for simplified configuration.
- Effects of fuselage drag brake deflection.
- Operation in ground effect.
- Spoiler and rudder power at sideslip angle.

PHASE III

- Further wing simplification and horizontal tail development to yield final flight test wing configuration and associated tail-off and trim data.
- Extended α range (to post-stall); stall hysteresis.
- Rudder and spoiler deflection through post-stall incidence.

PHASE IV

- Further development of horizontal stabilizer for blowing-off flight test configuration; trim force data.
- Rudder power at high stabilizer deflections.
- Fairing for air supply ducting.

PHASE V

- Conversion to final wing configuration as necessitated by financial and construction limitations.
- Additional lateral and directional data for final flight test configuration.
- Effect of short chord splitter flap to reduce drag for takeoff configuration.

Note that Phases II, III, IV, and V were, in most cases, attempts to (1) simplify or reduce the cost of modifications on the flight demonstrator aircraft, (2) improve performance or obtain additional stability and control data, and (3) add to data pertaining to aircraft safety of flight. The whole series of tests will provide the data base upon which aircraft flight clearance will depend.

RESULTS AND DISCUSSION

LIFTING SURFACE IMPROVEMENT AND ADDITIONAL MODIFICATIONS

The initial wing configuration maintained essentially the same trailing edge parameters as the 2-D section shown in Figure 4. Actual slot height and trailing edge radius varied along the span so that the ratios h/r and r/c remained constant across the tapered planform at 0.03086 and 0.03623, respectively. This produced an average slot height and radius midway between wing stations 55.5 and 270.0 of $h_{av} = 0.0156$ in. and $r_{av} = 0.5047$ in. at $c_{av} = 13.930$ in. This configuration was expected to provide strong lift augmentation, with some improvement needed in the leading edge parameters to increase performance at higher incidence. Results of variations in the leading edge characteristics are seen in Figure 10 for a sample C_μ of 0.263. A serious separation problem produced stall between 4 and 6-deg angle of attack and was not affected by variation in slat angle, gap, or leading edge radius (Configurations 3, 4, 7, 8 and 11). Tuft studies showed a strong vortex originated at the glove located at the wing-body juncture (Figure 7) and produced strong flow separations both aft of the glove and at the outboard edge of the slat. Removal of a sharp leading edge strake which existed on the glove produced a significant improvement (Configuration 13), and additional rounding, deflection or addition of a Kruger flap to the glove (Configurations 14, 20, 28, and 39) showed continued elimination of separation and vorticity. Removal of conventional flow fences and the addition of those fences shown in Figure 9 also aided by controlling spanwise flow; see Figure 11 for fence details. Including these fences and some variation in slat gap, Figure 10 shows increases in $C_{L_{max}}$ from 3.1 to 4.6 and α_{stall} from 4 to 20 deg obtained solely by improving the leading edge and glove geometry. Figure 12 shows the tail-off lift, drag, and pitching moment coefficients for the best of the above configurations (Configuration 39) as functions of blowing and incidence, along with a comparison with the standard A-6A, tested tail-off in its landing configuration (30-deg flap and 25-deg slat deflections)⁸. With this blown wing configuration, $C_{L_{max}}$ can be increased by a factor of 2.2 at $C_\mu = 0.30$. Analysis of the bleed airflow available from the A-6's

J-52-P-8B engines indicates that C_μ greater than 0.30 will not be available on the full-scale flight demonstrator aircraft. For this reason, $C_\mu = 0.30$ is considered an upper limit on momentum coefficient for the remainder of these studies.

Additional Modifications

Although Configuration 39 was the optimum of the initial investigation, during considerations of full-scale aircraft modification a number of changes were deemed necessary in the lifting surface design in order to (1) reduce modification cost, (2) simplify the configuration, (3) further increase lifting performance, and (4) conform to existing wing structures and predicted mass flows. At the initiation of the Phase II investigation, the following changes were made to the slat, fences, and blowing slot of the final Phase I configuration:

- Slat angle was reduced from 37.5 to 25 deg; the 0.02c gap was retained.
- Slot length was shortened from 25.59 to 25.24 in. as outboard termination was moved from WS 270.0 to WS 267.0 to avoid fuel dump nozzle.
- Outboard flow fence was moved inboard from WS 270.0 to WS 267.0.
- Flap track louvers were added to wing upper surface at 0.83c to duplicate the actual aircraft.
- Slot height for both the Phase I and II configurations was reduced from the Configuration 39 value $h/r = 0.0309$ ($h_{av} = 0.0156$ in.) to $h/r = 0.0231$ ($h_{av} = 0.0117$ in.) to accommodate expected full-scale mass flows and pressures on the test aircraft.

The results of these changes are seen in Figure 13, where the primary difference is an increase in $C_{L_{max}}$ of 0.2 to 0.3 for the blown cases. The shortened slot span and inboard fence movement should have produced a decreased blown aspect ratio, which in conjunction with the flow disturbances produced upstream of the slot by the track louvers should have reduced lifting capability at constant C_μ . The net increases then must be attributed to the increased vertical force component produced on the slat at the reduced deflection. Maintenance of flow attachment is due to the increase in slat leading edge radius, Figure 14, as verified in Figure 15.

This rounded leading edge was also present on the slat for Configuration 39 and the final Phase I configuration in Figure 13. Thus, the 25-deg slat deflection which exists on the actual aircraft can adequately prevent flow separation at higher incidence and blowing as long as the increased leading edge radius is retained.

In Phase III, two additional simplifications to the lifting surface were made. The inboard flow fence at WS 55.5 was removed as were the gap radius and ramp on the main airfoil just aft of the slat gap; see Figure 4. As Figure 16 shows, removal of the inboard fence reduces $C_{L_{max}}$ by about 0.25 or less, while removal of the gap radius and ramp restores a portion of this but produces up to a 2-deg loss in stall angle. Tail-off lift, drag, and pitching moment coefficients are presented in Figure 17, and when compared in Figure 18 to the Phase I optimum configuration show the effects of configuration compromise due primarily to goals of simplification and cost reduction. For momentum coefficients greater than 0.075, the Phase III loss in $C_{L_{max}}$ increases with C_{μ} , to a maximum loss of 0.47 at $C_{\mu} = 0.30$, since the simplifications made are most detrimental at higher blowing. However, for $C_{\mu} < 0.075$, the latter configuration shows increases of up to 0.1 in $C_{L_{max}}$ and up to 3 deg in stall angle over the Phase I configuration as blowing decreases. This trend is further revealed in Figure 19 where lift augmentation is compared at zero incidence. In either case, increases in $C_{L_{max}}$ by a factor of 2 or more over the standard A-6A in landing configuration are generated.

Note that Figures 12 and 17 are not exactly comparable in that the engine inlet and exhaust fairing plugs of Phase I were removed for Phases II, III, IV, and V. Furthermore, Figures 12, 13 and 16 are not directly comparable due to differences in horizontal stabilizers, as shown in the section Horizontal Stabilizer Development.

Phase IV involved no changes in the wing; however, during construction of the actual flight test aircraft, a number of additional changes were necessitated due to structural or construction limitations. These changes were investigated in Phase V and include the following:

- Add small heat shield at inboard slot end (WS 56.09) to protect fuselage skin from jet sheet temperatures.

- Shorten slot to 24.986 in. and move outboard slot end and fence in to WS 265.5.
- Add support structure to base of outboard fence.
- Modify wing plenums by reducing nozzle entrance angle and installing screws nearer to slot.
- Add wing pylons at the wing fold station, WS 144.
- Add external crossover bleed air ducts to fuselage and wing.
- Add air conditioner inlet scoop on right wing Kruger flap upper surface.
- Reduce slot height to $h/r = 0.01406$ or $h_{av} = 0.0071$ in.
- Add yaw-control jet thrusters at WS 259.25 (unblown initially).

Details of the modified plenum and nozzle plus the yaw-control jets are shown in Figure 20. (The splitter flap shown was tested in a later portion of this investigation and is discussed on page 29.) The tail-off maximum lift coefficients and stall angles are compared to the Phase I and III configurations in Figure 18. Whereas the maximum lift coefficients show negligible variation from those of the final Phase III tail-off configuration, the combined effect of wing pylons and air conditioning inlet scoop produced a small reduction in stall angle (1.2 deg at most).

Slot Height Variation

Actual slot height on the flight test configuration will be a function of the available mass flow, pressure, and temperature delivered to the wing plenum from engine bleed, and as these were undetermined at the time, variation in the slot height was investigated. These effects have been investigated on similar circulation control airfoils, and for a constant momentum coefficient and airfoil incidence, a reduction in slot height produces an increase in lift due to the increased energy and turning of the jet.^{4,9,10} However, limits were found where, depending on the model and blowing rates, too small a slot height could reduce the lift at constant C_μ and incidence.

In Phase I of the present tests, 3 slot heights were investigated. Table 7 lists these slot heights and the resulting trailing edge parameters. The slot height values are nominal for the no-blowing case. Figure 21 shows that for the $h/r = 0.023143$ ($h_{av} = 0.0117$ in.) data of Phase II, slot height

expansion under pressure ratios up to 4.4 produced as much as a 75-percent increase in average slot height over the nominal value. This increase is due to the thin upper surface slot lip (see Figure 4) required to allow smooth undisturbed flow from the airfoil upper surface into the jet region and by the placement of the support screws well ahead of the slot to prevent flow distortion in the jet throat. Figure 22 presents momentum coefficients obtained for the three slot heights of the Phase I investigations as a function of pressure ratio. Slot expansion under pressure is similar to Figure 21, with the exception of a somewhat higher expansion rate for the smallest slot, $h_{av} = 0.0078$ in. Figure 23 presents variations in lift coefficient with slot height at a constant geometric incidence of 4 deg. As seen in previous investigations, at constant low values of C_μ , the smaller slot heights are slightly more effective due to additional energy in the jet; but at higher values of C_μ , crossovers occur in the curves and the small slot heights prove less effective. The net difference in lift coefficient between the smallest and largest slot height is never more than 0.1. Although the effect thus appears minor, it is perhaps more meaningful to compare the data at constant values of kinetic energy in the jet, or power required to produce that energy:

$$K.E. = 1/2 \dot{m} V_j^2$$

$$Power = \frac{\Delta KE}{\Delta t} = \frac{\Delta \dot{m} V_j^2}{2 \Delta t} = 1/2 \dot{m} V_j^2$$

or non-dimensionalized

$$\frac{Power}{q S V_\infty} = \frac{\dot{m} V_j^2}{2 q S V_\infty} = C_\mu \frac{V_j}{2 V_\infty}$$

Then, as Figure 24 shows, for constant values of this parameter, increased slot height produces slightly greater C_L over the entire range of jet velocity. Again, the difference between largest and smallest slot heights

is minimal, but the trend is toward reduced lift with smaller slot heights. It is therefore advisable to adopt the lower limit on h/c of 0.0005, as discussed in Reference 4.

Reynolds Number Effects

While the majority of the present investigations were run at a free-stream dynamic pressure of 25 psf and Reynolds number (based on $\bar{c} = 1.282$ ft) of 1.2×10^6 , the effect of varying Reynolds number was desired in order to allow data extrapolation to the full-scale flight demonstrator. The area of primary interest is, of course, $C_{L_{max}}$; however, as discussed in Reference 2, setting an incidence near the unknown stall incidence while retaining constant C_μ over a range of dynamic pressures can produce effective corrected incidence beyond stall due to tunnel interference effects (see the Appendix). Thus, a lower angle of incidence was used to conduct the study. Figure 25 shows effects of varying dynamic pressure from 5 to 30 psf (R_e from 0.54 to 1.30×10^6) at 4-deg geometric incidence. For $C_\mu \leq 0.18$, an increase in dynamic pressure at constant momentum coefficient produces increased C_L ; but for $C_\mu > 0.18$, the crossplotted data of Figure 26 show a slight reduction in C_L at increased R_e . This apparent abnormality is explained by the fact that the effect of Reynolds number alone cannot be distinguished from the effects of increasing the pressure ratio (or jet velocity) to maintain constant C_μ at increased q . Figure 25 shows that a constant pressure ratio of 1.5 can vary C_μ from 0.279 to 0.047 for q ranging from 5 to 30 psf. Figure 27 shows C_μ as a function of q and pressure ratio. Apparently, increase in pressure ratio can produce a knee in the $C_L - C_\mu$ curve beyond which lift augmentation is somewhat reduced. For the present configuration, that point for each curve of Figure 25 is denoted on both Figures 26 and 27; the locus of points appears to fall in a pressure ratio band between 2.4 and 2.6, and coincides with the dropoff in C_L with increased q at higher C_μ in Figure 26. These lift losses are small, 0.10 or less in C_L for $C_\mu \leq 0.30$, the range of interest for the flight demonstrator, but they may reconfirm the data of Figure 24 which tends to favor a larger slot and reduced pressure ratio over the entire C_μ range of interest.

Whereas the Reynolds number effect is not resolved by the above data, Figure 28 presents the effects of boundary layer transition devices and

implies the effects of higher Reynolds number. The wing of the A-6 has a forward-facing step at the 15-percent chord location into which the trailing edge of the slat retracts at zero deflection. For data through Configuration 38, this step was faired over; however, on Configuration 39 it was unfaired and returned to its production shape. The result was a slight decrease in C_L at constant α , but a slight increase in $C_{L_{max}}$, characteristic of the usual expected increase with Reynolds number. For Configuration 40, saw-toothed leading edge transition strips of tape were placed at the 5-percent chord location on the slat, glove, and vertical tail, and around the fuselage circumference at Fuselage Station 120 (14.1 in. from the nose of the model). The results were the reverse of before--an increase in C_L at constant α but a slight reduction in $C_{L_{max}}$ and α_{stall} . The strips apparently did little to induce transition and were thus removed; the slat step was left unfaired as on the actual aircraft.

Coanda Surface Imperfections

From a design and operational standpoint, it was desirable to investigate the effects of imperfections in the Coanda surface downstream of the slot. To represent a poorly constructed Coanda surface with a protruding surface producing a forward facing step in the jet, a piece of 0.012-in. thick tape was applied across the entire span of the right wing blown section, with the step located 90 deg downstream of the slot (see Figure 29). This imperfection resulted in serious degradation of the jet effectiveness, causing a 22-percent reduction in lift at $C_{\mu} = 0.30$ in Figure 29. Continuation of this imperfection to include the left blown surface as well could produce as much as twice that loss; any forward facing protrusion should thus be avoided in construction. Figure 29 also shows the effect of holes in the Coanda surface, representing possible damage due to enemy weapons. To model this, wax which covered attachment screws in the right Coanda surface was removed in the pattern shown in Figure 29, representing a porosity (hole area/surface area) of 0.0068. The total lift loss, should both wings receive this amount of damage, was 8 percent at $C_{\mu} = 0.30$. Should protruding metal result from weapon impact, larger lift loss would be expected. Figure 29 also shows additional data on the effect of removing

the slat gap radius on the main airfoil and supplies supporting data for the effects previously shown in Figure 16.

Final Lifting Surface Configuration

The final lifting surface, modified as necessary to reduce cost, increase simplicity, or conform to existing structures and conditions, is summarized in model scale:

Coanda trailing edge: $r/c = 0.03623$, $r_{av} = 0.5084$ in., $C_{av} = 14.033$ in.

$h/r = 0.01406$, $h/c = 0.00051$, $h_{av} = 0.0071$ in.

slot from WS 56.1 to 265.5, 24.99 in. length

Slat: 25-deg deflection, 0.02C gap, increased L.E. radius

Glove: Kruger leading edge, with air conditioner inlet scoop on right side

Fences: set 2F (outboard fence at WS 265.5, inboard heat shield fence at WS 56.1; conventional fences removed)

Slat gap radius: removed

Wing pylons: at W.S. 144.0

Wing plenum: modified as shown in Figure 20

Yaw control thrusters: at WS 259.25 (unblown)

Slat step: unfaired

Flap louvers: in place ahead of slot

HORIZONTAL STABILIZER DEVELOPMENT

The rather large nose-down pitching moment associated with blown systems of this type are evident in Figures 12 and 17 and, when compared to the conventional A-6, suggest that the existing all-moving horizontal stabilizer will probably be insufficient to assure longitudinal trim. An attempt to improve its trim capabilities was undertaken in Phase I after development of the lifting surface, and was continued in Phases II, III and IV of the investigations. The following sections detail changes in tail configuration and characteristics of the flow field in which the tail must operate.

Wing Downwash and Dynamic Pressure at the Tail

The large streamline curvature produced by the blown wing was expected to generate large downwash angles in the tailplane vicinity, which would result in some loss of dynamic pressure at the tail. To investigate the downwash, the horizontal tail was removed and three thin wires with cotton tufts attached were strung from tunnel floor to ceiling with the tufts at the horizontal tail quarter-chord location (when $\alpha = i_s = 0$ deg) at three spanwise positions:

y, in.	$y/0.5b_T$	ℓ , in.	C_T , in.
2.92	0.200	33.03	10.22
6.27	0.429	34.94	8.68 (tail MAC)
14.62	1.000	39.75	4.68 (tip)

where ℓ = longitudinal distance from 0.253 \bar{c} of the wing to the respective tail quarter chord. The tail root chord at the fuselage centerline ($y=0$) is 11.69 in. and the tail quarter-chord line intersects the fuselage at $y = 1.85$ in. or $y/0.5b_T = 0.127$. Photographs were taken of these tufts at $q = 15$ psf over a range of fuselage incidence and momentum coefficient. Figure 30 shows several sample photos, where the most forward appearing wire is at the $y/0.5b_T = 0.200$ spanwise station and the most aft at $y/0.5b_T = 1.000$. The white stripe on the fuselage represents the horizontal tail chord location; the two parallel lines on the fin are located at $0.5 \bar{c}_T$ and $1.0 \bar{c}_T$ above the chord plane. The shorter stripes perpendicular to the chord line represent the tail quarter-chord positions at the three spanwise locations. The angles between the tufts and the tail chord line at these positions are the local tail angles of attack α_T and were measured directly from the photos. The fuselage incidence α (corrected for tunnel induced effects as discussed in the Appendix) was obtained from recorded data and the local downwash calculated as the difference:

$$\epsilon = \alpha - \alpha_T$$

where wing incidence relative to fuselage is $i_w = 0$ deg. These data for the three spanwise positions are shown in Figure 31, which shows curves faired through data obtained independently from the photos by two investigators. Large downwash angles at the tip are evident, and local values of $d\epsilon/d\alpha$ approach 1.0 with increasing C_{μ} . However, data at the tail MAC show reduced local downwash and $d\epsilon/d\alpha$ decreasing with increased C_{μ} . The 0.200 station shows increased downwash relative to the MAC location. These data show that the tail span is immersed in a largely varying downwash field due to the vorticity from both a very strong outboard (wing tip) vortex and an inboard vortex at the wing-body juncture. Attempts to derive an effective downwash for the entire tail from existing data, tail-on and tail-off, yielded values similar to those measured at the tail MAC but were based on several unsubstantiated assumptions (such as $q_T/q = 0.95$). An attempt to evaluate the dynamic pressure at the tail plane was undertaken by installation of a pitot-static probe at the tail MAC spanwise location ($y/0.5b_T = 0.429$) with its measuring station approximately $0.16 \bar{c}_T$ ahead of where the tail leading edge would normally be. The probe was later mounted on the antenna pod near the top of the vertical fin ($1.03 \bar{c}_T$ above the first location on the chord line) with the measuring station at about midchord of the fin and lateral location at $y/0.5b_T = 0.335$. Figure 32 shows these results, where a loss in dynamic pressure of up to 45 percent of the free-stream value is seen. At the antenna pod location, losses of only 10 percent or less are observed, confirming the fact shown by the tuft pictures that there is little flow deflection or dynamic pressure loss at this high position. Considering that the pitot-static probe may be somewhat inaccurate in the high angularity of the downwash field, these results, nevertheless, indicate that the tail will be operating in a flow field adverse to the generation of the large moment needed for longitudinal trim. Whereas relocation of the horizontal tail on the top of the vertical fin appeared an obvious and effective solution, the cost of doing so on the flight demonstrator was prohibitive. As an alternative, an investigation to improve the existing all-moving stabilizer was undertaken.

Phase I Horizontal Stabilizer Development

In this segment of the investigation, the main objective was to first determine the performance of the existing stabilizer, and if inadequate, to determine what modification could be made to provide trim over a range of C_μ up to 0.30, and tail incidence from -24 deg (LE down) to +10 deg. The nominal and actual measured values of stabilizer incidence relative to the fuselage reference line are as follows:

<u>nominal i_s, deg</u>	<u>measured i_s, deg</u>
+10	10.18
+ 7	7.20
+ 3	2.82
0	- 0.18
- 5	- 5.10
-10	- 9.97
-15	-15.37
-18	-18.13
-24	-23.95

Table 2 lists the various configurations tested during Phase I of the investigation, most of which are shown in Figure 33. Whereas the range of C_μ and stabilizer incidence varied, a comparison of configurations is made here for $C_\mu = 0.10$ and 0.20 at $i_s = -18$ deg (Figures 34 and 35). The conventional horizontal tail airfoil sections vary from NACA 64A007Mod at the tip to 64A009Mod at the root, the modification consisting of a slight leading edge inverted droop and an enlarged leading edge radius. Even though these modifications should prove favorable, this tail (Configuration 46) is stalled over most of the aircraft incidence range in Figure 34 and cannot provide the nose-up pitch to return $C_{M0.253\pi}$ to zero for trim. An attempt to reduce the leading edge stall by use of an inverted leading edge slat deflected -27 deg (Configuration 50) helped little, as shown in Figure 35. However, when combined with a 20-percent tail chord extension deflected upwards -20 deg (denoted Flap 1, Configuration 51), considerable pitch improvement resulted. Realigning the slat trailing edge relative to

the airfoil leading edge and deflecting the slat to -33 deg (Configuration 52) produced additional moment and reduced the stall somewhat at lower C_{μ} . Additional chord extension or upward deflection (Configurations 61, 62, and 63) produced more than enough pitch to trim the aircraft up to $C_L = 3.42$ at $C_{\mu} = 0.20$.

Additional improvements in reducing tail stall were obtained by reducing the inboard wing vortex by either removing the inboard wing fence (Configuration 54) or by removing the engine inlet and exhaust plugs so that flow through the engines could exit into and dissipate the vortex (Configuration 55). Also, a fairing blending the outboard end of the tail slat into the tip cap provided an effective droop (Configuration 58) and stall alleviation. Changes which proved detrimental included fences on the tail (Configuration 56) and a spanwise extension of the tail (Configuration 64, which put more tail surface into the tip vortex). An attempt was made to add additional mass flow into the inboard vortex by simulating the jet exhaust with a 5/8 in. O.D. tube mounted inside the flow-through engine channels. Located upstream of the exit, the tube entrained air through the engine inlet; but due to the tube's small size, the 90-psig supply pressure was reduced to approximately 1.75 psig maximum pressure at the jet exhaust exit with a very nonuniform pressure distribution across this exit. Providing a measured thrust coefficient of less than 0.03, the test was not very representative of full scale, and the effects (Configuration 65) were somewhat detrimental in Figures 34 and 35, probably due to the poor exhaust characteristics. Thus, at the end of Phase I, the tail which most appeared to provide sufficient trim capability with a minimum of leading edge stall was Configuration 63, the inverted camber airfoil with a -33 deg slat deflection, a -25 deg deflection of a $0.40c_T$ tail chord extension, and a tip droop and fairing; see Figure 33.

Aft Center-of-Gravity Movement

Additional data taken for the Configuration 63 horizontal stabilizer showed that the nose-down moment associated with $C_{\mu} \geq 0.22$ could not be trimmed near $C_{L_{max}}$ with the existing maximum stabilizer deflection of -24 deg. Furthermore, attempts at obtaining additional tail download by greater deflection of the extended tail chord (such as Configuration 62 in

Figure 34) produced larger regions of leading edge stall due to increased circulation around the tail. To reduce the untrimmed moment, the aircraft center of gravity was shifted aft to the $0.35\bar{c}$ point. Figure 36 shows the destabilizing effect on the tail-off data of Figure 12; but as Figure 37 shows, the increased tail size aptly counteracts this tendency. The aft c.g. position provides additional nose-up moment that allows trimmed $C_{L_{max}}$ of 4.3 at $C_{\mu} = 0.30$ and $i_s = -19$ deg (see section on trimmed data, p. 22). The stability level is reduced from that at the $0.253\bar{c}$ c.g. location, but as Figure 37 shows, it is still considerably greater at $0.35\bar{c}$ than the standard A-6A high lift configuration with $x_{cg} = 0.253\bar{c}$. The one exception is for $C_{\mu} = 0$, where the aft c.g. position is slightly less stable than the conventional A-6 ($dC_M/dC_L = -0.102$ compared to -0.111). However, the aft position appears quite satisfactory for all values of C_{μ} including 0, and will thus serve as the reference location for the remainder of these investigations.

Phase II Horizontal Stabilizer Modifications

Although the final tail configuration of Phase I appeared aerodynamically adequate, the structural aspects posed some problems. The $0.40c_T$ flat plate flap attached at 25 deg deflection to the sharp trailing edge of the conventional tail presented the problems of large moments and loads at the thin attachment point, as well as an unsupported lengthy flat plate, which would probably bend and possibly vibrate. To reduce these problems, the various configurations of Figure 38 were investigated to find a more suitable structural shape which would provide aerodynamic characteristics similar to Configuration 63. For all configurations, the -33 deg slat deflection and tip droop and fairing were retained. Figures 39 and 40 present the moment data for those configurations tested, where Configuration 68 is the reference shape from Phase I (Configuration 63), deflected to $i_s = -15$ deg. Initially, a shortening of Flap 4 to $0.20c_T$ (Flap 5) reduced the download on the tail to the point of not being able to trim at $C_{\mu} = 0.30$. A configuration suggested by Grumman involved removal of the existing $0.20c_T$ honeycomb trailing edge structure from the conventional tail, insertion of a cambered section, and reattachment of the trailing edge at a -25 deg deflection, providing a highly cambered and thicker trailing edge structure.

These shapes are called GAC-1, -2, and -3, and provide an effective chord increase of either $0.10c_T$ or $0.274c_T$, the lengths of the trailing edge extensions when projected onto the original chordline. The GAC-1 shape provided somewhat more download than Flap 5, but the increased flap length of GAC-2, and -3 provided ample trim up to and including $C_{\mu} = 0.30$. The effect of increasing the leading edge radius on the main tail airfoil (not the slat) is shown by comparing Configurations 104 and 105 as well as Configurations 119 and 120. In both cases, the increased radius reduces tail stall. Also, note that Configurations 101 through 120 employed the fuselage drag brakes deflected to 60 deg (see Drag Generation, p. 26) which produced a flow field modification sufficient to cause large regions of tail stall, especially at higher C_{μ} . Retracting the drag brakes reduces or eliminates this stall (Configurations 68 and 121).

Phase III Horizontal Stabilizer Modifications

After a complete range of momentum coefficients and tail settings had been investigated for the GAC-3 tail, it became apparent that two rather serious problems existed with that configuration, as shown in Figure 41. With $C_{\mu} = 0$, the cambered tail provided so much download and nose-up pitch that the aircraft could not be trimmed with its maximum upper deflection of +3 deg (later found to be limited to only +1.5 deg on the flight demonstrator). Also, at the large downwash angles associated with high blowing, the circulation around the tail at $i_s = -24$ deg further reduced tail stall angles such that the tail was stalled over more than 90 percent of the aircraft incidence range. The tail was over-designed, and the Phase III effort was undertaken to reduce the effective camber and the associated leading edge stall. Figure 42 presents the configurations investigated. A 40-percent chord trailing edge extension deflected -10 deg (EC-40-10-D) was found to trim $C_{L_{max}} = 4.0$ at $C_{\mu} = 0.30$, while still trimming $C_L > 0.44$ at $C_{\mu} = 0$ with maximum upward deflection of +3 deg. Variations were made in the leading edge slat angle (reduced angle of -27 deg being denoted RA), in sealing the slat gap (denoted -SS), and in converting the slat to a drooped leading edge with increased radius (denoted -D). The drooped configuration was felt to be the simplest to construct, and thus became the final configuration, as pictured in Figure 42. Note that the

stabilizer tip fairing and droop, as well as the increased leading edge radius on the stabilizer main airfoil, were removed from all the configurations of Phase III.

Phase IV Horizontal Stabilizer Modifications

Phase IV was undertaken to develop the final Phase III tail into a more structurally-feasible configuration with better performance in the unblown flight mode. Figure 43 presents the trailing edge configuration suggested by Grumman to replace the flat plate deflected trailing edge of Configuration EC-40-10-D. The fairing between the airfoil surface at $x = 0.556c_T$ and the trailing edge of the flat plate has been sized to produce slightly less effective camber (and thus the ability to trim at lower C_L) than EC-40-10-D. This configuration, GAC-6, has a reduced trailing edge mean line deflection of -6.25 deg but an increased effective chord length of $0.630c_T$. As Figure 44 shows, this allows trim down to $C_L = 0.2$. (Trim at this low C_L is necessary for unblown climb and descent to and from flight test altitude because available maximum stabilizer incidence on the test aircraft is $+1.5$ deg, and because power effects are believed to require additional positive tail deflection to trim.) Tuft studies of flow over this tail at $i_s = +3$ deg and $C_u = 0$ showed regions of separation and unsteadiness behind the leading edge of the inverted droop. These were reduced or eliminated by reducing the droop angle to approximately -25 deg, Configuration GAC-6RA. This was then accepted as the final tail configuration for the flight demonstrator. The slightly reduced longitudinal stability ($dC_M/dC_L = -0.028$ at $x_{cg} = 0.35\tau$ compared to -0.044 for the conventional tail on the standard A-6A approach configuration at $x_{cg} = 0.253\tau$ and $i_s = +3$ deg) can be increased to -0.050 by forward movement of the c.g. location to 0.32τ (Figure 45). A forward c.g. shift will occur in flight as the landing gear is retracted and as fuel transfer is performed. Figure 45 also indicates the neutral point location for $i_s = +3$ deg to be around $x_{cg} = 0.38\tau$.

Final Horizontal Tail Configuration

Based on the capability to trim both the high lift blown case and reduced lift unblown case, the GAC-6RA horizontal stabilizer was chosen for

use on the flight demonstrator. Constructed on the existing A-6A all-moving stabilizer rotating at the existing torque-tube location, this tail has the leading and trailing edge modifications shown in Figure 43. No additional outboard tip droop or fairing has been added. The existing incidence range ($-24 \text{ deg} \leq i_s \leq +1.5 \text{ deg}$) will be used unless additional analyses of power effects or required maneuver margin indicate the need for re-indexing to provide more leading-edge-up throw. To aid in proper position of the c.g. during flight tests, gear should probably remain down (aft c.g.) during higher blowing runs and retracted during unblown runs.

TRIMMED AERODYNAMIC DATA

As the above tail development phases were being conducted, the tail developed in each phase was tested over a range of tail incidence and momentum coefficient to determine its trim capabilities. In most cases, these runs exposed the limitations of each tail. Such was especially the case in Phase I, where the optimum lifting surface exhibited large nose-down pitch. The trim capability of the final tail configuration (Slat 2, Flap 4) of Phase I is shown in Figure 46 for the two c.g. positions tested. For the forward c.g. location, trimmed $C_{L_{\max}}$ was limited to 3.68 as the tail lower incidence limit of -24 deg was reached. At the aft location, $C_{L_{\max}} = 4.28$ could be trimmed at the C_{μ} limit of 0.30, but $C_{L_{\max}} < 2.25$ (and reduced C_L at lower α and C_{μ}) was unobtainable as the positive tail incidence limit of 1.5 deg was encountered. In addition, for $C_L < C_{L_{\max}}$, a number of problems were related to tail stall at lower aircraft incidence and higher C_{μ} . In general, a less than operational set of trim data could be found in Phase I, even though quite promising trimmed values of $C_{L_{\max}}$ were attained.

The trimmed lift and drag coefficients obtained with the GAC-3 tail of Phase II are shown in Figure 47 and compared with the conventional A-6A in the trimmed approach configuration. Greater than 110-percent improvement in $C_{L_{\max}}$ is achieved at $C_{\mu} = 0.30$. Figure 48 shows variation in trimmed lift and drag with C_{μ} . From the data of Figure 49, it is seen that the large camber of the tail requires positive tail settings greater than the $+1.5\text{-deg}$ upper limit in order to trim C_L of less than approximately 2.7 to 2.9. This proves to be a problem for the low and no blowing cases and, as

shown in Figures 47 to 49, makes a large region of the trimmed data unobtainable with this tail incidence range on the flight demonstrator. Re-indexing of the horizontal tail to allow a higher upper limit is a possible solution, but would probably produce flow separation from the tail leading edge at such high local incidence. The alternative of further tail modification to somewhat reduce available download was thus chosen.

Figures 47 and 48 point out some benefits discussed in Reference 11 for this type of blown high lift system. The blown drag polars, composed primarily of induced drag, are substantially higher than that of the conventional A-6. This will offset engine thrust, allow equilibrium approach at higher power settings, bleed rate and descent angles, and reduce engine spin-up time in the event of a wave-off. Unlike many blown high lift systems, very little jet thrust recovery results. Thus, low speed, steep glide slope approaches are possible. As Figure 48 indicates, maximum lift augmentation occurs at C_{μ} values of 0.15 or less, which are within the limits that should be obtainable from bleed of many existing turbine engines. The system thus appears feasible for a number of existing aircraft without large powerplant modifications. Also, lift achieved from blowing rather than high aircraft incidence should offer considerable improvement in pilot visibility on approach.

In Phase III, thorough ranges of C_{μ} and i_s values were run to determine trim characteristics of the sealed slat tail (EC-40-10-SS); however, as previously discussed, the drooped leading edge configuration (EC-40-10-D) was chosen as the final configuration. The drooped tail gives slightly more download than the sealed slat (see Figure 41), but the characteristics are otherwise quite similar. For this configuration, the trimmed lift and drag are presented in Figure 50 (in comparison to the standard A-6A data^{8,12}) and tail incidence required to trim in Figure 51. Whereas the drooped tail results in very slight losses in trimmed $C_{L_{max}}$ relative to the GAC-3 tail of Figure 47 (losses of 0.09, 0.07, and 0.14 for $C_{\mu} = 0, 0.10$, and 0.30 , respectively), almost the entire range of C_{μ} and α in Figure 50 can be trimmed within the existing stabilizer travel range, and an increase of 104 percent in trimmed $C_{L_{max}}$ over the standard A-6A is still obtained.

Figure 50 also indicates representative approach conditions, where the more conventional multiples of V_{stall} are shown in comparison to a criterion

suggested by Grumman for STOL approach: $\alpha = \alpha_{\text{stall}} - 10 \text{ deg}$. This provides an allowance for 10 deg of gust upwash, yet does not penalize the high C_{μ} cases by taking a fixed percentage of $C_{L_{\text{max}}}$. Figure 52 presents trimmed lift-to-drag ratio in comparison to that of the standard A-6A, in both clean and approach configurations. Also shown is an equivalent lift-to-drag ratio where the equivalent drag ($C_{D_e} = C_D + C_{\mu}$) attempts to account for the momentum expended to obtain the lift, but makes no assumption on internal pressure losses, nozzle efficiencies, etc. These lift-to-drag ratios are seen to decrease with increased blowing and at higher lift coefficients.

The Phase IV data was run only for the $C_{\mu} = 0$ case since the primary objective of this phase was to develop the tail for unblown flights. Figure 44 compared at $i_s = +3 \text{ deg}$ the pitch characteristics of the three configurations tested; Figure 53 compares lift and pitch for those configurations at various tail settings and $C_{\mu} = 0$, and Figure 54 presents the unblown drag polars for this final Phase IV configuration. The trimmed lift and drag data are presented as Figure 55 where the blown values are adjusted from the EC-40-10-D tail data of Figure 50. The difference between the two tail configurations occurs in the stabilizer setting required to trim, Figure 56 compared to Figure 51. For the GAC-6RA tail at $C_{\mu} = 0$, the 1.5-deg stabilizer upward travel limit only allows trim for C_L greater than 0.58 (which can be reduced to 0.38 if the c.g. is moved forward to 0.32c). This 0.58 minimum trimmed C_L value results in an increase of 33.2 knots in equilibrium trimmed speed obtainable in the unblown flight test configuration weighing 34,000 lb and flying at sea level, in comparison to the 147.7 knot speed due to the EC-40-10-D minimum C_L of 0.87. The L/D of the unblown configuration is plotted in Figure 57, where the conversions to full scale and gear retracted provide an improved aerodynamic efficiency. Since the flight demonstrator will have its high lift devices locked in the deployed position, $C_{\mu} = 0$ becomes the minimum drag case and corresponds to the configuration for climb to and descent from test altitude as well as cross-country ferry. The maximum C_L trimmed with -24-deg tail incidence was reduced slightly from 3.96 for the EC-40-10-D tail to 3.89 for the GAC-6RA configuration, resulting in an increase in minimum obtainable stall speed of only 0.62 knots at sea level for a 34,000-lb aircraft. The net effects of the GAC-6RA tail are thus an expanded flight envelope and a

configuration which is structurally more feasible. In addition, flow separation at the leading edge at positive i_s has been eliminated.

In Phase V, the GAC-6RA tail was retained, but a number of changes to the wing were made as discussed earlier to convert the model to the actual flight demonstrator being constructed by the contractor. Figure 58 shows the effect of horizontal tail deflection on lift, drag, and pitch; these curves are used to establish the trim lift and drag data of Figure 59 and the tail incidence required to trim in Figure 60. Apparently, the reduced blowing span has increased the effective downwash at the tail, because a comparison of Figures 60 and 56 show the same trimmed lift in Phase V achieved with 1 to 2 degrees less negative tail incidence. Due to this, the horizontal stabilizer (already completed by the contractor) could not trim $C_L < 0.82$ with blowing off, and thus the incidence had to be readjusted on the flight demonstrator to a new range, $-21.5 \text{ deg} \leq i_s \leq +4 \text{ deg}$. However, this produces no change in the trimmed maximum $C_L = 3.89$ for Phase IV and allows trimmed minimum C_L down to 0.28 at $C_\mu = 0$ (corresponding to a maximum trimmed speed of 260.3 knots for a 34,000-lb aircraft at sea level). Trimmed lift-to-drag ratios are presented in Figure 61. Thus the final flight test configuration can achieve trimmed C_L from 0.28 to 3.89 and exhibits a slightly expanded flight envelope over the Phase IV model.

GROUND EFFECT

The flight test goal of demonstrating STOL operations with the testbed aircraft required that a knowledge of its behavior in ground effect be available. To accomplish this, the fixed ground plane shown in Figure 62 was installed at various heights below the model in Phase II, with the gear down and the GAC-3 horizontal stabilizer installed. The test technique and tunnel corrections employed are discussed in the Appendix. A collection of data for powered lift aircraft operating in ground effect is presented in Reference 13. As also reported by Stevens and Wingrove,¹⁴ ground effect may be adverse at high incidence and C_L ; however, favorable effects frequently occur at the more moderate lift and incidence values that are characteristic of actual takeoff and landing. The adverse conditions are primarily associated with jet impingement and stagnation on the ground at low heights, thus reducing available lift and stall angles. This effect is visibly displayed

in the tuft photographs of Figure 63, where for $C_{\mu} = 0.21$ the tufts below and ahead of the wing are seen to be deflecting forward. Figure 64 presents trimmed lift and drag data for three ground board heights and the out-of-ground-effect data, where the height h_g is that of the c.g. above the ground at zero aircraft incidence, nondimensionalized by $\bar{c} = 15.388$ in. The reduction in stall angle and $C_{L_{\max}}$ at low height and higher C_{μ} is evident; this dependence on height above the ground plane is plotted in Figure 65 for $C_{L_{\max}}$. In this figure, a limit labeled "Turner's Criterion" has been imposed. As developed by Turner,¹⁵ this criterion defines the combinations of height above ground and lift below which the fixed ground plane technique generates data inaccuracies due to interaction between the model flow field and the boundary layer on the ground board. Thus, the actual losses in $C_{L_{\max}}$ at higher C_{μ} are probably not as severe as the data predict. However, as Figure 66 shows, favorable ground effect occurs at lower incidence. Excluding the data on the limiting criterion line, Figure 66 implies that for almost all values of C_{μ} tested at 12-deg incidence or less, the lift in ground effect is greater than that in free air ($h_g/\bar{c} = \infty$). If the operational limit on incidence of $\alpha_{\text{stall}} - 10$ deg is imposed, the flight test aircraft should never experience an adverse lift loss due to close ground proximity.

The ground effects on drag and pitch should also be considered. As the drag polars of Figure 64 show, operation at a given lift and C_{μ} produces reduced drag closer to the ground for incidence of $\alpha_{\text{stall}} - 10$ deg or less. This should produce a favorable effect during STOL takeoff. Figure 67 implies that for constant C_{μ} , approach to the ground results in increased nose-down pitching moment for either a constant lift coefficient or constant incidence. This is probably the result of reduced downwash angles producing less tail download to counteract the pitch, or increased nose-down pitch due to jet impingement on the ground. The result is a requirement for greater leading-edge-down stabilizer settings to trim the aircraft near the ground.

DRAG GENERATION

As the data show (for example, Figures 47, 50 and 55), the primary drag contribution of the CCW high lift system is induced drag due to lift, with negligible reduction in drag due to the resultant thrust component from the wing jet sheet. Increased blowing produces increased drag, quite

unlike blown flaps, jet flaps, or upper surface blowing. However, because descents down steep glide slopes are desirable for STOL approaches and because higher engine thrust levels are required to produce the bleed air to power the wing, generation of additional drag may be desirable for equilibrium STOL flight paths. In Phase I, investigations of additional drag sources were thus conducted, using the wing of Configuration 39 and the horizontal tail employing Slat 2, Flap 4, and the faired, drooped tip. Drag increments due to landing gear, wing store pylons, wing stores (four 300-gallon fuel tanks) and wing tip drag brakes are shown in Figure 68a for $C_{\mu} = 0$. Only the landing gear and the 60-deg drag brakes produce increments in $C_{D_{min}}$ of greater than 0.01. Similar trends are seen in Figures 68b and 68c for $C_{\mu} = 0.10$ and 0.20 . Figure 69 shows the effects on lift. With blowing applied, both 20- and 60-deg drag brake deflections produced early stall and a strong buffet; whereas drag was greatest with these devices at low aircraft incidence, they produced lower $C_{L_{max}}$ and thus reduced corresponding drag because of interference with the lifting surface and tip loading. In equilibrium flight with blowing at high angle of attack, drag brake deflection would produce stall, lift loss, drag reduction and resultant aircraft acceleration. At $C_{\mu} = 0.20$ and presumably greater, the store pylons and fuel tanks also produced a decrease in stall angle and some loss in lift and drag. The greatest stall angle, $C_{L_{max}}$, and drag could be obtained by using no drag producing devices other than the landing gear.

Earlier versions of the A-6A employed fuselage speed brakes which deflected outward from the fuselage just aft of the engine tailpipes and thus acted as thrust deflectors. In Phase II, these speed brakes were deflected 60 deg on the model to determine their aerodynamic effectiveness as drag devices (the unpowered model does not allow their effects on thrust to be evaluated). The effect of the fuselage speed brakes was found to be very similar to that of the wing tip speed brakes: by interfering with the inboard wing loading, they produced lower stall incidence and reduced $C_{L_{max}}$, but produced higher drag at incidences below stall. However, a more severe problem is shown in Figure 70. By protruding into the strong vortex generated at the wing-fuselage junction, they apparently altered the downwash field so that stall of the horizontal tail occurred over a wider range

of aircraft incidence. Thus, fuselage speed brakes were categorized as unacceptable for use on the flight demonstrator.

POST-STALL AND STALL HYSTERESIS

Tuft studies showed the stall to be from the wing trailing edge, spreading inward from the fence at the outboard slot end. The unblown wing tip outboard of this fence was found to stall at aircraft incidence as low as 3 deg due to the large upwash created by the vortex at that location, and it was because of this stalled region that the fence was a necessity. With the tufts removed in Phase III, the model was pitched well beyond stall and then returned to low incidence for several values of C_{μ} . Figure 71 shows the results for two blowing rates. The data are pitch-pause static force data and thus do not include any dynamic components of stall. Due to the very strong entrainment effect of the jet, the flow reattached itself to the trailing edge at exactly the same angle of attack at which it had separated. There was negligible stall hysteresis, as shown by the flagged symbols and dashed curves, which indicate decreasing incidence returning from approximately 27.5 deg. In addition, regardless of blowing rate, all post-stall curves converged on a point ($C_L \approx 2.0$ at $\alpha = 28$ deg).

Drag and pitching moment curves of Figures 72 and 73 show additional post-stall trends. Unlike conventional stalls where flow separation leads to increased drag, stall of the CCW configuration leads to the reverse because the jet entrainment prevents large areas of flow separation; induced drag is thus quite predominant over separation drag. Lift loss beyond stall thus results in a corresponding drag reduction. For an aircraft which has approached the stall at equilibrium thrust, velocity, and C_{μ} levels, exceeding the stall angle will result in reduced drag and thus an excess of thrust which will accelerate the vehicle. Increased velocity will result in reduced C_{μ} and assist in recovery from the stall. Note also that there is negligible hysteresis in the drag polars as angle of attack is reduced. For $C_{\mu} = 0.30$, higher incidence beyond stall produces less drag than low incidence prior to stall. Pitching moment exhibits a post-stall trend towards nose-up values, but this eventually reverses itself at higher incidence until, for $C_{\mu} = 0.30$, the pitch eventually decays to zero. As the aircraft accelerates after stall, reduced C_{μ} results in reduced moment to

trim once the prestall portion of the curve is reached (for examples, see Figures 12, 17, and 58), and thus the stall recovery should be less difficult.

SPLITTER FLAP

While the high induced drag levels associated with the CCW rounded trailing edge are quite beneficial in steep STOL landing approaches, on takeoff they may degrade aircraft acceleration and short takeoff potential in spite of the high lift availability. Optimum takeoff techniques have not yet been determined, but initial analysis indicates this problem may be overcome by not turning on the blowing until near the takeoff speed corresponding to the high blown lift obtainable with CCW. As an alternative, a splitter flap attached to the rounded trailing edge was proposed in an attempt to reduce drag by increasing the thrust recovery during takeoff. Figure 20 shows this configuration as applied to and tested on the Phase V model. The 45-deg flap deflection relative to the chordline was found to be most effective for this type of blown application.¹⁶ The flap length is $0.0726C$, equal to the trailing edge diameter, so that an operational device could be retracted along a radius of, and stored within, the rounded trailing edge. The dummy yaw jets were removed, and as Table 6 shows, the configuration employed the final Phase V flight demonstrator wing, fuselage, and tail. Figure 74 presents lift, drag, and pitching moment coefficients for the splitter flap tested with three horizontal tail settings and three blowing rates. In Figure 75, comparison of these data to the final Phase V CCW configuration (from Figure 58) indicates an increase in unblown lift due to the cambering effect of the splitter plate, but a reduction in total lift for $C_{\mu} = 0.10$ and 0.30 since the splitter plate limits aft stagnation point movement to 135° from the slot. As blowing is applied, the lift improvements due to CCW become evident: CCW at $C_{\mu} = 0.05$ achieves the same lift as the splitter flap at $C_{\mu} = 0.10$, and CCW at $C_{\mu} = 0.10$ achieves the same lift as the splitter flap at $C_{\mu} = 0.30$. The drag data imply that at fixed C_{μ} and α the splitter flap has considerably lower drag levels than CCW for C_{μ} greater than 0. This drag reduction is not totally due to splitter flap thrust recovery, because the comparisons are at unequal lift values and induced drag due to lift is the predominant drag component. At

constant values of C_L (as denoted on the drag curves) the splitter drag reduction is not as significant. For example, $C_L = 3.0$ can be obtained by the splitter flap at $C_\mu = 0.30$, $\alpha = 16.1$ deg, and $C_D = 0.503$, or by the CCW at C_μ of only 0.10, $\alpha = 13.2$ deg, and $C_D = 0.838$. Whereas the 40-percent reduction in drag due to the splitter flap appears large, it requires three times the momentum coefficient, which will result in considerable thrust loss due to bleed and thus offset the drag reduction. It is thus not clear-cut which system is to be preferred for takeoff. Up to $C_L = 3.0$, the splitter flap results in reduced drag at higher required mass flow, while lift coefficients above 3.25 are unobtainable by the splitter flap. It does appear that considerable reductions in drag (and recovery of thrust loss due to bleed) may be obtained by operating the CCW at lower C_μ and higher α to achieve a desired C_L for takeoff.

LATERAL AND DIRECTIONAL CHARACTERISTICS

A significant amount of data was generated to verify the lateral and directional stability and control as well as handling qualities. The specifics of the investigations conducted are listed in Tables 2 through 6, and a brief discussion and some data are presented in Reference 11.

CONCLUSIONS AND RECOMMENDATIONS

Wind tunnel investigations were conducted on a 1/8.5-scale model of the A-6/Circulation Control Wing flight demonstration aircraft in order to confirm the high lift capability of the concept, to improve the lifting and control surfaces of the testbed aircraft, and to provide supporting data to assure safety of flight and adequate handling of this aircraft. Results of this effort have provided the following conclusions:

- Two-dimensional data yielded section lift coefficients as high as 6.5, while the three-dimensional data showed that the best CC wing configuration examined could multiply $C_{L_{max}}$ by a factor of 2.2 compared to that of the conventional A-6A high lift configuration.
- Wing and horizontal stabilizer configurations were developed to simplify the actual aircraft modifications, reduce costs, increase the range of parameters obtainable in the trimmed full scale flight envelope, and provide adequate aircraft handling. Whereas this reduced the maximum trimmed

aerodynamic lift coefficient from 4.1 to 3.9, it provided a greatly expanded flight envelope that otherwise could not have been obtained.

- Aft c.g. shift to 0.35 \bar{c} to allow trim over this expanded envelope resulted in greater longitudinal stability than the conventional aircraft with c.g. at 0.253 \bar{c} .

- Effects of Reynolds number and slot height variations were investigated to aid performance predictions for the full-scale aircraft, and the effects of imperfections in the rounded trailing edge were studied.

- Model operation in ground effect showed that for the anticipated range of C_{μ} and aircraft approach incidence less than $\alpha_{\text{stall}} - 10$ deg, lift in ground effect was always greater than in free air; just the opposite was true for drag.

- In general, because of the predominance of lift-induced drag, drag generating devices such as wing tip and fuselage drag brakes proved detrimental and unnecessary for STOL operations because of their interference with the wing flow field.

- Post-stall and stall hysteresis investigations revealed virtually no hysteresis effects as a result of the very strong flow entrainment properties of the CCW trailing edge.

- A blown splitter flap showed significant reductions in drag under certain conditions and could be a beneficial configuration for thrust recovery during short takeoffs.

The following recommendations are suggested by the above investigations:

- Aircraft flight and control characteristics should be input to a flight simulator to be flown by project test pilots before aircraft first flight.

- A smaller, more efficient horizontal stabilizer, perhaps employing leading edge or spanwise blowing, should be developed before consideration of the CCW on an operational aircraft. Canards might also be considered as trim devices to reduce nose-down pitch.

- Optimizations of short takeoff configuration and piloting technique should be undertaken.

In general, the presented results confirm the high lift capability of the Circulation Control Wing concept, and should provide a very adequate data base upon which to construct and fly the A-6 demonstrator aircraft.

REFERENCES

1. Stone, M.B. and R.J. Englar, "Circulation Control - A Bibliography of NSRDC Research and Selected Outside References," NSRDC Report 4108, AD 775-284 (Jan 1974).
2. Englar, Robert J., "Subsonic Wind Tunnel Investigation of the High Lift Capability of a Circulation Control Wing on a 1/5-Scale T-2C Aircraft Model," NSRDC Report ASER-299, AD 781-856 (May 1973).
3. Englar, Robert J., "Investigation Into and Application of the High Velocity Circulation Control Wall Jet for High Lift and Drag Generation on STOL Aircraft," AIAA Paper 74-502 presented at the AIAA Seventh Fluid and Plasma Dynamics Conference, Palo Alto, California (17-19 Jun 1974).
4. Englar, Robert J., "Subsonic Two-Dimensional Wind Tunnel Investigations of the High Lift Capability of Circulation Control Wing Sections," DTNSRDC Report ASER-274 (Apr 1975).
5. Englar, Robert J., "Circulation Control for High Lift and Drag Generation on STOL Aircraft," AIAA Journal of Aircraft, Vol. 12, No. 5, pp. 457-463 (May 1975).
6. Riebe, J.M., "A Correlation of Two-Dimensional Data on Lift Coefficient Available with Blowing-, Suction-, Slotted-, and Plain-Flap High Lift Devices," NACA RM L55D29a (Oct 1955).
7. Englar, R.J. and R.M. Williams, "Test Techniques for High Lift Two-Dimensional Airfoils with Boundary Layer and Circulation Control for Application to Rotary Wing Aircraft," Canadian Aeronautics and Space Journal, Vol. 19, pp. 93-108 (Mar 1973).
8. Giangrande, G., "Application of the Calderon Flap to a Carrier-Based Jet Aircraft," Grumman Aircraft Engineering Corporation Report FSR-427-1 (Apr 1968).
9. Englar, Robert J., "Experimental Investigation of the High Velocity Coanda Wall Jet Applied to Bluff Trailing Edge Circulation Control Airfoils," NSRDC Report ASER-308, AD 771-690 (Jun 1973). Also published as M.S. Thesis, University of Maryland, Department of Aerospace Engineering (Jun 1973), and as DTNSRDC Report 4708 AD-A-019-417 (Sep 1975).
10. Englar, Robert J., "Two-Dimensional Subsonic Wind Tunnel Tests on a Cambered 30-Percent-Thick Circulation Control Airfoil," NSRDC Report ASER-201, AD 913-411L (May 1972).
11. Englar, R.J., L.A. Trobaugh, and R.A. Hemmerly, "STOL Potential of the Circulation Control Wing for High-Performance Aircraft," AIAA Journal of Aircraft, Vol. 15, No. 3, pp. 175-181 (Mar 1978).

12. Ettinger, John, "A-6E Basic Aerodynamic Data Required for Substantiation of the 1971 Standard Aerodynamics Characteristics Charts and the 1971 NATOPS Flight Manual," Grumman Aircraft Engineering Corporation Report XA128-105-26 (Apr 1971).

13. Campbell, J.P., J.L. Hassell, and J.L. Thomas, "Recent Research on Powered-Lift STOL Ground Effects," AIAA Paper 77-574, in "A Collection of Technical Papers," AIAA/NASA Ames V/STOL Conference, Palo Alto, CA, pp. 47-56 (Jun 1977).

14. Stevens, V.C. and R.C. Wingrove, "STOL Ground Effects Determined from Flight Data," AIAA Paper 77-576 presented at AIAA/NASA Ames V/STOL Conference, Palo Alto, CA (Jun 1977).

15. Turner, Thomas R., "A Moving Belt Ground Plane for Wind Tunnel Ground Simulation and Results for Two Jet-Flap Configurations," NASA TN D-4228 (1967).

16. Stevenson, J.A. et al., "Wind-Tunnel Study of a Circulation-Controlled Elliptical Airfoil," AIAA Journal of Aircraft, Vol. 14, No. 9, pp. 881-886 (Sep 1977).

APPENDIX

MODEL, EXPERIMENTAL APPARATUS, AND TECHNIQUE

MODEL

The 1/8.5-scale A-6A model employed in the present investigations was borrowed from Grumman Aerospace Corporation, and due to its status as a basic aircraft developmental model, very closely resembled the actual aircraft of Figure 2. Table 1 presents the full-scale geometric characteristics of the A-6A, and includes dimensions of the final configuration of the CCW aircraft where they differ from the standard configuration. Design rationale for the three-dimensional (3-D) CCW configuration was to replace the existing 40-deg semi-Fowler flap with the rounded trailing edge developed in the two-dimensional investigation, maintaining the same characteristic parameters of slot location, h/c , r/c , and h/r (some of which were variable due to an adjustable slot height, see Table 7). The 3-D wing configuration thus very closely resembles the section of Figure 4, except that the plenum volume was roughly half as large. Nevertheless, rule-of-thumb guidelines that the converging entrance to the slot should be at least 10 times the slot height and that slot adjustment screws should be at least 50 slot heights upstream in the plenum were maintained. The slot throat is located approximately $0.006C$ aft of the original trailing edge, with the center of the rounded trailing edge directly below the slot lip at a distance $r+h$. Side and aft views of the model (during Phase I) in Figure A.1 show the wing fences, slat, trailing edge detail, pylons, stores, and the flow-through engine ducts. Figure A.2 shows the Phase III wing and tail configurations.

The model wing plenums were instrumented with total pressure probes (three in the left plenum, one in the right) and a thermocouple (at midspan of left plenum). Each plenum was connected through 1-in. I.D. high pressure flexible tubing to a steel common plenum beneath the tunnel test section; see Figure A.3. Model slot height was adjustable with screws in the plenum (see Figures 4 and 20) to allow the range of variation listed in Table 7. Due to the thin lip on the plenum upper surface, considerable expansion of the slot occurred under pressure (see Figure 21 and A.4). Because each of the supply lines into the model was controlled by a separate valve, the

flows into the plenums were independently adjustable to assure balanced lift between the wings and to later test the roll control capability of differential blowing.

TEST APPARATUS AND TECHNIQUE

The three-dimensional investigation was conducted in the DTNSRDC 8- x 10-Foot North Subsonic Tunnel (Figure A.3). The model was mounted on a main strut and a pitch strut, as shown in Figures 8, 9, A.2 and A.3, with the 6.24-ft wing span located horizontally in the 10 ft width of the tunnel. Air was supplied through 1.5-in. I.D. flexible tubing which connected to the steel common plenum, then through the two separate 1.0-in. I.D. lines into the model wing plenums. Mass flow into the model was measured by a venturimeter located in the supply line; the system was capable of a maximum of 2 lb/sec flow.

Six-component data from the balance frame were recorded by strain gage flexures located on Toledo mechanical balances attached to the frame. The strain gage signals were fed into and processed by a Beckman 210 high-speed data system, which digitized and recorded them on magnetic tape for later reduction on an XDS-930 digital computer. For each data point, the Beckman system recorded all data 10 times over a 5-sec interval (to denote any unsteadiness), and then took the average of those. Data from the Toledo scales were automatically recorded for each data point and were punched on paper tape as a check on the electrical data system.

The jet momentum (blowing) coefficient was calculated as:

$$C_{\mu} = \frac{\dot{m}V_j}{qS}$$

where the mass flux (\dot{m}) was recorded by the venturimeter and the jet velocity was calculated assuming an isentropic expansion from wing plenum total conditions to freestream static conditions:

$$V_j = a_j M_j = \sqrt{\gamma R T_j} M_j = \left\{ 2 R T_d \frac{\gamma}{\gamma - 1} \left[1 - \left(\frac{P_{\infty}}{P_d} \right)^{\frac{\gamma - 1}{\gamma}} \right] \right\}^{1/2}$$

It is realized that expansion to local static conditions at the jet exit gives a far more realistic value of V_j and that expansion to freestream static pressure underestimates V_j and M_j . However, local exit conditions are functions of local geometry, and thus a comparison of two blown airfoils of unlike trailing edge geometry but identical slot areas, plenum pressures, and temperatures would yield unlike values of C_μ . The momentum coefficient based on expansion to freestream conditions is thus accepted as a more "universal" parameter for comparison of blown systems. Similarly, isentropic mass flow was calculated as a check on the venturimeter as follows:

$$\text{Choked flow: } \dot{m} = A_j P_d \sqrt{\frac{\gamma}{RT_d}} \left(\frac{2}{\gamma + 1} \right)^{\frac{\gamma + 1}{2(\gamma - 1)}}, P_d/P_\infty \geq 1.89$$

$$\text{Unchoked flow: } \dot{m} = A_j P_d \left\{ \frac{2\gamma}{(\gamma - 1)RT_d} \left[\left(\frac{P_\infty}{P_d} \right)^{2/\gamma} - \left(\frac{P_\infty}{P_d} \right)^{\frac{\gamma + 1}{\gamma}} \right] \right\}^{1/2}$$

The difference between measured and isentropic mass flow is an indication of the jet nozzle effectiveness; this nozzle loss coefficient for Phase I is shown in Figure A.5. Its calculation requires values of measured pressures, temperature, and expanded slot height. Measured mass flow for three slot heights as a function of plenum pressure ratio (P_{D2}/P_∞) is shown in Figure A.6. Note that once the left and right slot height and mass flows were balanced, the total pressure P_{D2} in the middle of the left plenum was used to calculate the flow characteristics of both wings. This figure also shows a comparison to isentropic mass flow at the same pressures and temperatures but assuming no slot expansion. With the exception of the Reynolds number investigation and Phase V runs, the majority of the runs were conducted at a dynamic pressure of 25 psf ($R_e = 1.20 \times 10^6$), with a few specific sets of data at 15 psf ($R_e = 0.93 \times 10^6$) and 20 psf ($R_e = 1.07 \times 10^6$).

TARES AND DATA CORRECTIONS

To account for physical weight transfer as the model was pitched or yawed, wind-off weight tares were recorded for each configuration over the

expected angle of attack and angle of yaw ranges. These values were subtracted from the wind-on pitch and roll data. To account for any additional effect on the balance frame due to pressure in the air supply lines, a series of pressure tares was also run. The temflex supply hoses were plugged at the wing plenum juncture, a range of pressures covering the desired C_{μ} range was then run, and the results on the balance were recorded and correlated with static pressure measured in the supply line just below the balance frame. These data were then subtracted from the wind-on data based on the supply line static pressure recorded with the wing plenums unplugged. Additional corrections were made to drag coefficient to subtract out the drag component of the two air supply hoses attached to the model, and corrections to pitch and drag coefficients accounted for interference effects from the model mounting strut and shield.

Solid blockage corrections to dynamic pressure were calculated as

$$q = q_u (1 + 2\epsilon)$$

where $\epsilon = 0.00390$ was based on blocked area due to fuselage, wings, mounting strut, and wind shield. Uncorrected dynamic pressure (q_u) was measured by calibrated piezometer ring differential read on a ± 1.0 psid transducer. The following tunnel boundary corrections were added to α , C_D , and C_M :

$$\Delta\alpha = 0.6415 C_L, \text{ deg}$$

$$\Delta C_D = 0.0112 C_L^2$$

$$\Delta C_M = 0.01107 C_L$$

where the moment correction was applied only when the horizontal tail was installed.

GROUND EFFECT TEST TECHNIQUE

A ground board 194.5 in. in length was installed in the 10-ft-wide test section, with its leading edge 103 in. ($6.7\overline{c}$) ahead of the strut

centerline and its trailing edge 91.5 in. ($5.9\bar{c}$) downstream of the centerline. At 0 deg incidence, the model c.g. was located 47.561 in. above the tunnel floor; thus three ground plane locations were tested:

$\underline{h_g, \text{ in. at } \alpha = 0 \text{ deg}}$	$\underline{h_g/\bar{c}}$
12.811	0.833 (see Figures 62 and 63)
25.311	1.645
47.561	3.091

The first position (0.833) was sufficiently close to the model that the nose gear impacted with the groundboard at $\alpha < -2.4$ deg and the main gear made contact at $\alpha > 18$ deg for model rotation about the $0.253\bar{c}$ strut attachment point. Thus, only incidence between those limits was evaluated for that groundboard height. For $h_g/\bar{c} = 3.091$ the groundboard was removed from the tunnel, and the tunnel floor became the effective groundplane simply by removing the tunnel boundary corrections to α , C_D , and C_M from the corrected free-air data. With the other two groundboard locations, the method of determining dynamic pressure had to be modified, since the tunnel was thus divided into two unlike channels, and the piezometer ring shown in Figure A.3 was no longer adequate. A pitot-static probe was mounted with its measuring station 65.25 in. upstream of the mounting strut, 12 in. down from the ceiling, and 12 in. out from the left wall. Before installing the groundboard, this probe had been calibrated against the blockage corrected dynamic pressure obtained from the piezometer ring as described. Then, with the groundplane installed, corrected dynamic pressure above the groundboard was obtained from the probe and the relationship $q_{\text{corr}} = q_{\text{probe}}/1.03959$ and was used to reduce the data obtained to the coefficients of Figures 64 through 67.

TABLE 1 - GEOMETRIC CHARACTERISTICS OF THE GRUMMAN A-6A
(full-scale dimensions; model scale = 1/8.5)

<u>Wing</u>		
Area, excluding fillets		528.9 ft ²
Span		53.0 ft
Aspect ratio		5.31
Taper ratio		0.312
Sweep at 0.25c		25.0 deg
Fillet leading edge sweep		55.0 deg
Chords: root (W.S. 0.0)		182.6 in.
M.A.C. (W.S. 131.55)		130.8 in.
wing fold (W.S. 144)		125.9 in.
tip (W.S. 318.0)		57.0 in.
Airfoil sections:		
root (W.S. 0.0 to 33.0)		NACA 64A009 MOD
wing fold (W.S. 144.0)		NACA 64A008.4 MOD
tip (W.S. 318)		NACA 64A005.9 MOD
Incidence		0 deg
Dihedral (outboard of W.S. 65.0)		-1 deg
Location of 0.25c		F.S. 264.0, W.L. 90.5
Flaperon total area (0.12c length)		41.0 ft ²
Leading edge slat area (0.15c length)		49.8 ft ²
 <u>Flaps</u>		
Type	<u>Conventional</u>	<u>JCW Phase V</u>
	0.30c Semi-Fowler	CCW
Total area	104.0 ft ²	12.6 ft ²
Inboard chord (stream wise)	48.2 in. (W.S. 55.5)	5.82 in. W.S. (56.1)
Outboard chord (stream wise)	22.9 in. (W.S. 270)	2.83 in. (W.S. 265.5)
Span (each wing)	214.5 in.	209.4 in.

TABLE 1 (Continued)

<u>Horizontal Stabilizer</u>	<u>Conventional</u>	<u>CCW Phase V</u>
Area	117.0 ft ²	184.4 ft ²
Span	20.38 ft	20.38 ft
Aspect ratio	3.55	2.25
Taper ratio	0.404	0.404
Sweep at 0.25c	30 deg	30.9 deg
Chords: root (B.L. 0.0)	98.5 in.	154.8 in.
M.A.C.	73.89 in. (B.L. 51.0)	115.21 in. (B.L. 52.4)
tip (B.L. 122.25)	39.8 in.	62.6 in.
Airfoil section root	NACA 64A009 MOD	GAC-6RA
tip	NACA 64A007 MOD	GAC-6RA
Dihedral	0 deg	0 deg
Incidence	0 deg	0 deg
l_H (distance wing $\bar{c}/4$ to tail $\bar{c}/4$)	300.51 in.	294.59 in.
Pivot point (W.S. 553.5), % root chord	47.9	41.9
<u>Vertical Tail</u>		
Area	79.25 ft ²	
Rudder area	16.32 ft ²	
Fin area	62.93 ft ²	
Height (from fuselage ref. line, W.L. 100)	123.5 in.	
Aspect ratio	0.962	
Taper ratio	0.307	
Sweep at quarter chord	28.0 deg	
Chords: root (NACA 64A008.1 MOD)	164.74 in.	
M.A.C. (W.L. 162.97)	117.73 in.	
tip (NACA 64A006.5 MOD)	50.51 in.	
l_V (distance from wing $\bar{c}/4$ to tail $\bar{c}/4$)	297.2 in.	

TABLE 1 (Continued)

<u>Control Surface Deflections, Approach Configuration</u>	
Flaps	30 deg Takeoff, 40 deg Landing
Horizontal Stabilizer, Conventional A-6A	+1.5 deg Up, -24 deg Down
CCW Phase V	+4 deg Up, -21.5 deg Down
L.E. slat (streamwise plane)	25 deg
Rudder	+35 deg
Flaperon (spoiler)	0 to +51 deg Up
Wing tip speed brakes (24.25 ft ² total area)	120 deg included angle
<u>Fuselage</u>	
Maximum length	655 in.
Maximum frontal area	49.75 ft ²
Wetted area	848.0 ft ²
Maximum width	73.1 in.

TABLE 2 - PHASE I TEST PROGRAM SUMMARY

Initial Configuration: Wing, body, vertical tail, gear up, $h_{AV} = 0.016$ in.
 $\delta_{rud} = \delta_{sp} = 0$ deg, Horizontal tail off, $q = 25$ psf, -2 deg $\leq \alpha \leq 22$ deg, $C_{\mu} = 0.263$

Config	Runs	Inb'd δ_{SLAT} deg	Outb'd δ_{SLAT} deg	Slat L.E. Radius	Slat Gap C	Fences	Main Airfoil L.E. Gap Radius	Slat Step	Glove (Fillet)	Glove Strake	Purpose
1	1-20	25	25	Conv.	.02	Conv.	0	Unfaired	Conv.	Conv.	Lifting Surface Optimization
2	21-23	↓	↓	↓	↓	↓	.01042C	Unfaired	↓	↓	↓
3	24-25	25	25	↓	.02	↓	↓	Faired	↓	↓	↓
4-6	26-35	37.5	37.5	↓	.02 → .04	Conv. +	↓	↓	↓	↓	↓
7	36-38	37.5	37.5	Conv.	↓	Conv. + Set 2	↓	↓	↓	↓	↓
8-12	39-44	45	45	.023C	.02 → .04	↓	↓	↓	↓	↓	↓
13	45	↓	↓	↓	.02	Conv. + Set 2	↓	↓	Conv.	Conv. OFF	↓
14	46	↓	↓	↓	↓	↓	↓	↓	L.E. Radius Increase	↓	↓
15-17	47-49	↓	↓	↓	↓	Conv. + Set 2A, 5	↓	↓	↓	↓	↓
18	50	↓	↓	↓	↓	2A Only	↓	↓	L.E. Radius Increase	↓	↓
19-20	51-52	↓	↓	↓	.02	2A Only	↓	↓	L.E. Droop	↓	↓
21-23	53-55	45	↓	↓	.02 → .03	1, 2, 2A	↓	↓	↓	↓	↓
24	56	37.5	↓	↓	.02	2A	↓	↓	L.E. Droop	↓	↓
25-26	57-59	45	45	.023C	.02, .03	↓	↓	↓	Kruger 1	↓	↓
27-29	60-62	37.5	37.5	.023, Conv.	.02, .03	↓	↓	↓	↓	↓	↓
30-31	63-64	25	↓	↓	.02	↓	↓	↓	Kruger 1	↓	↓
32	65-66	37.5	↓	.023C	↓	↓	↓	↓	Kruger 7	↓	Lifting Surface Optimization
33-35	67-69	↓	45	↓	↓	2A	↓	↓	↓	↓	↓
36-37	70-71	↓	45	↓	↓	6	↓	Faired	↓	↓	↓
36,	72-79	↓	37.5	↓	↓	2A	↓	Faired 6	↓	↓	Re Effects
40	82-83	↓	↓	↓	↓	↓	↓	Unfaired	↓	↓	↓
39	80-81	37.5	37.5	.023C	.02	2A	.01042C	Unfaired	Kruger 2	OFF	Optimized Wing

TABLE 2 (Continued)

Initial Configuration: 39 (optimum wing)

Config	Runs	i_s deg	α deg	C_u	q psf	Fences	Inlet and Exhaust Fairings	Horiz. Tail L.E.	Horiz. Tail T.E.	Tail Tip	Purpose
41	84-97	OFF	Range	0 → .50	25, 15	2A	In	OFF	OFF	OFF	Tail Off $C_L - \alpha$
42	98-105	OFF		0 → .30	25, 15			OFF	OFF	OFF	Downwash Pictures
43-47	107-131	-24 → +3			25			Conv.	Conv.	Conv.	Conv. Tail Trim
48	132-136	-24						Drop			Stabilizer Optimization
49-50	137-143	-24, -18		0 → .30				Slat 1	Conv.		
51	144-148	-18		0 → .20				Slat 3	Flap 1		
52-53	149-157	-18, -10		0 → .20		2A		Slat 2			
54	158-159	-18		.05, .10		6	In				
55	160-162	-18		.05 → .15		6	Out				
56	163-165					6 + Tail					
57	166-168					2A				Conv.	Stabilizer Optimization
58	169-171									Drop & Fairing	
59-60	172-177								Flap 1	Inb'd Slot Taped	
61	178-180								Flap 2	Stabilizer Optimization	
62	182-184			.05 → .15					Flap 3		
63	185-188			.05 → .20					Flap 4	Drop & Fairing	
64	190-193						Out			Extension & Drop	
65	196-200	-18		.05 → .20			Jet Simulation			Drop & Fairing	Stabilizer Optimization
66-72	202-231	-24 → +10	Range	0 → .25	25	2A	Out	Slat 2	Flap 4	Drop & Fairing	Trim For Optimized Wing and Horizontal Tail

TABLE 2 (Continued)
Initial Configuration: 69 (optimum wing and horizontal stabilizer) $i_s = -10$ deg

Config	Runs	i_s deg	α deg	C_u	q psf	h_{AV} in.	Pylons	Stcrs	Landing Gear	δ_{rud} deg	Right δ_{sp} deg	ψ deg	Purpose
73	233-235	-10	RANGE	0 \rightarrow 20	25	.016	OFF	OFF	DOWN	0	0	0	Landing Gear Down
74	237-239						ON	OFF					Four Pylons On
75	241-243						ON	ON					Four Stores On
76-77	245-250		RANGE				OFF	OFF					Wing Tip Speed Brakes
78-80	252-262		4	0 \rightarrow 20							10, 30		Spoiler Roll Power
81	266-274			0 \rightarrow 15							20	0	
82-83	275-286		RANGE	0 \rightarrow 20							0	5, 10, 15	Sideslip Effects
84	287-293	-10	4	RANGE						± 35		0 \rightarrow 15	Max. Rudder Power
85-86	295-300	OFF	RANGE	0 \rightarrow 20	25					0		0	Differential Blowing
88-91	305-308	-10	4	RANGE	20, 25								Downwash & $q_{T/q}$
													Coanda Surface
													Imperfections
													Slat L.E. Radius
92	309-310		RANGE	.10, .20	25	.016							Effect
93-94	311-313		4, 10	RANGE	20	.012, .008							Slot Height Variation
95	314-315	-10	4, 10	RANGE	20	.012, .008	OFF	OFF	DOWN	0	0	0	Slat Gap Radius Effect

TABLE 3 - PHASE II TEST PROGRAM SUMMARY

Initial Configuration: 84 from Phase I (optimum wing and horizontal tail plus radii added to slat and slat gap) $h_{AV} = 0.012$ in.

Config	Runs	α deg	C_L	δ_{SLAT} deg	Fences	i_s deg	Horizontal Tail LE & TE	Tail Tip & Droop	δ_{rud} deg	Right δ_{sp} deg	ψ deg	Fuse- Drag Brakes	h_g/c	Purpose
96	317-323	RANGE	RANGE	37.5	2A	-10	Slat 2, Flap 4	ON	0	0	0	IN	∞	Phase I Comparison
97	325-328		0 \rightarrow .3	25.0	2A									$\delta_{SLAT} = 25^\circ$, Increased
98	329-334				2B									L.E. Radius
100	341-344													Fences Moved In, Slot
101-102	345-352		0 \rightarrow .3			-10	Slat 2, Flap 4					IN		Shortened
103-105	353-362		-1, .2, .3			-10, -15	Slat 2, Flap 4, Flap 5	ON				OUT		Air Supply Line Pairings
106	364-373		0 \rightarrow .3			OFF	OFF	OFF						Fuse. Drag Brakes
107-114	374-408		0 \rightarrow .3			-24 \rightarrow +10	Slat 2, Flap 5	ON			0			Horiz. Stab. Mods.
111	409-420		0, .15, .3			-10			0		2.5 \rightarrow 15			Tail-Off Data
115	421-435													Tail-On Trim Data
116-117	436-439		0, .3			-10	Slat 2, Flap 5		-35		0 \rightarrow 15			Sideslip Effects
118	441-445		0 \rightarrow .3			-15	GAC-1		-20, -10		0			Rudder At Sideslip
119	447-449					-15	GAC-2		0					Rudder Effects At $\psi = 0$
120	450-452					-15	GAC-3							Horiz. Tail Mods.
121-128	453-478	RANGE	0 \rightarrow .3			-24 \rightarrow +10						OUT		Horiz. Tail Mods.
129	479-486	4, 12	RANGE			-10			0	30	0 \rightarrow -15	IN		Trim Data, Drag Brakes In
130	487-494	4, 12	RANGE			-10			-35					Spoiler At Sideslip
121-128	453A-478A	RANGE	0 \rightarrow .3			-24 \rightarrow +10			0					Rudder & Spoiler At Sideslip
131-138	495-518												3.091	Trim Data In Ground
139-146	519-543	RANGE	0 \rightarrow .3	25.0	2B	-24 \rightarrow +10	GAC-3	ON					1.645	Trim Data In Ground
									0		0	IN	0.833	Trim Data In Ground

TABLE 4 - PHASE III TEST PROGRAM SUMMARY

Initial Configuration: 140 from Phase II (Modified Wing, GAC-3 Tail, $h_{AV} = 0.012$ in.) Gear Down, Pylons & Stores Off, Speed and Drag Brakes Retracted

Config	Runs	q psf	α deg	C _D	Fences	i_s deg	δ_{rud} deg	Right δ_{sp} deg	Horizontal Stabilizer	Tip Droop & Pairing, Gap Radius On Tail	Purpose
147	545-559	25	RANGE	0 → Max	2B	-10	0	0	GAC-3	ON	Phase II Comparison
148-149	560-565				2C	-10			GAC-3	ON	Wing Inb'd Fence & Gap
150	567-576			0 → Max		OFF			OFF	OFF	Radius Removed
151-157	578-610			0 → 30		-24 +10			EC-20		Tail Off Data, Final Wing
160-161	611-626			.10 → .30		-18, -24			EC-20-SS		Horiz. Stab. Mode.
158-159	611-616			.10 → .30		-24 → +3			EC-40		
162-165	627-640			.10 → .30		-24 → +3			EC-40RA		
166-169	641-648			0 → .30		-24 → +3			EC-40-10		
170-172	649-654					-24 → +7			EC-40-10-SS		
173-174	655-658					-10		0			Horiz. Stab. Mods.
175-182	659-695	25	RANGE								Pos' Stall Data
183-185	696-705	15, 25	EXT. RANGE								
186-188	706-720	15	EXT.				0	10, 20, 30			
189	721-725	15	RANGE				-35	20			Po Max
190	726-730	25	RANGE								Stall Spoiler Power
191-197	732-751	25	RANGE	0 → .30		-10	0	0	EC-40-10-SS		Max Rudder, Post-Stall
						-24 → +7			EC-40-10-D		Flow Thru Engine Effect
198	752-755	15	RANGE & REVERSE	.10 → .30	2C	-10	0	0	EC-40-10-D	OFF	Final Tail, Trim Data
											Stall Hysteresis

TABLE 5 - PHASE IV TEST PROGRAM SUMMARY

Initial Configuration: 198 from Phase IIIJ (Modified Wing, EC-40-10-D Tail, $h_{AV} = 0.012$ in.) Gear Down, Flow Thru Engine Ducts, Pylons and Stores Off, Speed and Drag Brakes Retracted, $q = 25$ psf, $C_\mu = 0.0$, $\delta_{sp} = 0$ deg

Config	Runs	α deg	i_s deg	δ_{rud} deg	Horizontal Stabilizer	ψ deg	Airline Crossover Ducting	Purpose
199-200	757-758	0 \rightarrow 25	+3, -24	0	EC-40-10-D	0	OFF	Comparison To Phase IIIJ
201-203	759-762		+3, -10, -24	-35				Max Rudder Power With EC-40-10-D Tail
			+3, -5, -24	0, +35	EC-40-10-D			Flow Visualization
204-206	764-766		+3, -10, -24	0	GAC-6			Horiz. Tail Mode
207-215	768-776		+10 \rightarrow -24	0	GAC-6RA			Final Stab. Trim Data
216-217	777-778		+3, -24	-35				Max. Rudder Power With GAC-6RA Tail
			+3, -24	-35			OFF	Flow Visualization
218-220	780-783		+3, -10, -24	0		0, +15	ON	Airline Crossover Ducting
221-222	785-791	0 \rightarrow 25	-10	0	GAC-6RA	0, 15	ON	Air Hose Sideslip Tares

TABLE 6 - PHASE V TEST PROGRAM SUMMARY

Initial Configuration: Shortened Slot (W.W. 56.1 to 265.5), $h_{AV} = 0.0072$ in., outboard fence at W.S. 265.5 (Fence 2D),
Modified plenum with screws nearer to slot, Gear Down

Runs	q psf	α deg	C_L	i_s deg	ψ deg	Yaw Jets	δ_{rud} deg	δ_{sp} deg	Air Inlet Scoop	Splitter Flap	Purpose
800-803	20, 25	4, 12	0 → Max	-10	0	Off	0	0	Off	Off	En vs. C_L Calibration
804-807	20	Range	0 → .255			Off			Off		Comparison to Phase III
808-830			0, .075, .255						On & Off		Conversion to Final Wing, Fences, Ducting, Fairings and Scoops
831-833			0, .075, .255	-10		On, Closed			On		Add Dummy Yaw Jets
834-842			0 → .37	Off							Final Configuration, Tail-Off Data
998-1000											Final Configuration Trim Data
843-875			0, .05, .1, .2, .3	-24 → +7							Tail Stall Investigation
876	20	Range	.05, .1, .2, .3	-15, -18, -24		On, Closed					Static Forces Due to Yaw Jet
878, 884	0	0	Range	-10		Left Open					Yaw Jet Performance
881-883	20	4, Range				Left		10, 20			Adverse Yaw
885-895						Open		30			Spoiler Power, Yaw Jet Closed
915-917						On, Closed	0	10, 20, 30			Spoiler, Rudder & Yaw Jet
888-891							-15, -35	30			Rudder Power
964-967		4, Range	Range			Left Open	-7.5, -15, -35	0			Stab. Effect on Rudder
896-901		Range	0, .1, .3	-10	0	On, Closed	0, -35				Rudder Power at Sideslip
902-910		Range					0, -35				Rudder, Spoiler and Yaw Jet at Sideslip
911-914			0, .30	+7, -24	0, +15						Wing Tip Drag Brake
956-963		Range	0, .10, .30	-10	5, 10, 15	On, Closed	0 → -35	0			Splitter Flap
970-955		4	Range		5, 10, 15, -15	Left Open	-35	30			Static Pressure at Air Scoop Inlet
968-971		Range	Range		0	Left Open	0	30, 0		Off	Final Air Inlet Scoop
973-979		4, Range	Range			Open					
986-995		Range	0, .1, .3	-24, -10, +3		Off		0		On, 45°	
877, 996, 997			0, .30	-10						Off	
1001-1006	20	Range	0, .075, .255	-10	0	Off	0	0	On	Off	

TABLE 7 - 1/8.5-SCALE A-6/CCW MODEL TRAILING
EDGE PARAMETERS, BLOWING OFF

Phase	W S	c, in.	r, in.	h, in.	h/r	r/c	h/c
I	55.5	18.886	.6842	.0211	.030857	.036229	.001118
↓	270.0	8.973	.3251	.0100	↓		↓
I	162.75 (Avg.)	13.930	.5047	.0156	.030857		.001118
I	55.5	18.886	.6842	.0106	.015429		.000559
(Runs 312, 313)					↓		↓
↓	270.0	8.973	.3251	.0050	↓		↓
I	162.75 (Avg.)	13.930	.5047	.0078	.015429		.000559
(Runs 312, 313)							
I	55.5	18.886	.6842	.0158	.023143		.000838
(Run 311)					↓		↓
↓	270.0	8.973	.3251	.0075			
I	162.75 (Avg.)	13.930	.5047	.0117			
(Run 311)							
II, III, IV	55.5	18.886	.6842	.0158			
↓	267.0	9.112	.3301	.0076	↓		↓
II, III IV	161.3 (Avg.)	13.999	.5072	.0117	.023143		.000838
V	56.09	18.885	.6842	.0096	.014060		.000509
↓	265.50	9.181	.3326	.0047	↓		↓
V	160.80 (Avg.)	14.033	.5084	.0071	.014106	.036229	.000509

slot length for phase I (W S 55.5 to 270.0)

= 25.59 in. per wing

slot length for Phases II, III, IV (WS 55.5 to 267.0)

= 25.24 in. per wing

slot length for Phase V (W S 56.1 to 265.5)

= 24.99 in. per wing

slot sweep angle

= 9.6 deg

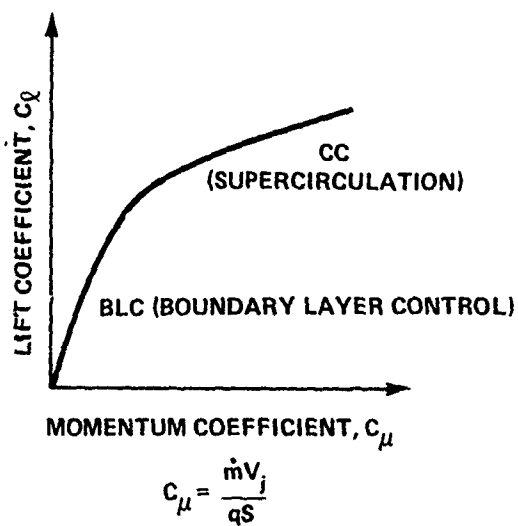
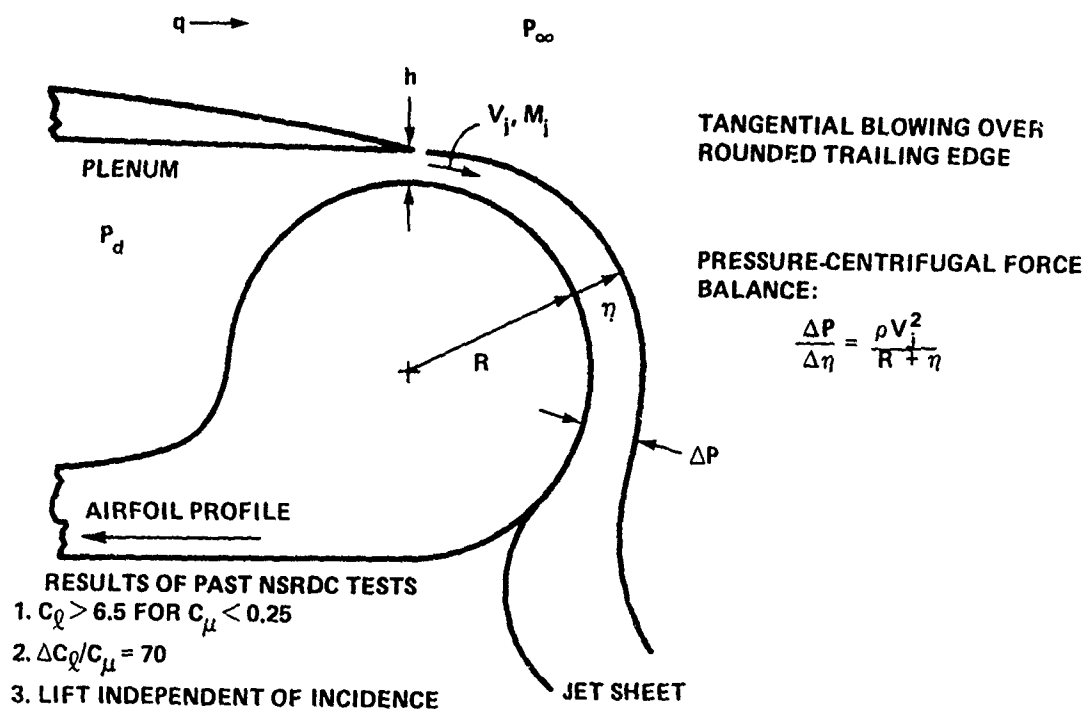


Figure 1 - Basic Circulation Control
Aerodynamics and Parameters

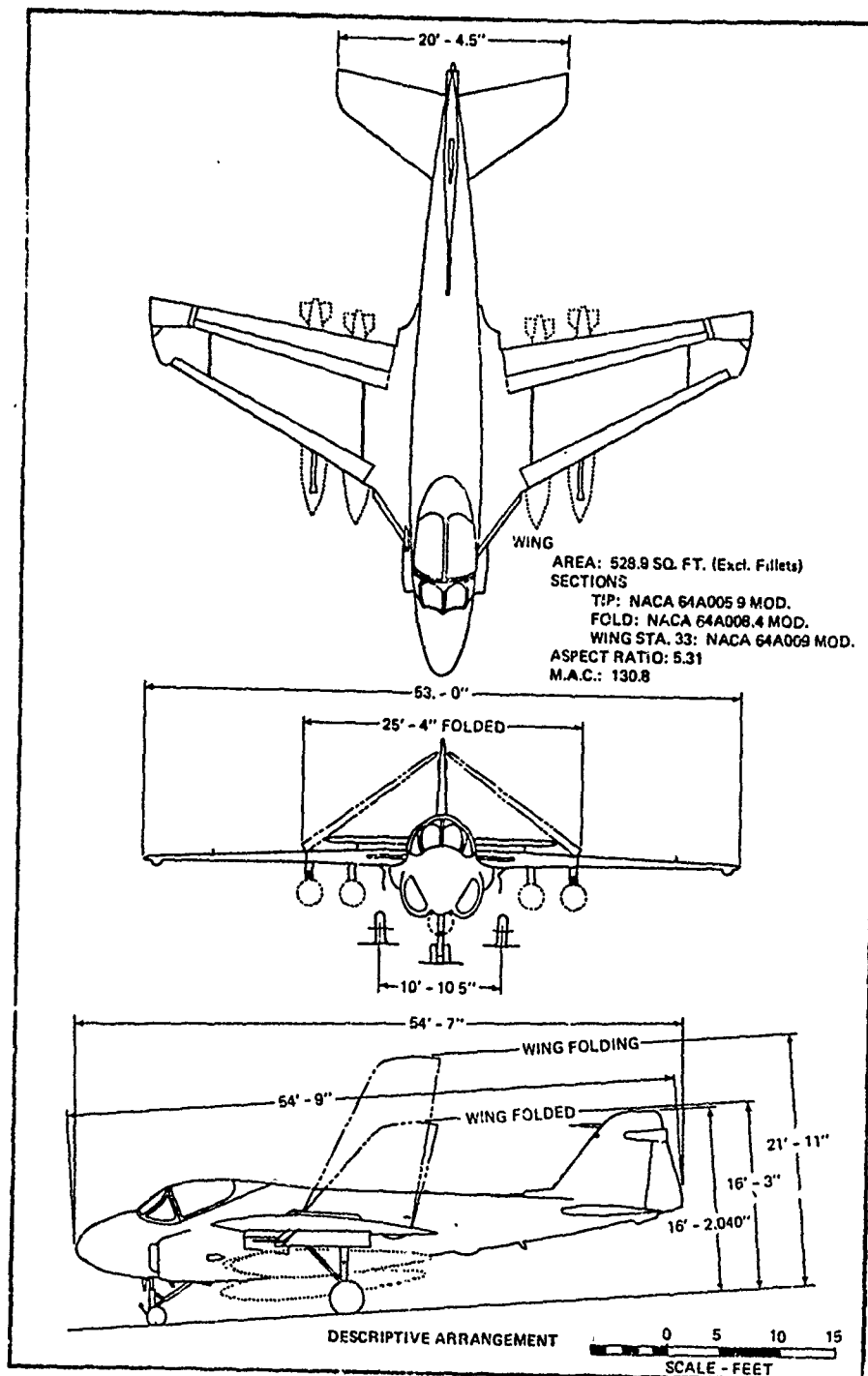
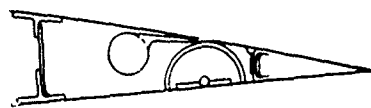
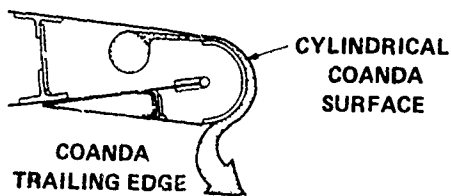
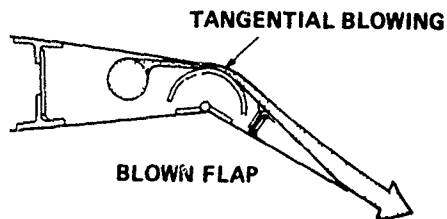


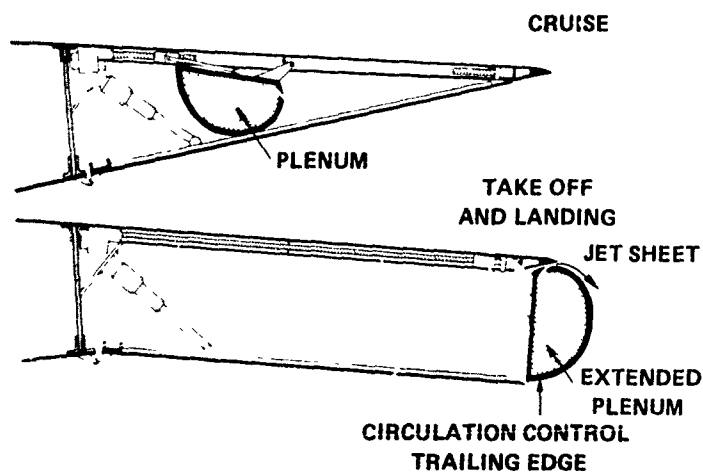
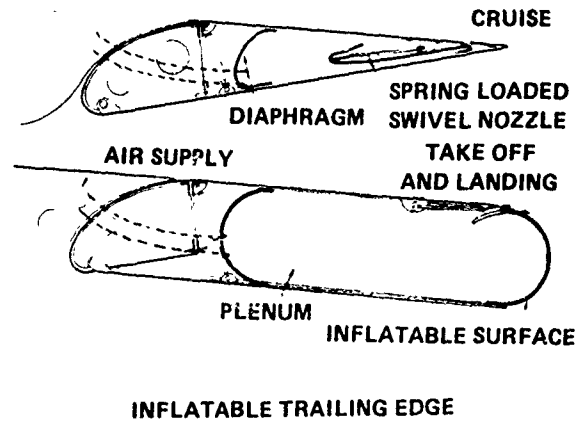
Figure 2 - Three-View of the A-6A Aircraft
 (from NAVAIR 00-110AA6-5)



CONVENTIONAL



180 DEGREE FLAP ROTATION
TO EXPOSE ROUNDED
TRAILING EDGE



EXTENDED TRAILING EDGE

Figure 3 - Proposed Circulation Control
Wing Configurations

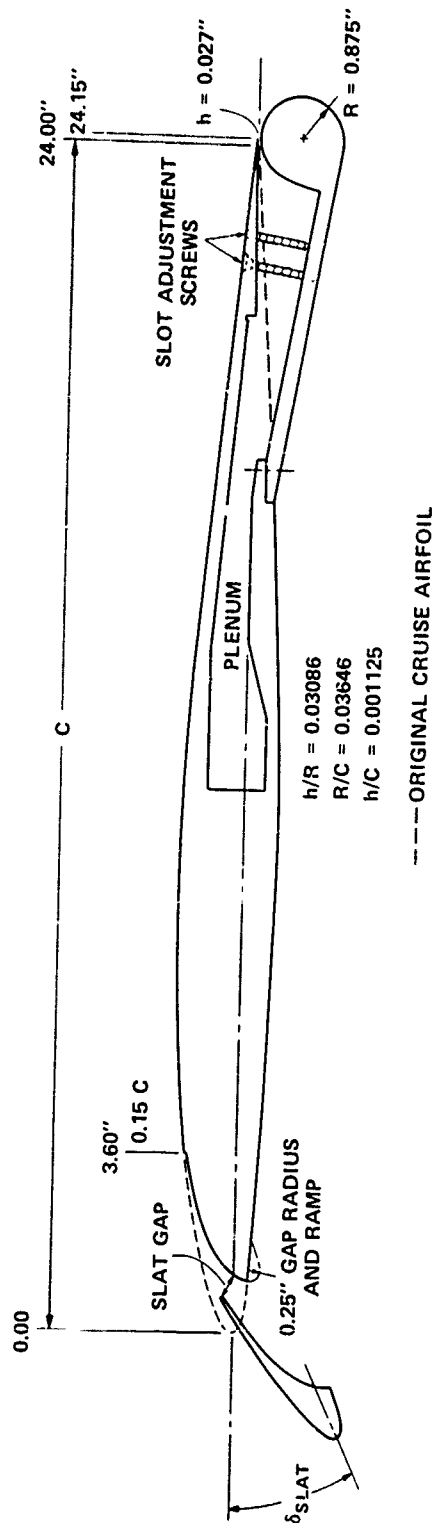


Figure 4 - NACA 64A008.4/CCW Two-Dimensional Airfoil Geometry and Parameters

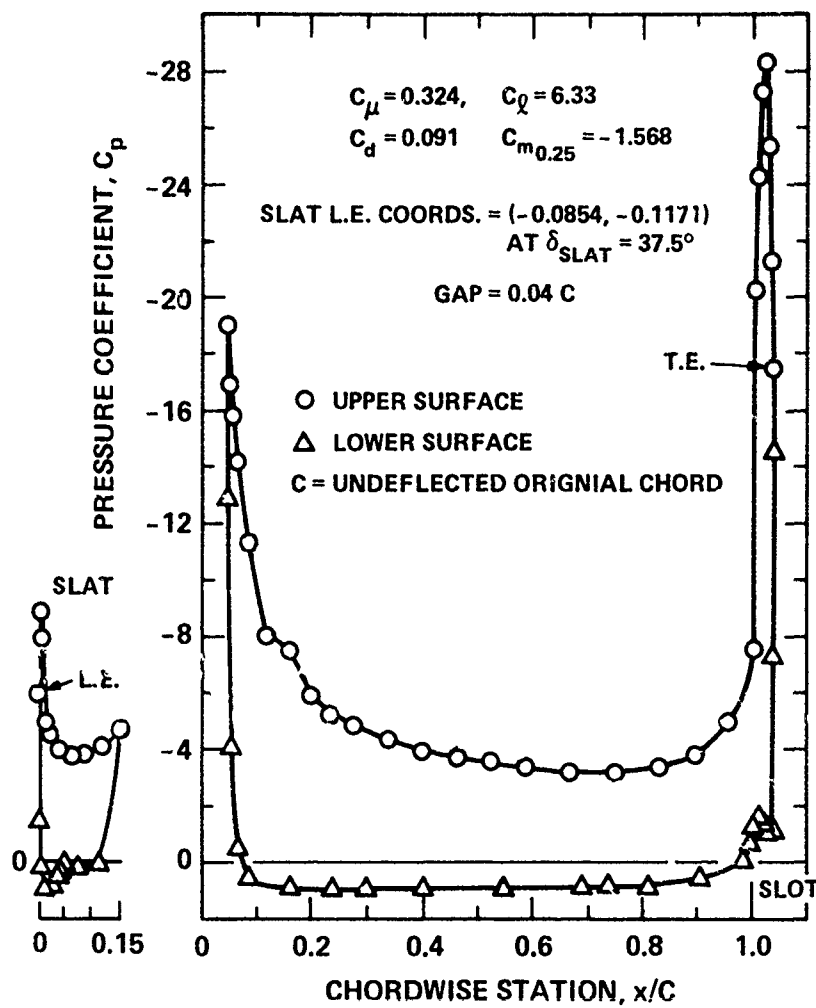


Figure 5 - NACA 64A008.4/CCW Airfoil Static Pressure Distribution at $\alpha_{\text{geo}} = 6^\circ$

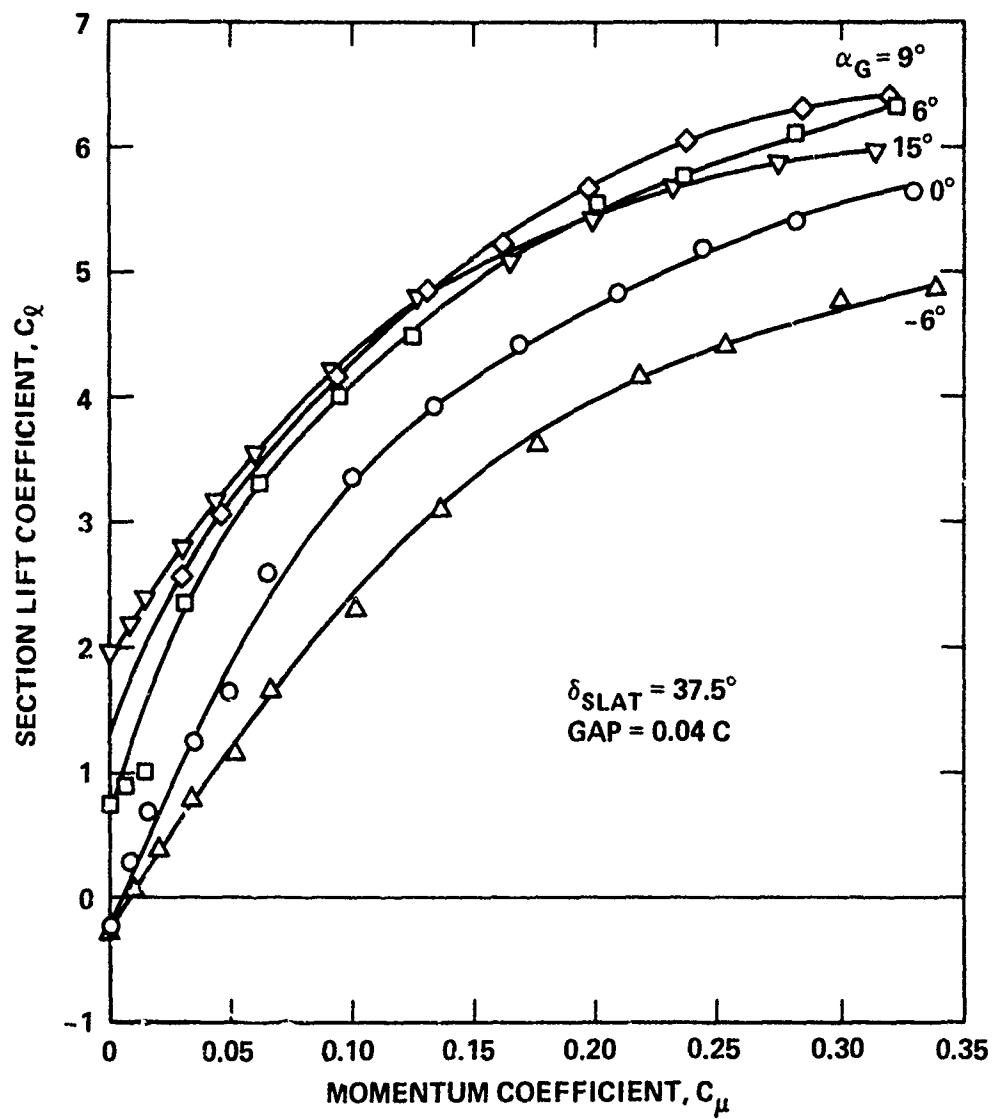


Figure 6 - Two-Dimensional Lift Characteristics of the NACA 64A008.4/CCW Airfoil

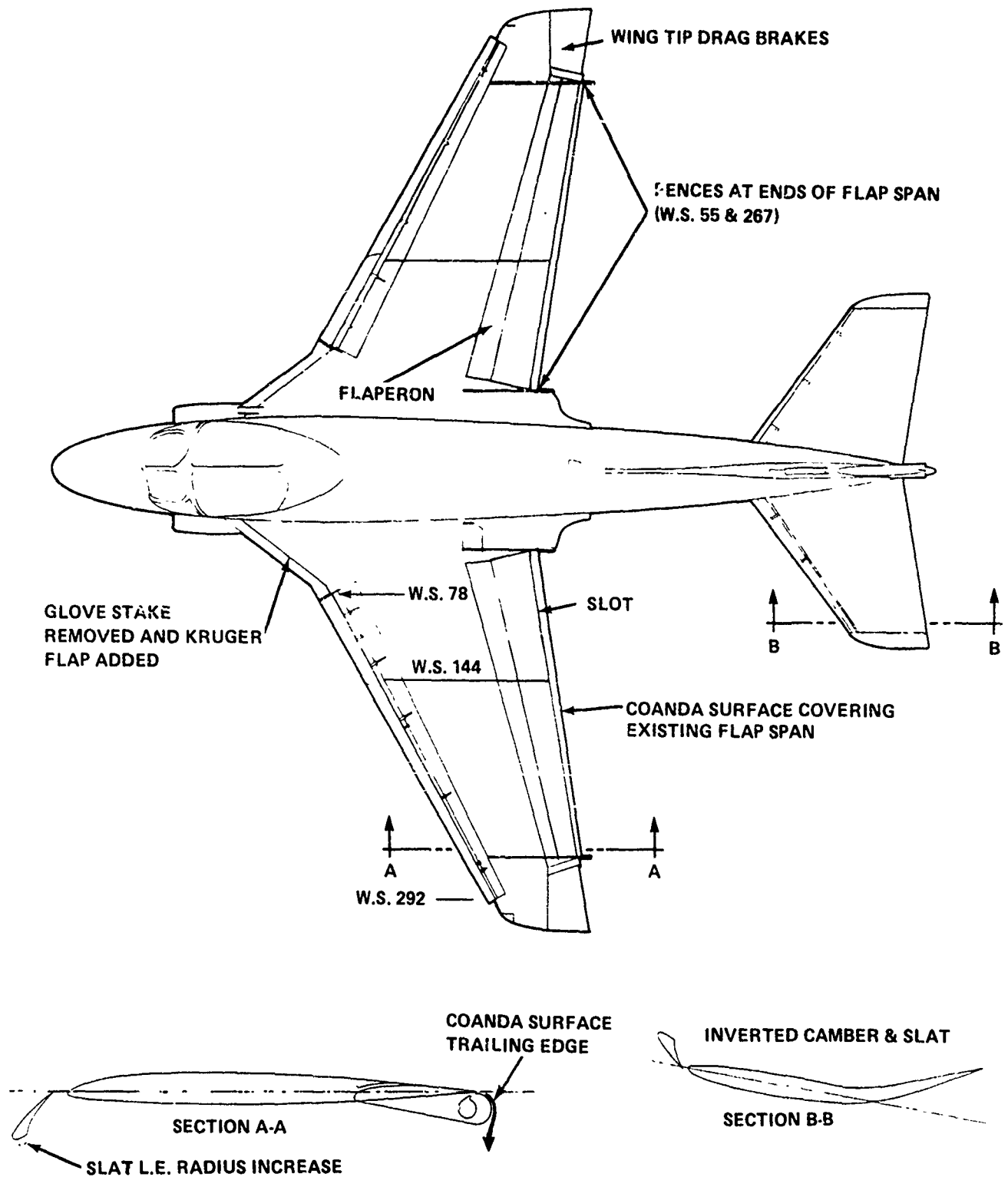


Figure 7 - 1/8.5-Scale A-6/CCW
Model Modifications

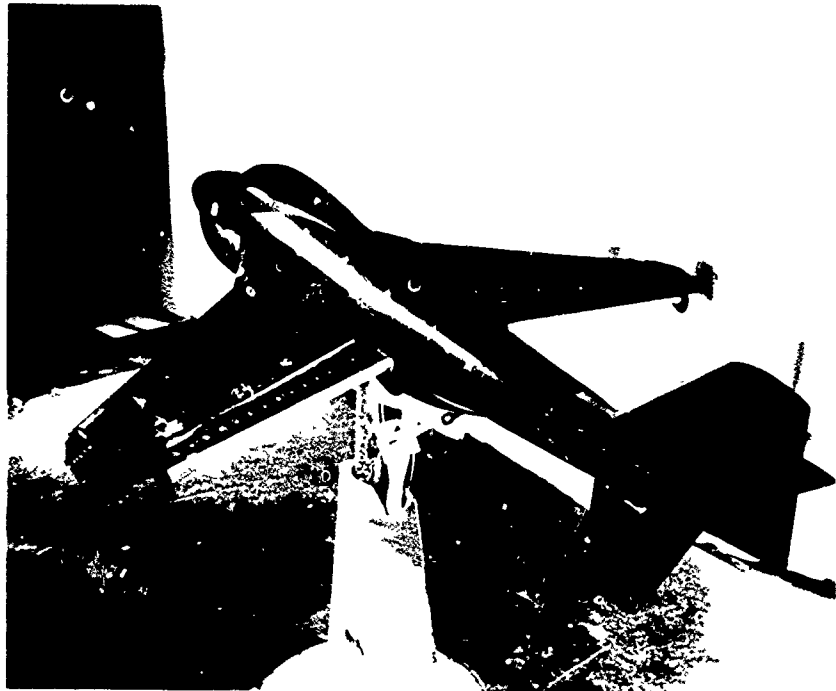


Figure 8 - 1/8.5-Scale Model Installed in 8- by 10-Foot
North Subsonic Tunnel, Phase I



Figure 9 - Trailing Edge Modification, and Cotton-Tuft
Showing Jet Turning (Wind Off)

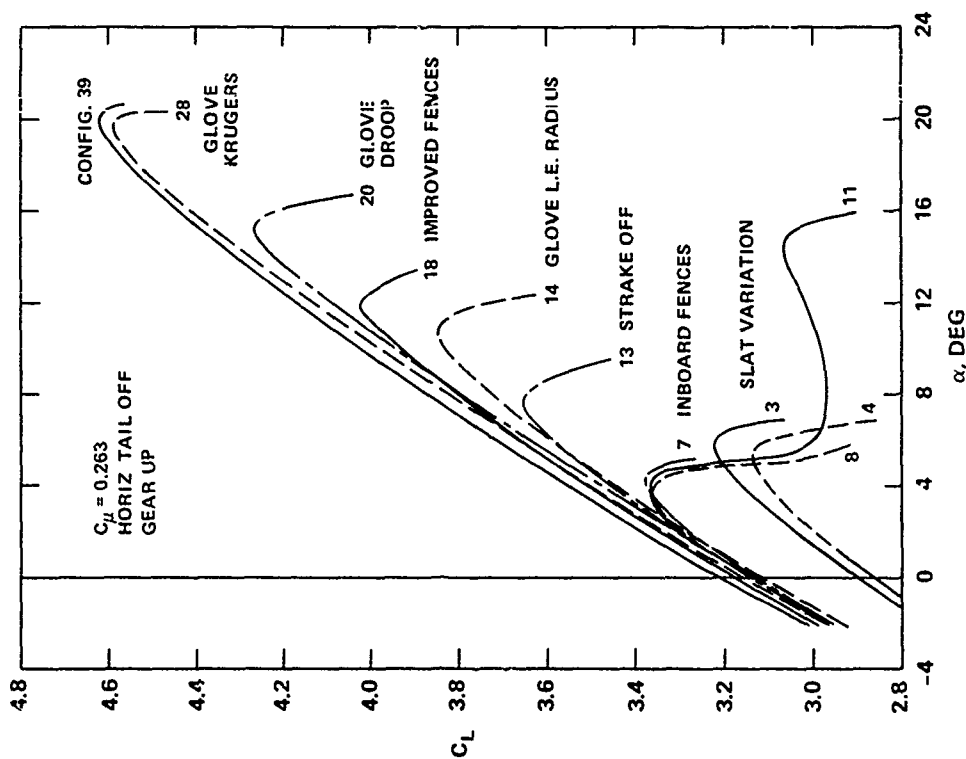


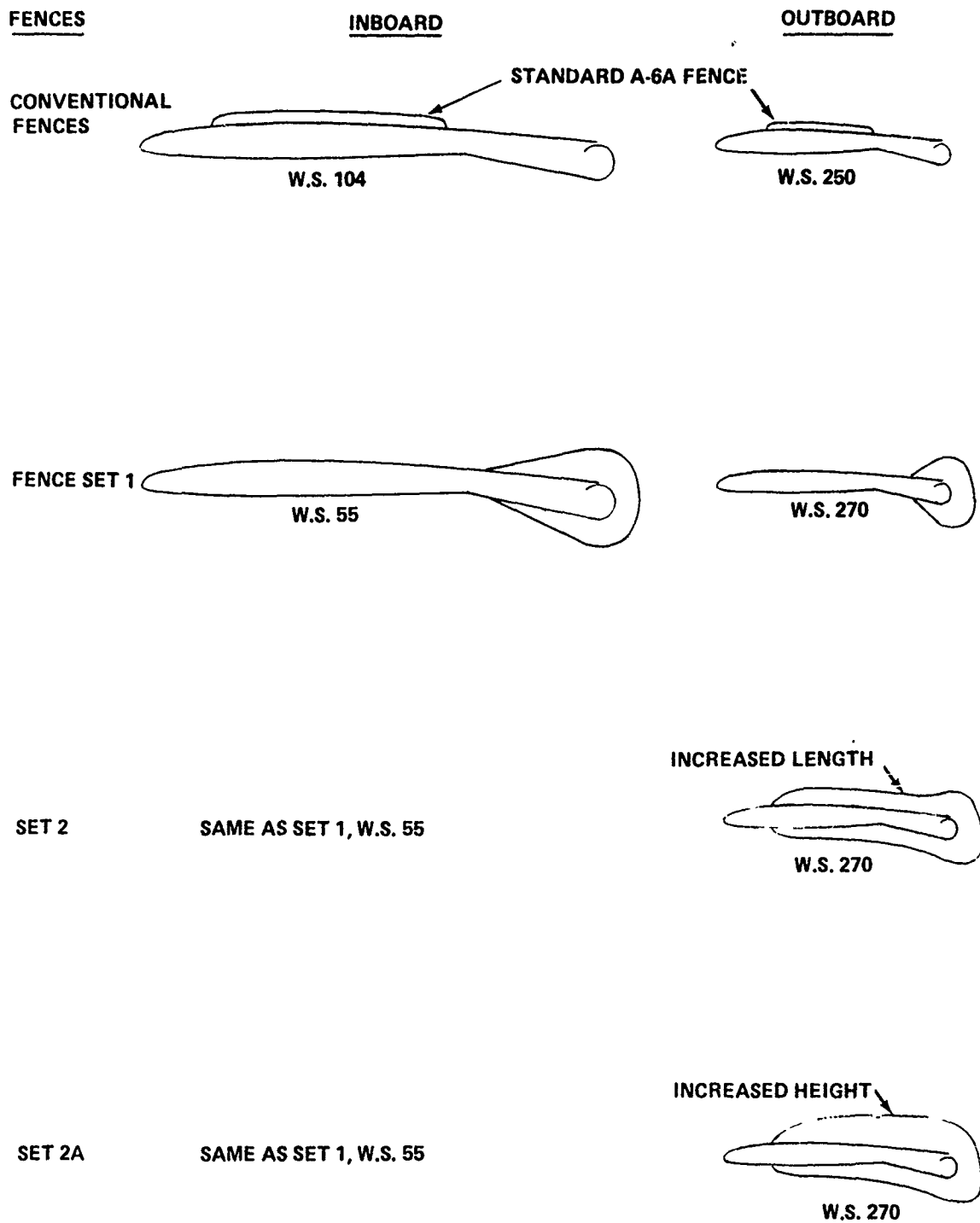
Figure 10 - A-6A/CCW Lifting Surface Improvement,
Tail Off, $C_{\mu} = 0.263$

Configuration Identification

Config	δ_s	Slat LER	gap/C	Fences	Wing Glove Leading Edge
3	25	Con.	.02	Con.	Con.
4	37.5				
7	↓		.04	Con. & Set 2	
8	45	↓	.02		
11		Inc.			↓
13					Stroke Off
14					LER Inc.
18				Set 2A, Con. Off	
20	↓	↓			Droop
28	37.5	Con/Inc*			Kruger 1
39	↓	Inc.	↓	↓	Kruger 2

LER = Leading Edge Radius Inc. = Increased
Con. = Conventional * = Inboard/Outboard

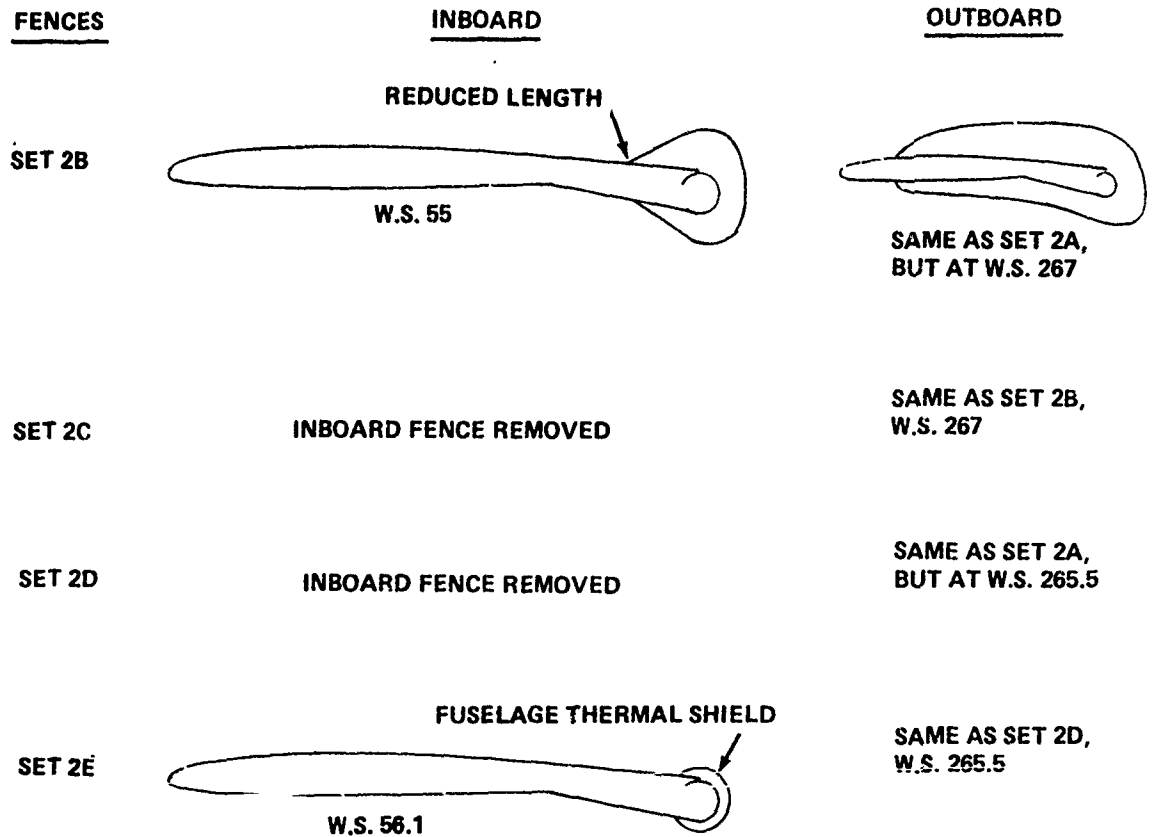
Figure 11 - Details of Wing Flow Fences



NOTE: LEADING EDGE DEVICES AND DEFLECTIONS NOT SHOWN

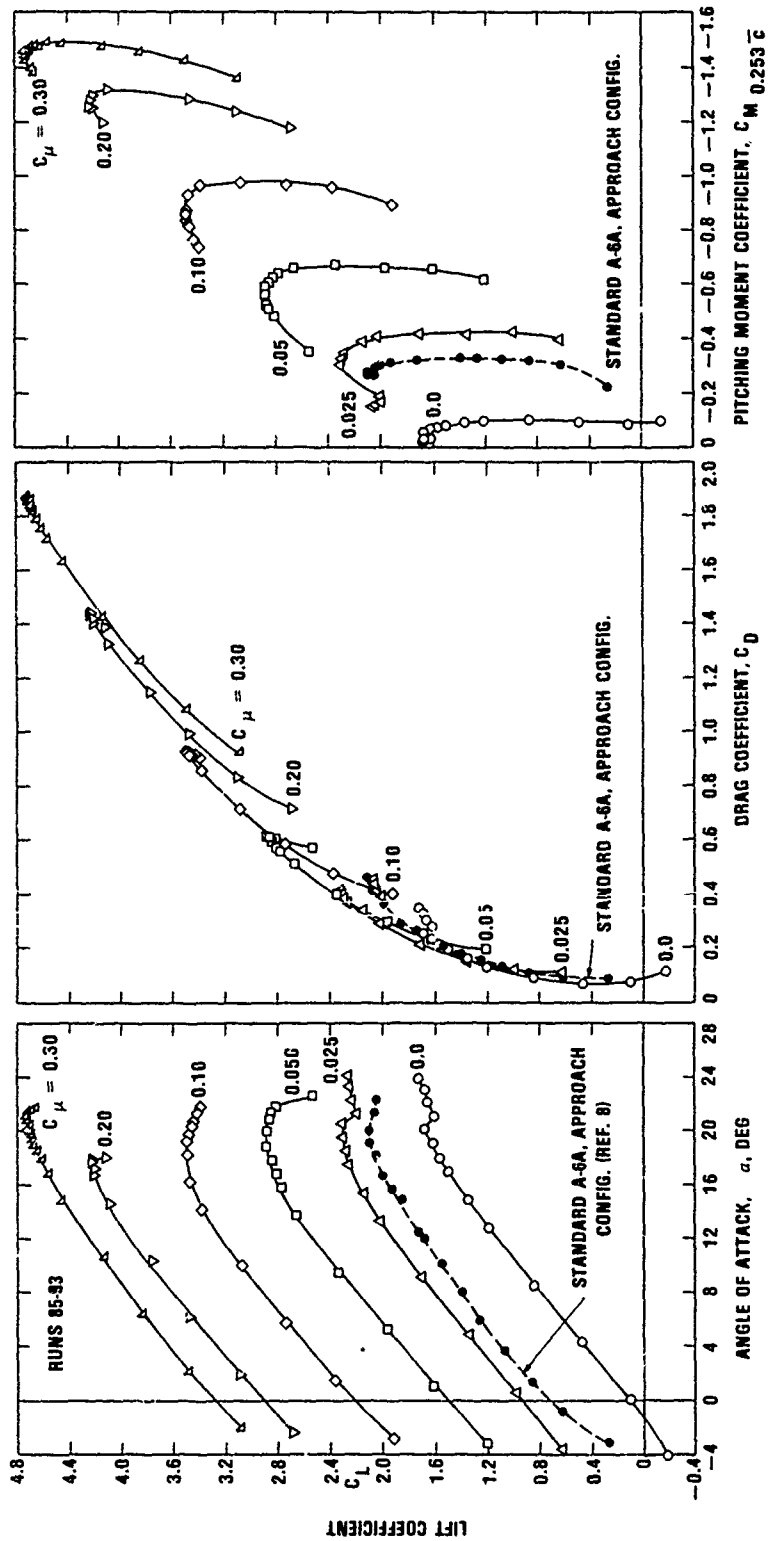
Figure 11a - Conventional Fences and Sets 1 through 2A

Figure 11 (Continued)



- SET 2F = SET 2E WITH STRUCTURAL SUPPORT BASE ON OUTBOARD FENCE
 SET 3 = SET 1 WITH OUTBOARD FENCE REMOVED
 SET 5 = SET 2A WITH SMALL FENCES BETWEEN K RUGER AND SLAT L.E. DEVICES
 SET 6 = SET 2A WITH INBOARD FENCE REMOVED

Figure 11b - Sets 2B through 6



$q = 25 \text{ psf}$, $h_{AV} = 0.0156 \text{ in.}$, $\delta_{SLAT} = 37.5 \text{ deg.}$

Figure 12 - A-6/CCW Tail-Off Aerodynamic Characteristics, Phase I

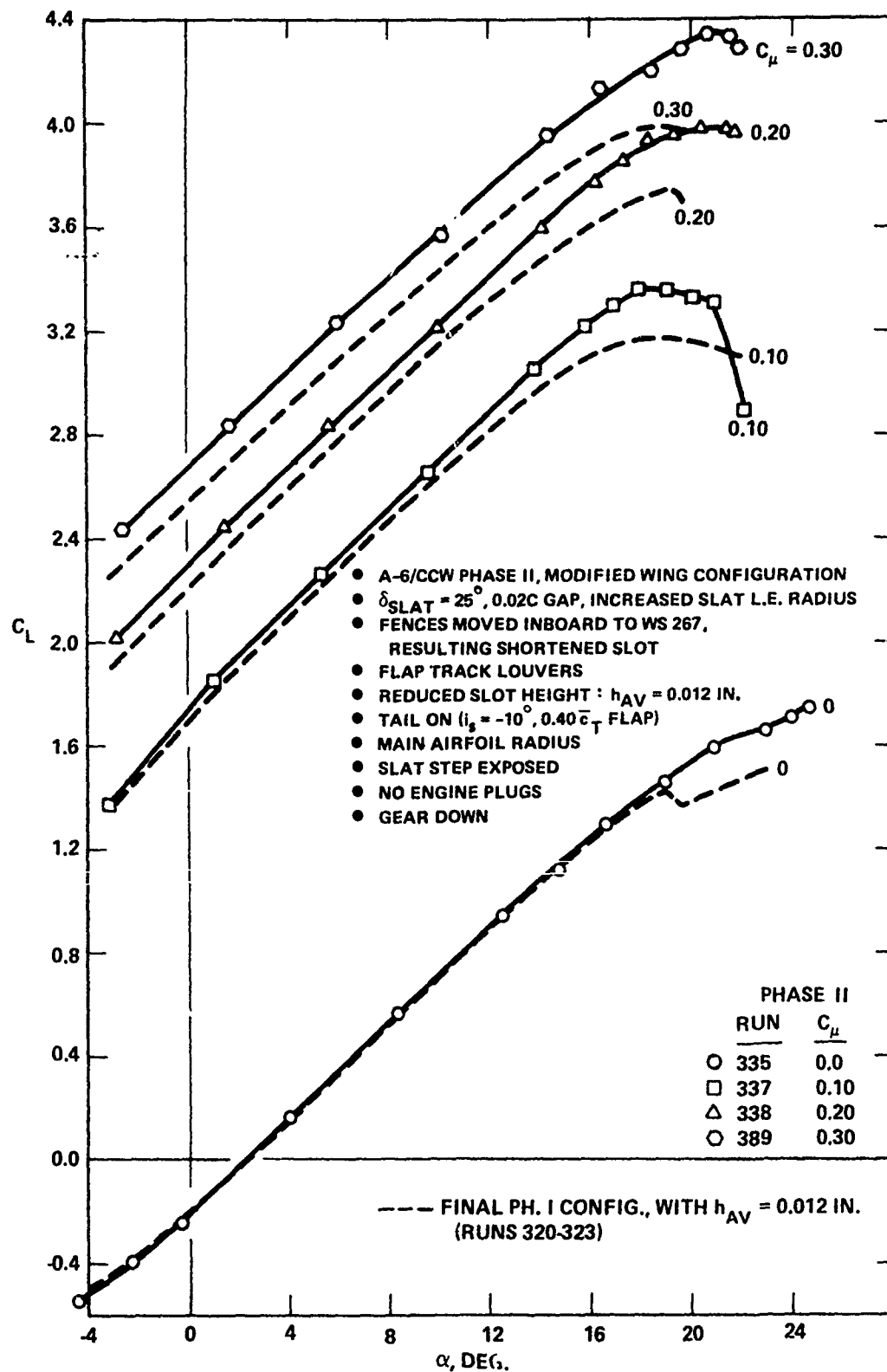
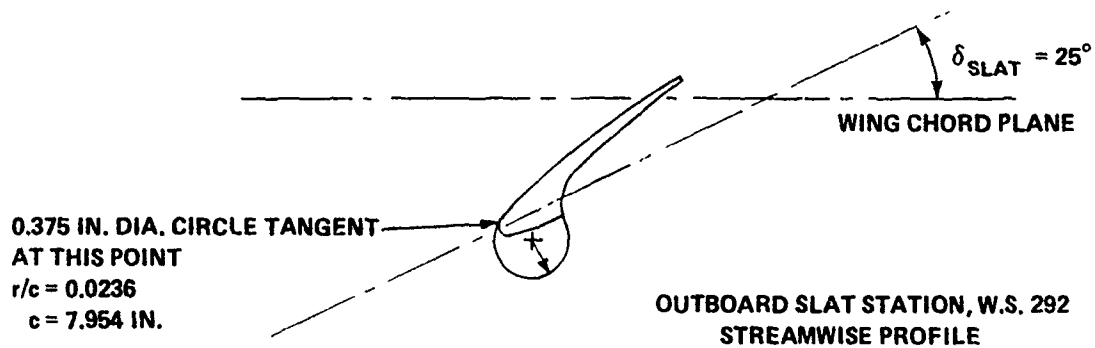
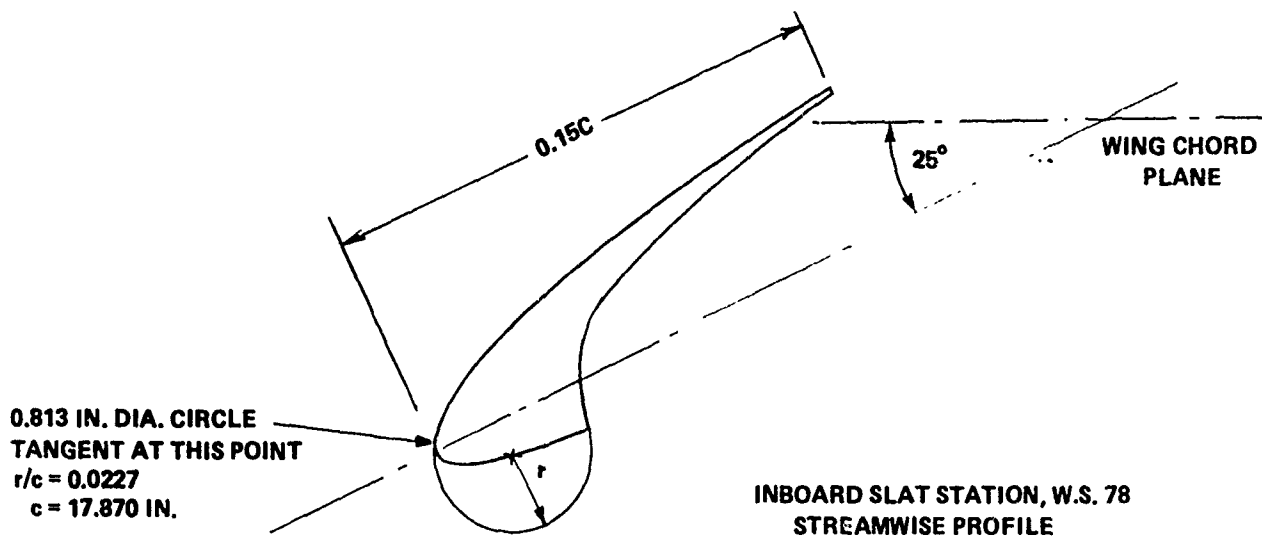


Figure 13 - Phase II Lifting Surface Modifications



DIMENSIONS ARE 1/8.5-SCALE

Figure 14 - Slat Leading Edge Radius Increase

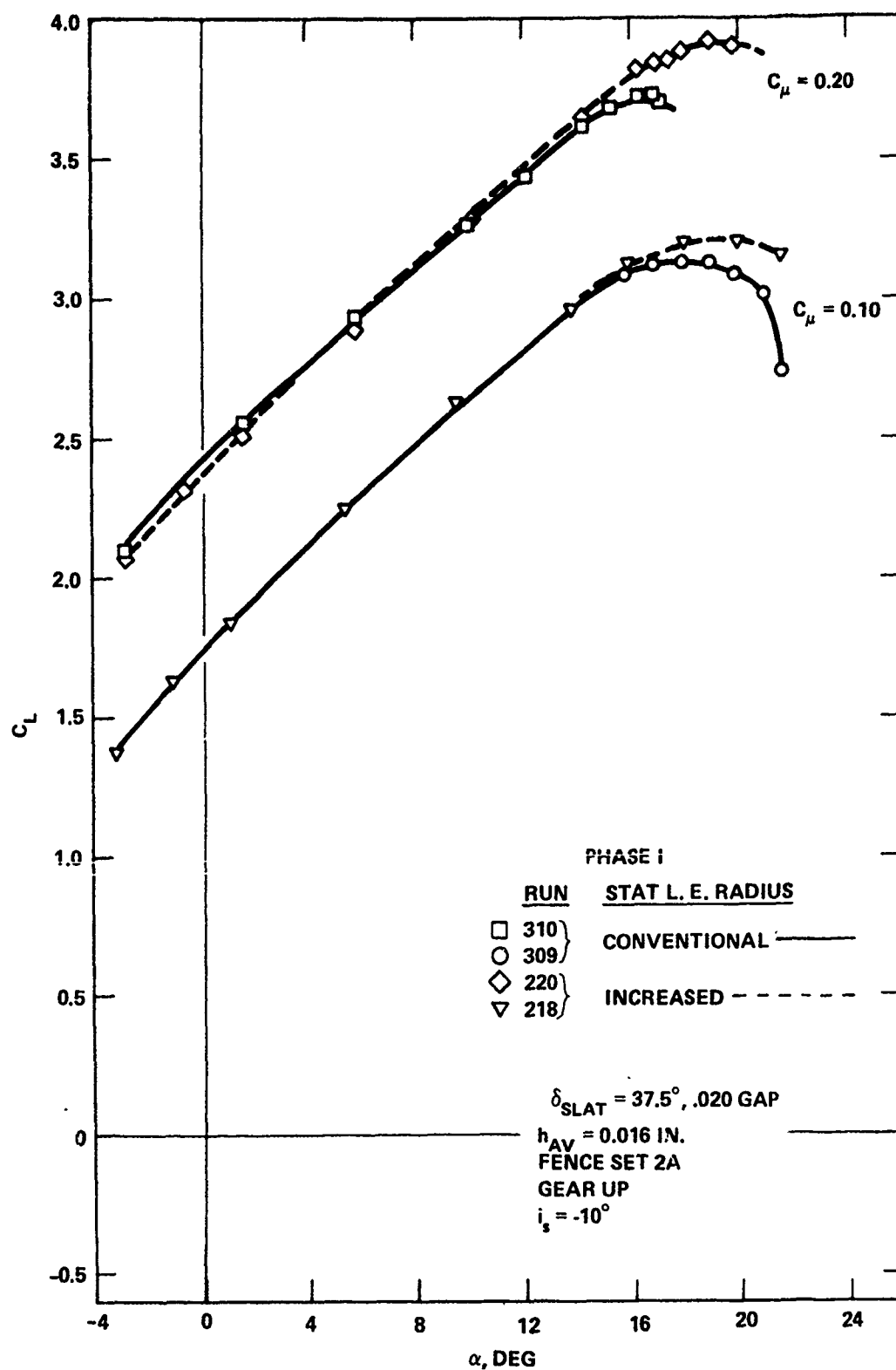


Figure 15 - Effect of Increase in Wing Slat Leading Edge Radius

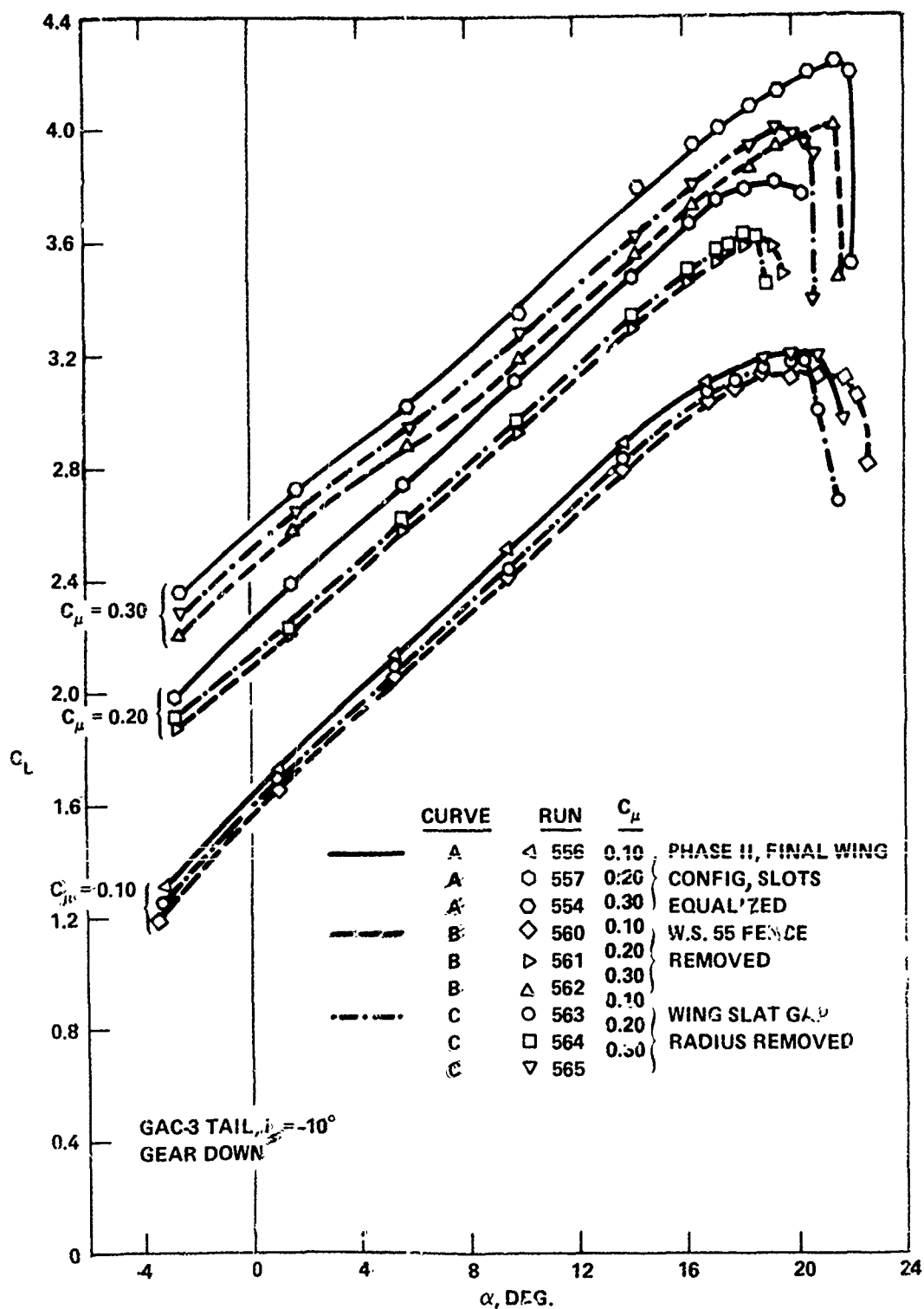


Figure 16 - Conversion to Phase III Lifting Surface Configuration

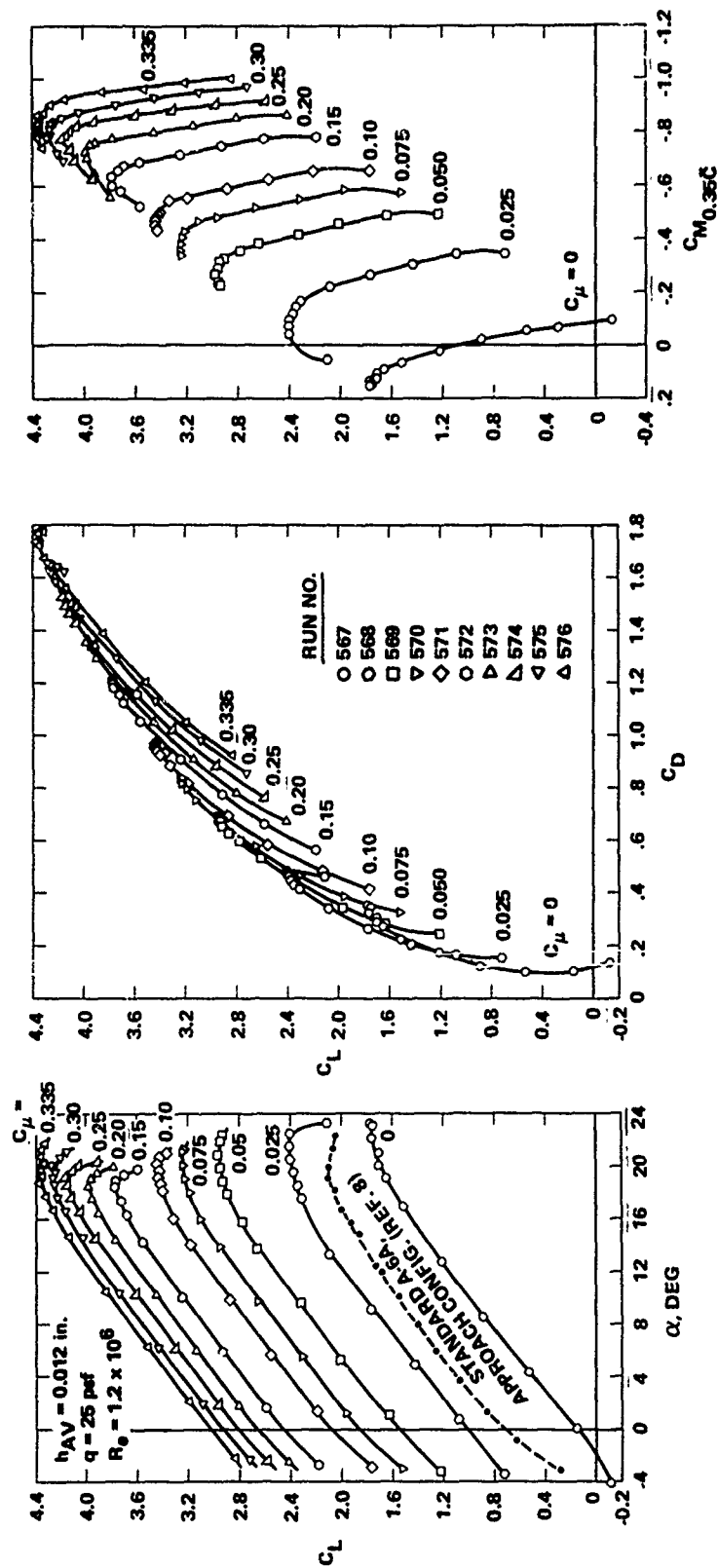


Figure 17 - Phase III Final Wing Configuration Aerodynamic Characteristics, Tail Off

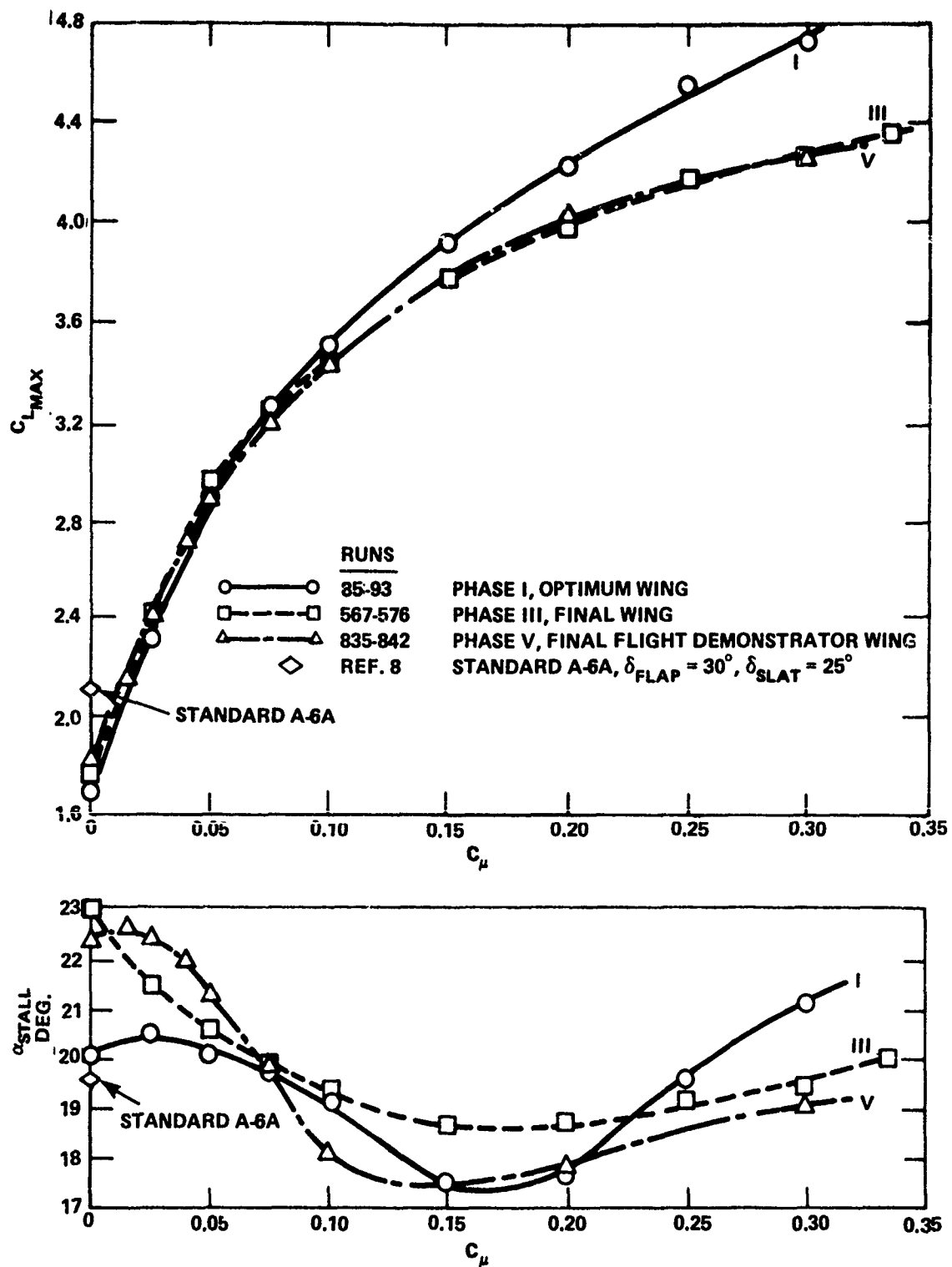


Figure 18 - Comparison of Tail-Off $C_{L_{max}}$ and Stall Angle for Various Configurations

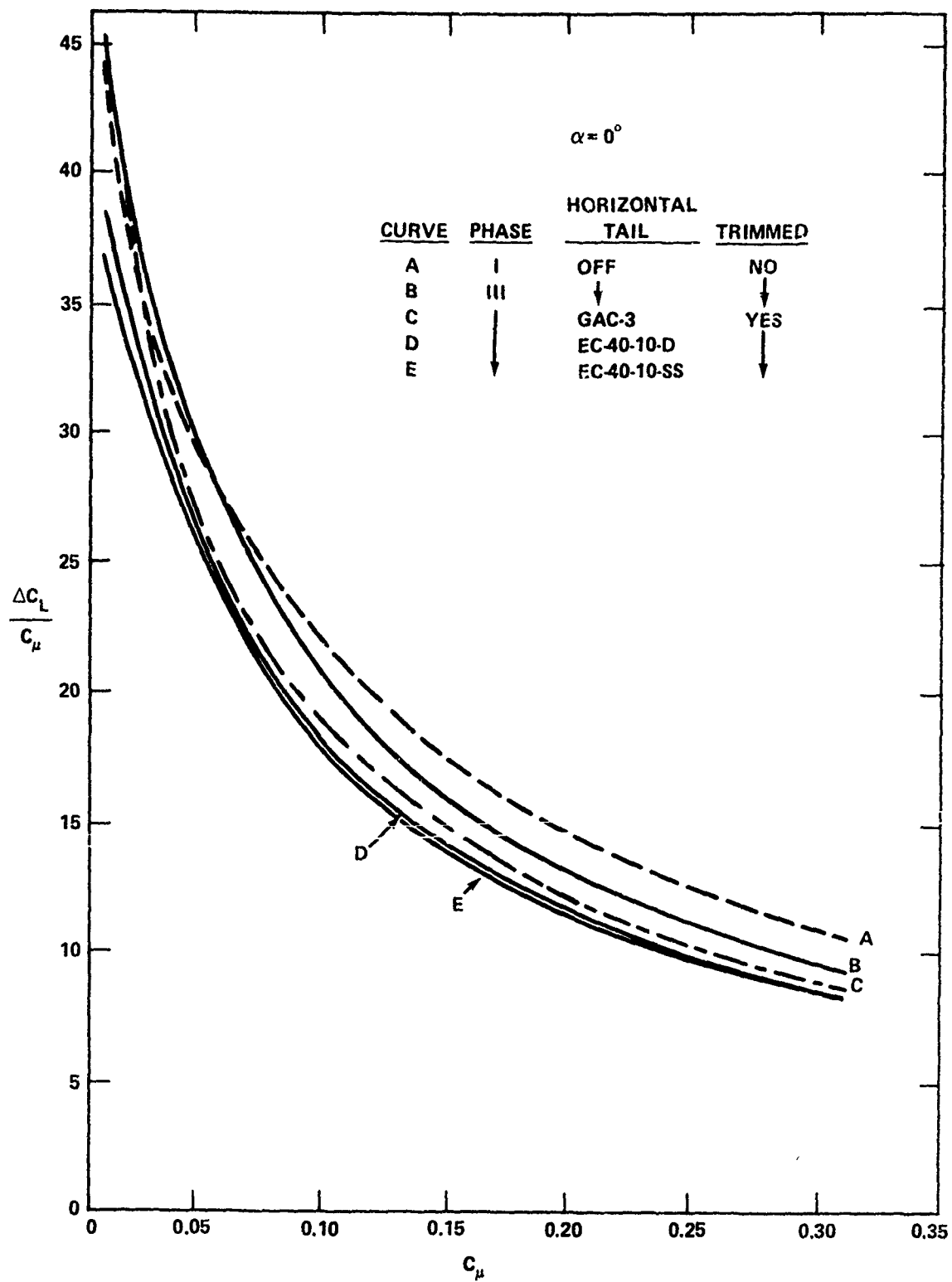


Figure 19 - Lift Augmentation as a Function of Momentum Coefficient

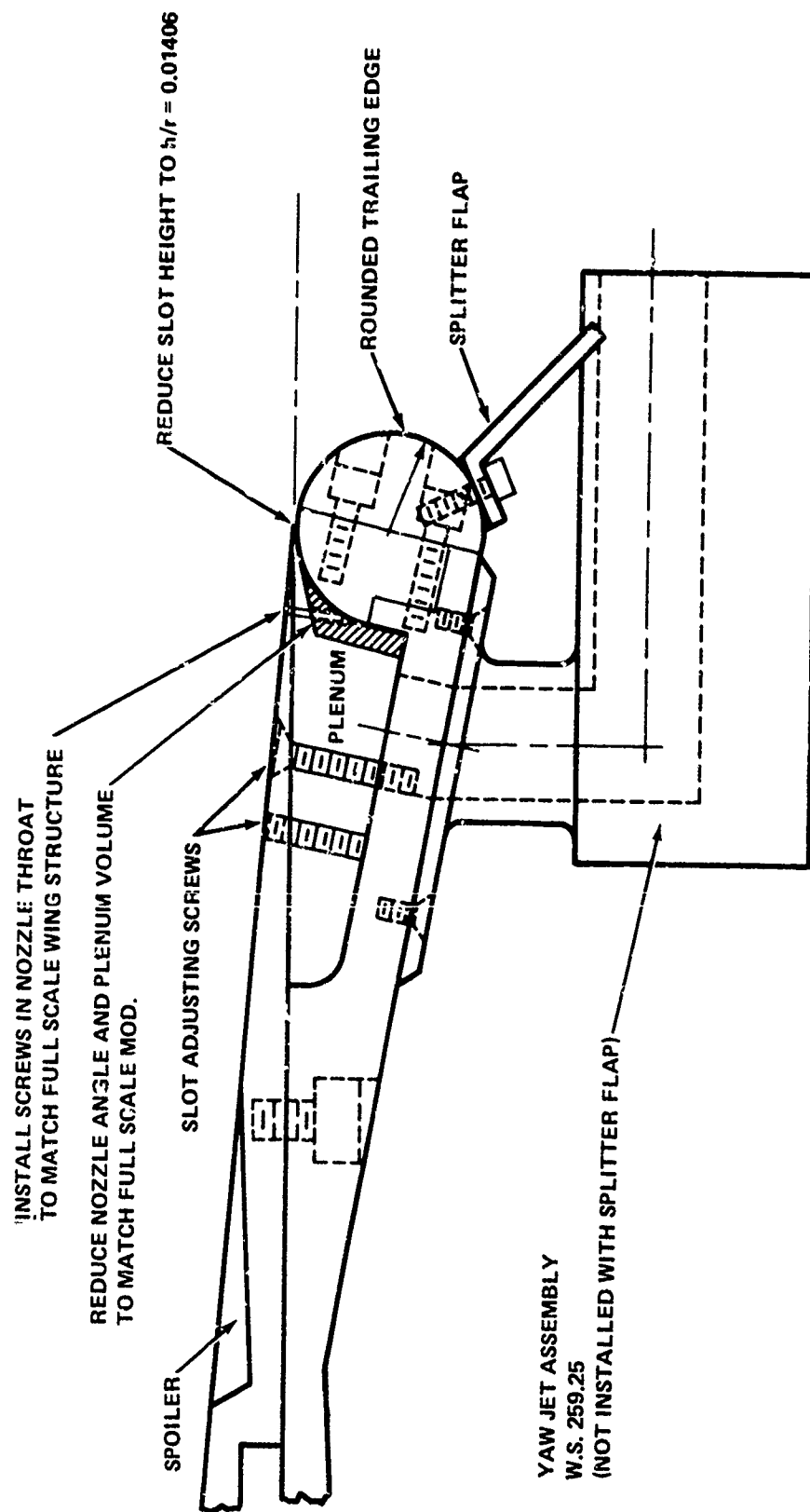


Figure 20 - Phase V Modifications to the Wing Trailing Edge

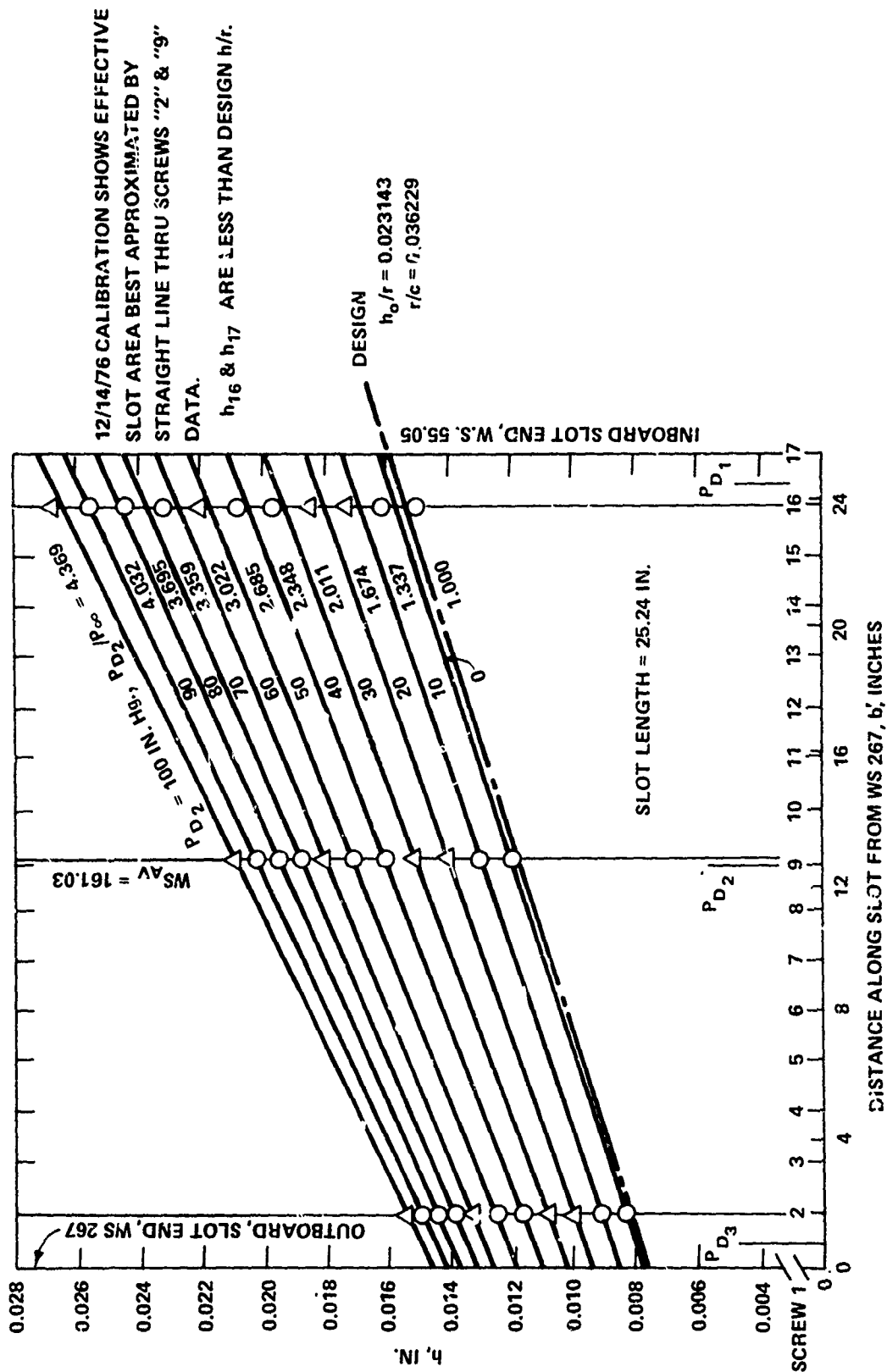


Figure 21 - A-6/CCW Phase II Left Wing
Slot Height Expansion

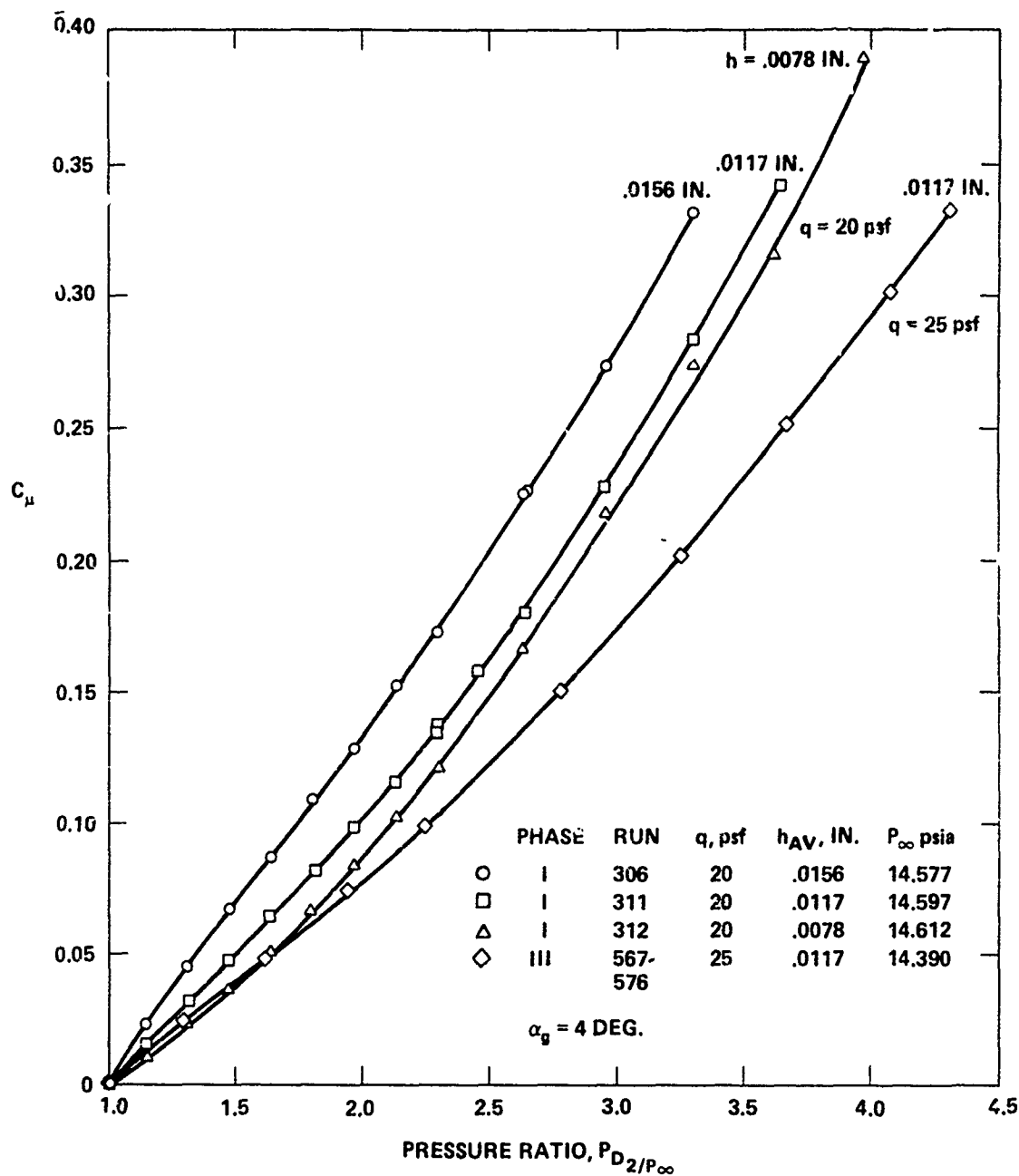


Figure 22 - Momentum Coefficient as a Function of Slot Height, Pressure Ratio, and Dynamic Pressure

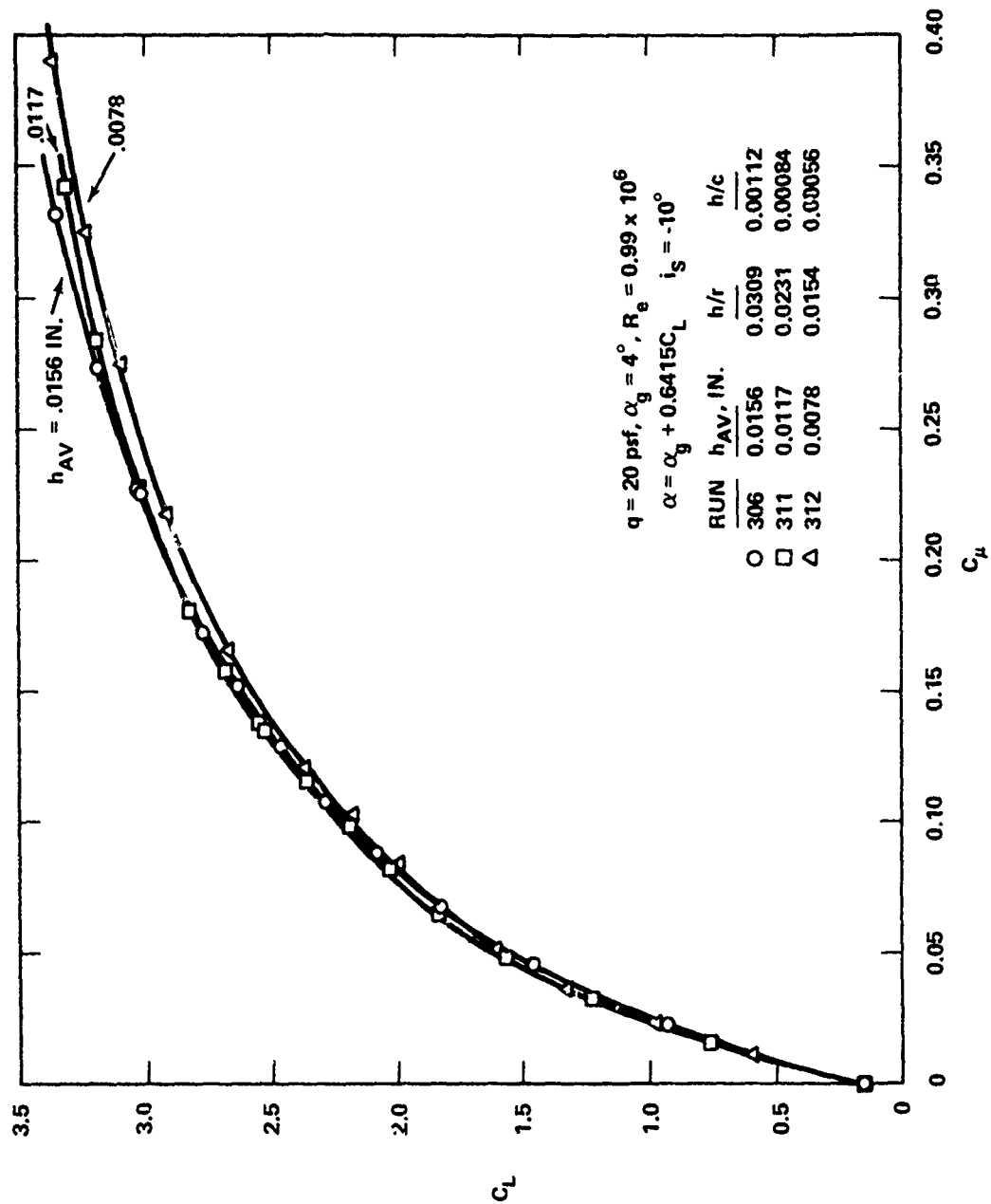


Figure 23 - Effect of Slot Height Variation on Lift Coefficient (Phase I)

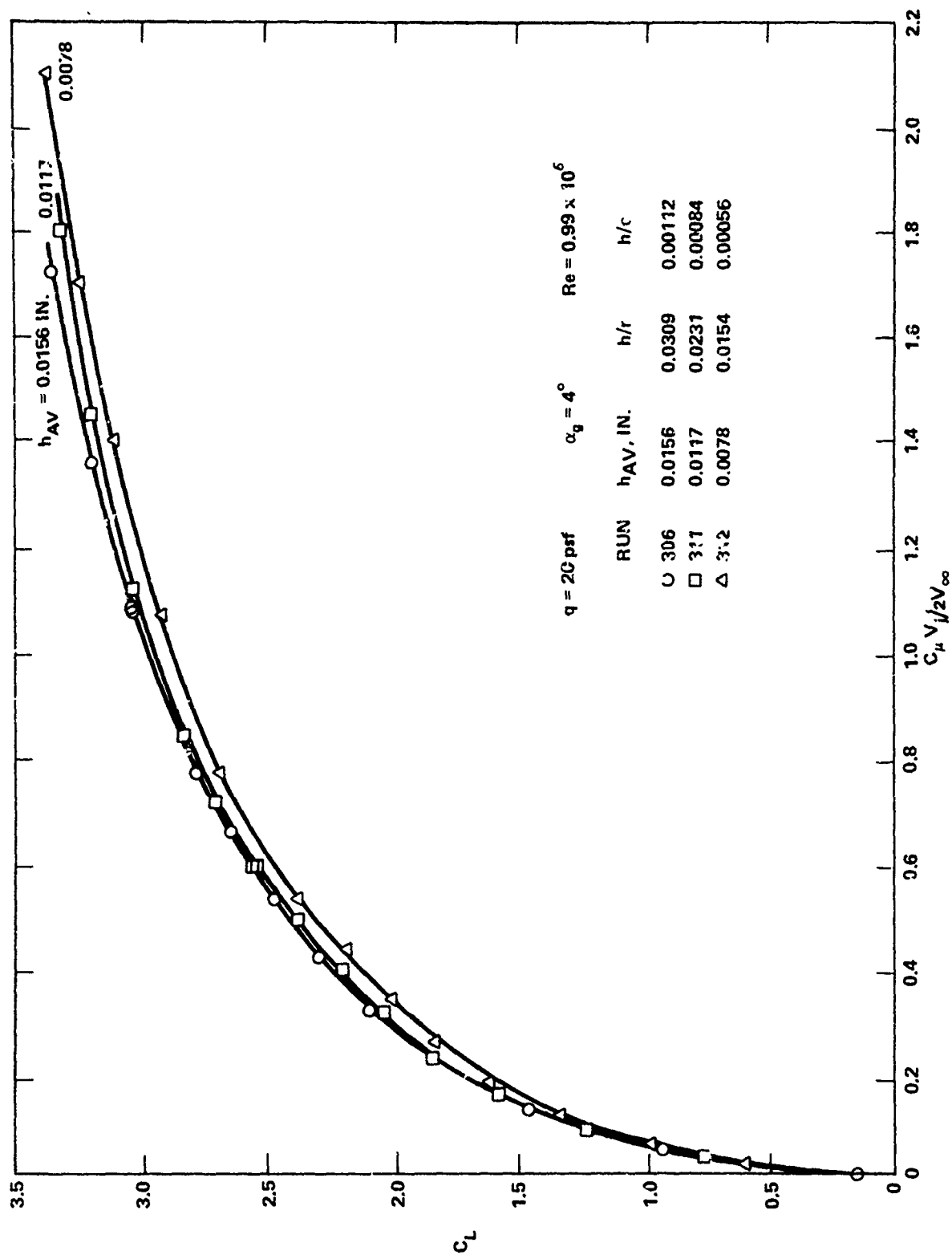


Figure 24 - Effect of Slot Height Variation as a Function of $C_\mu V_j/2V_\infty$ (Phase I)

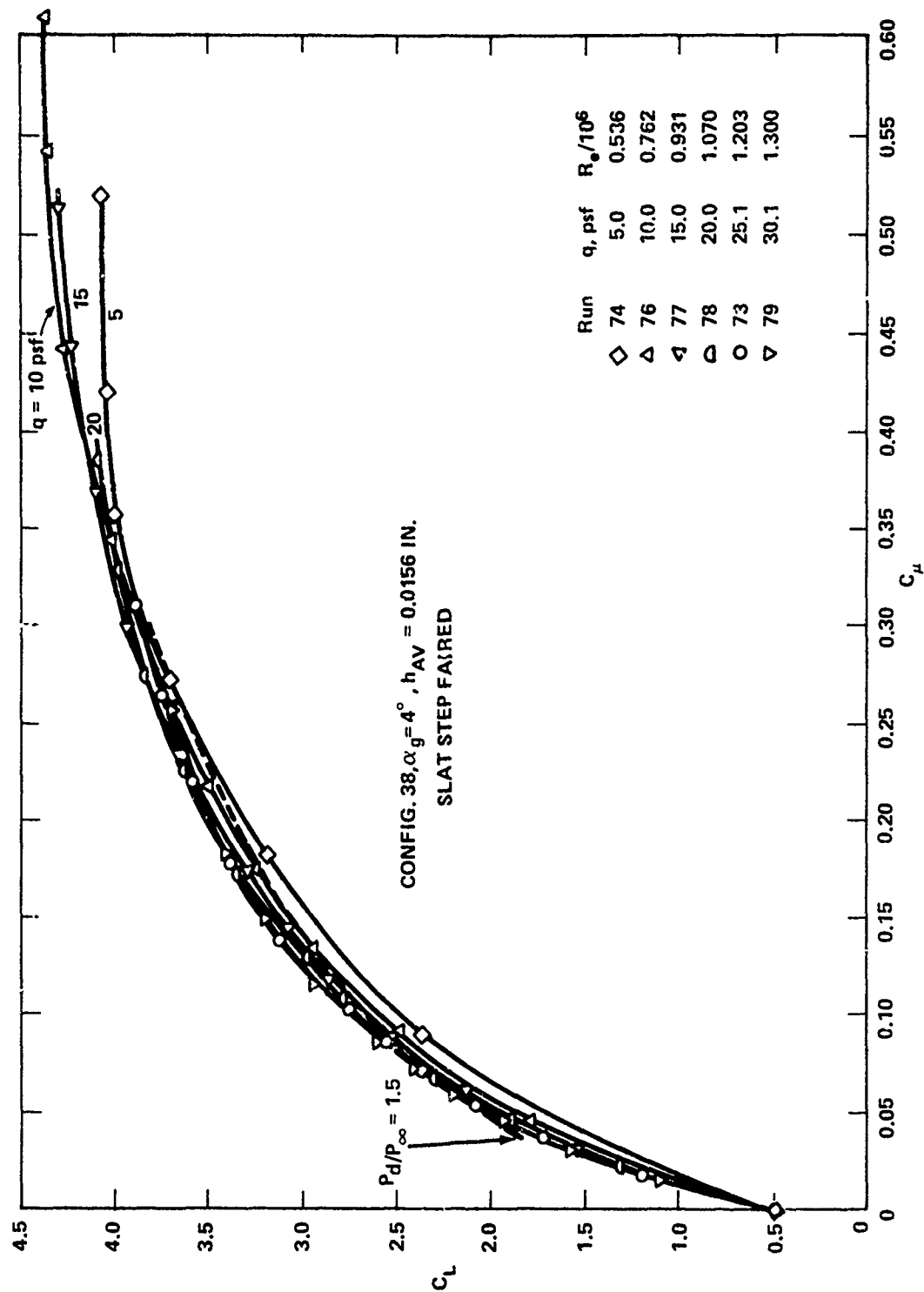


Figure 25 - Effect of Variation in Dynamic Pressure and C_μ (Phase I)

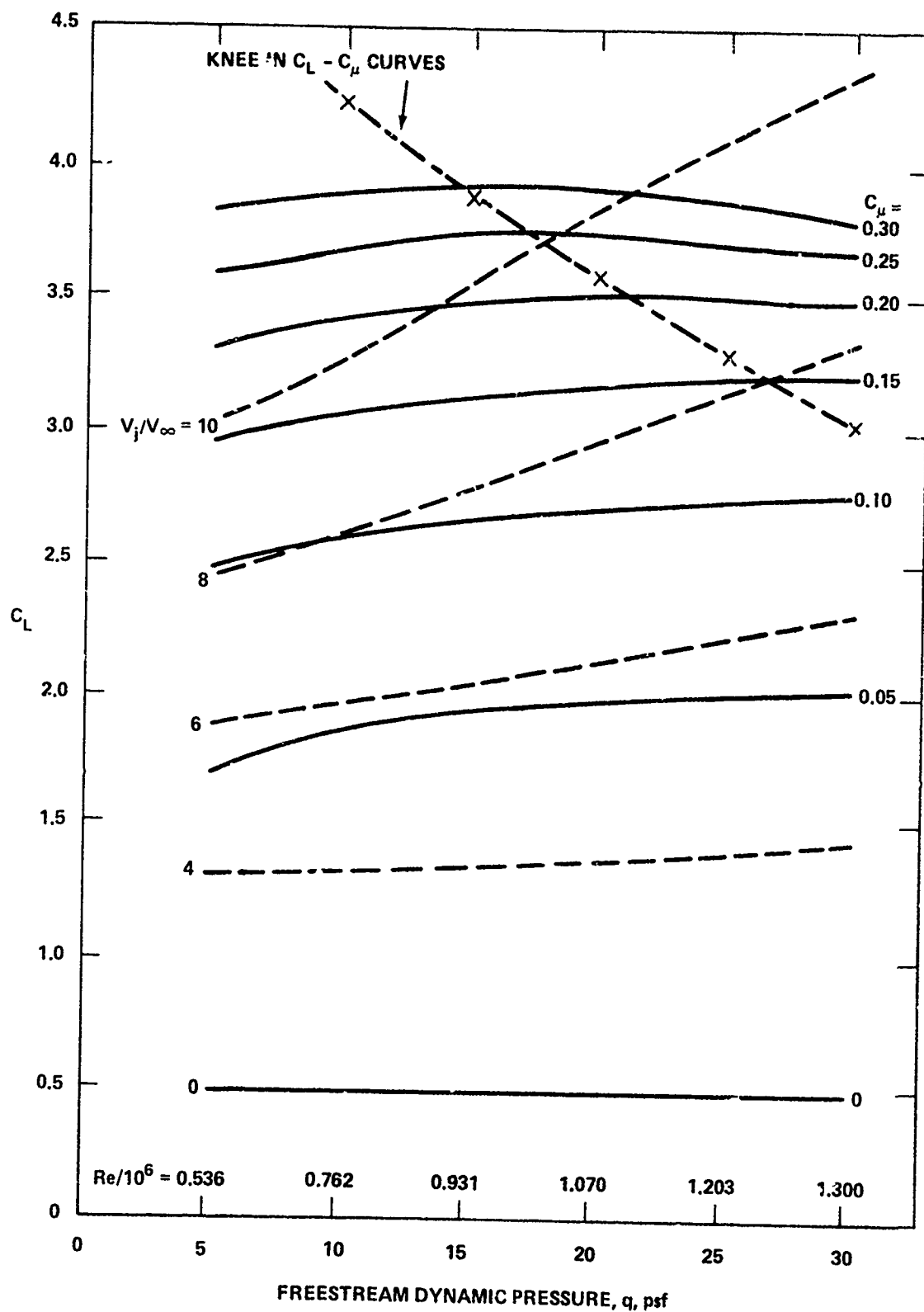


Figure 26 - Effect of Reynolds Number Variation at Constant Momentum Coefficient and Velocity Ratio

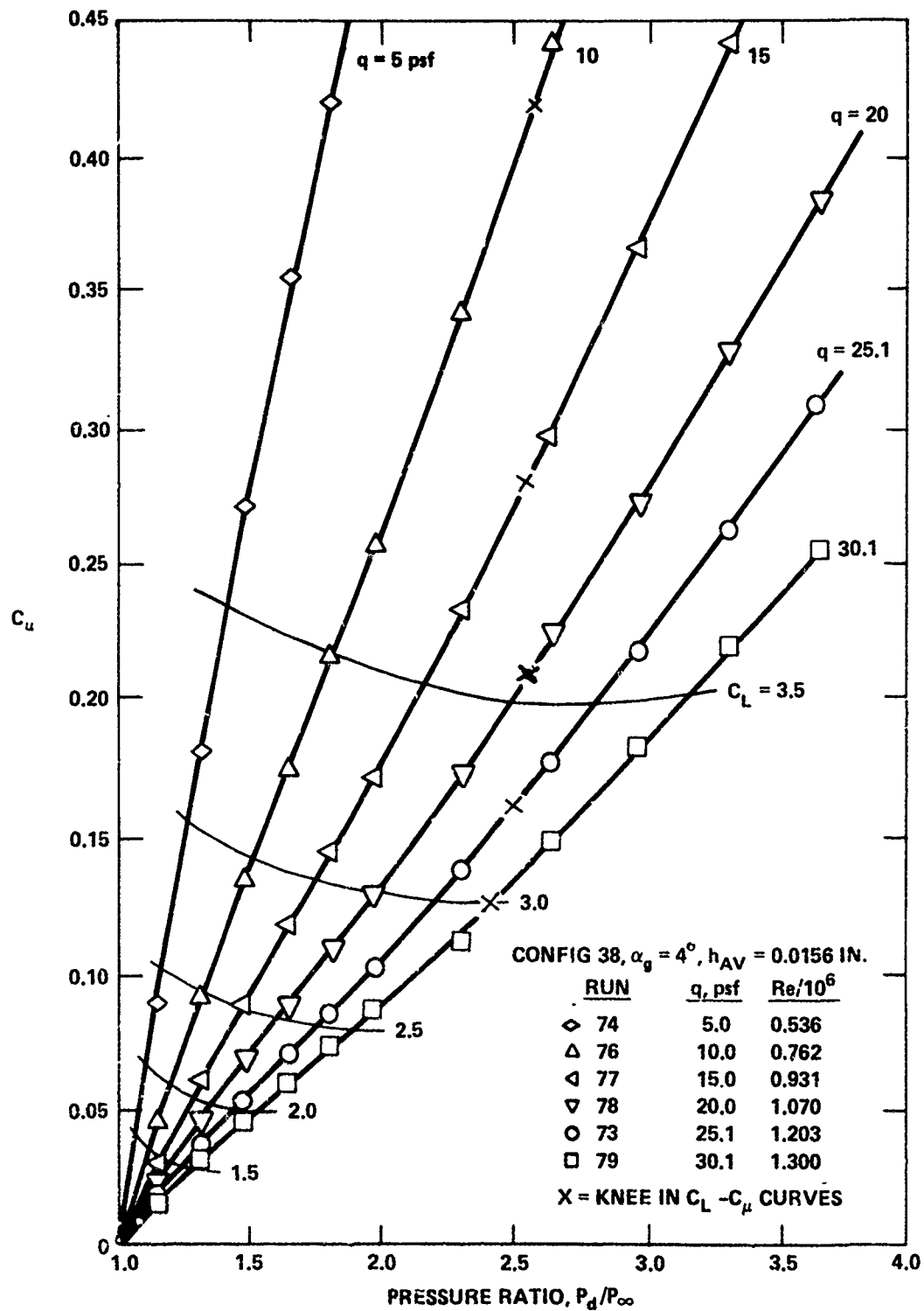


Figure 27 - Momentum Coefficient as a Function of Dynamic Pressure and Pressure Ratio (Phase I)

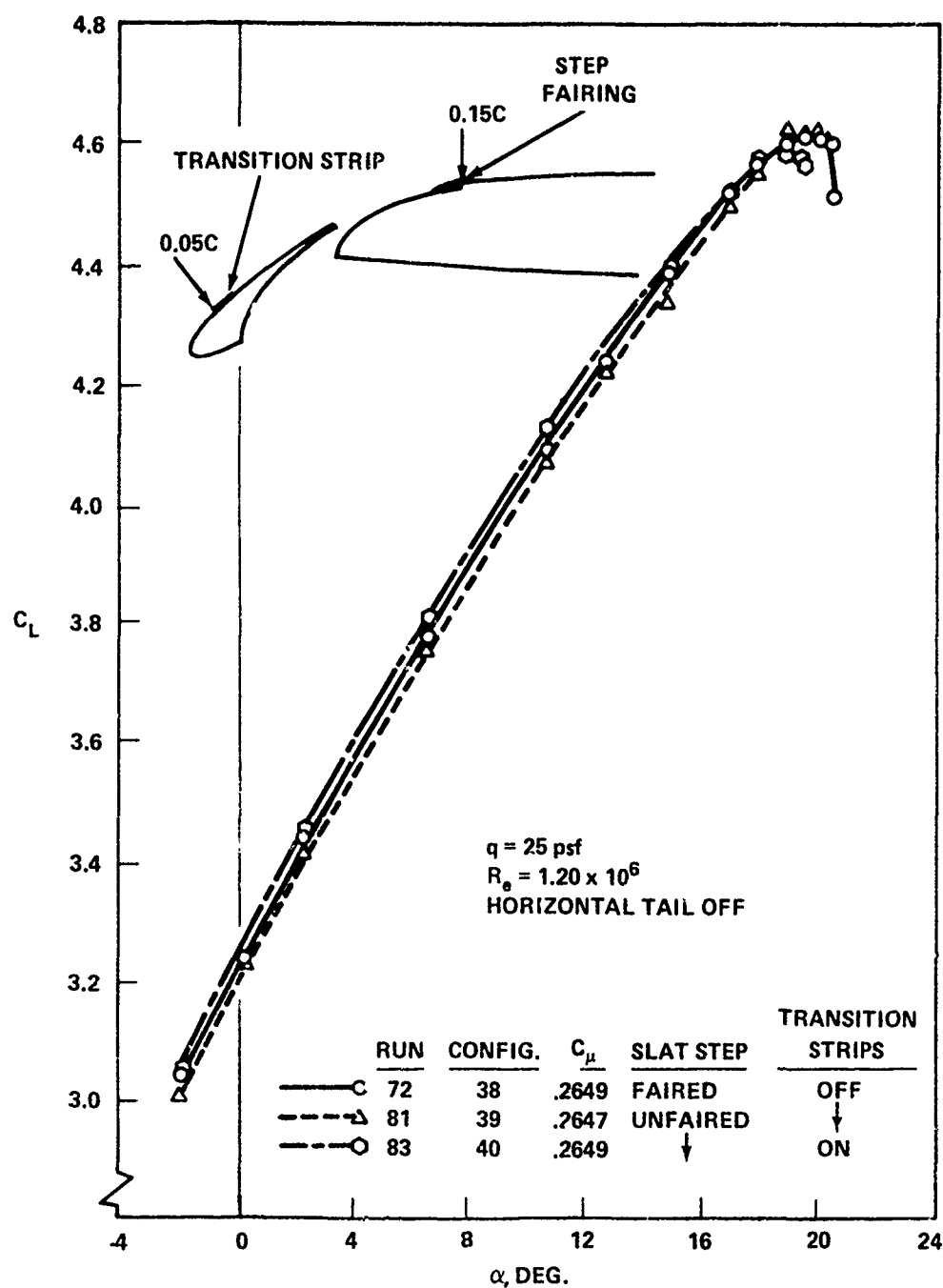


Figure 28 - Effect of Slat Step Fairing and Transition Strips

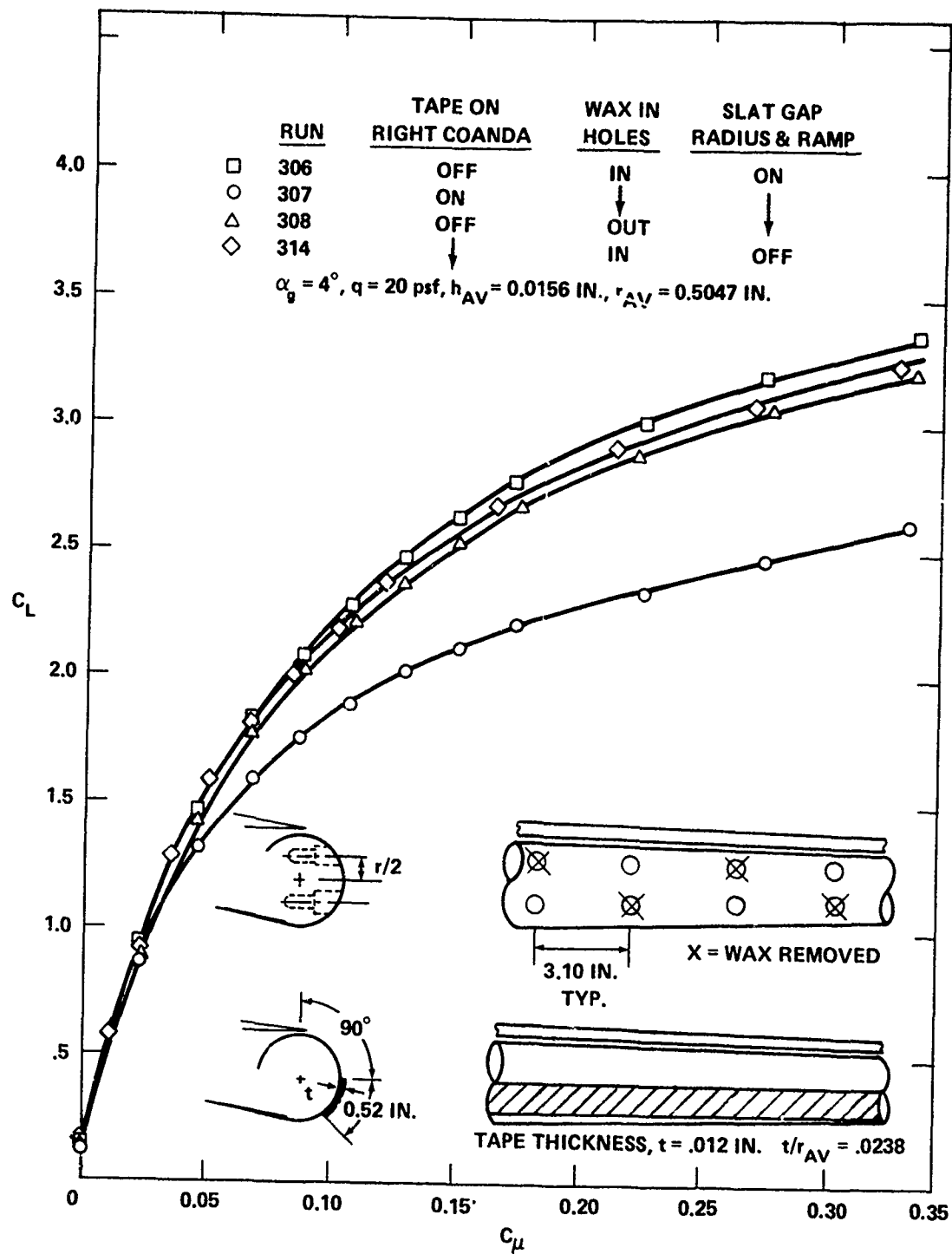
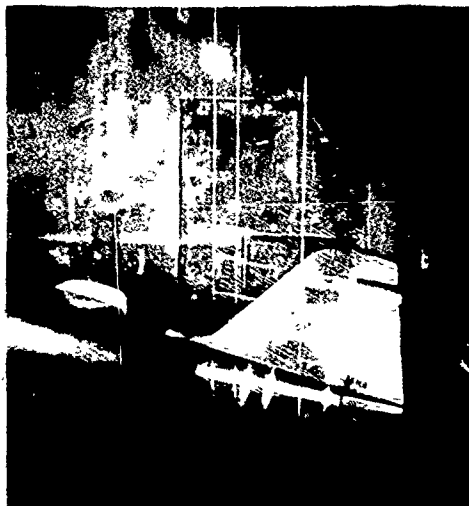
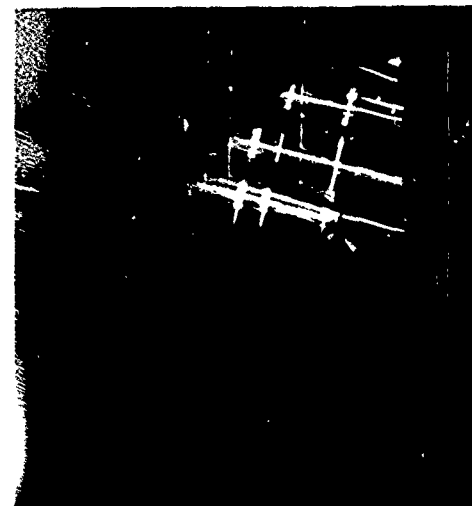


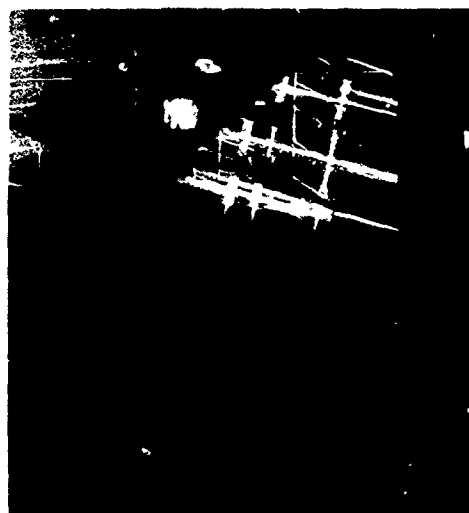
Figure 29 - Effect of Coanda Surface Imperfections (Phase I)



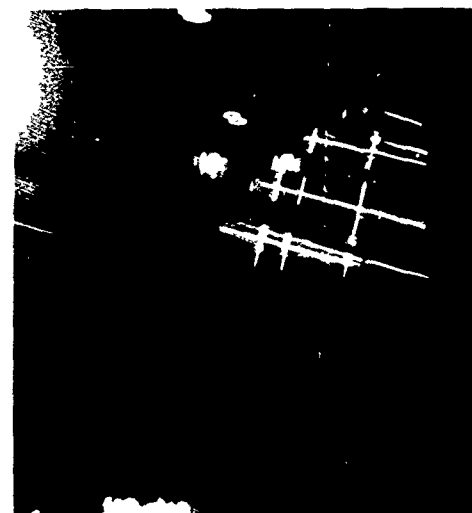
$C_{\mu} = 0, \alpha = 12.8^{\circ}, C_L = 1.18$



$C_{\mu} = 0.05, \alpha = 13.6^{\circ}, C_L = 2.53$



$C_{\mu} = 0.15, \alpha = 14.4^{\circ}, C_L = 3.74$



$C_{\mu} = 0.20, \alpha = 14.6^{\circ}, C_L = 4.07$

Figure 30 - Tufts Showing Downwash Angle in Vicinity of Horizontal Tail, $\alpha_g = 12$ deg, $q = 25$ psf

Figure 31 - Measured Downwash Angle at
Horizontal Tail Quarter Chords
(Phase I)

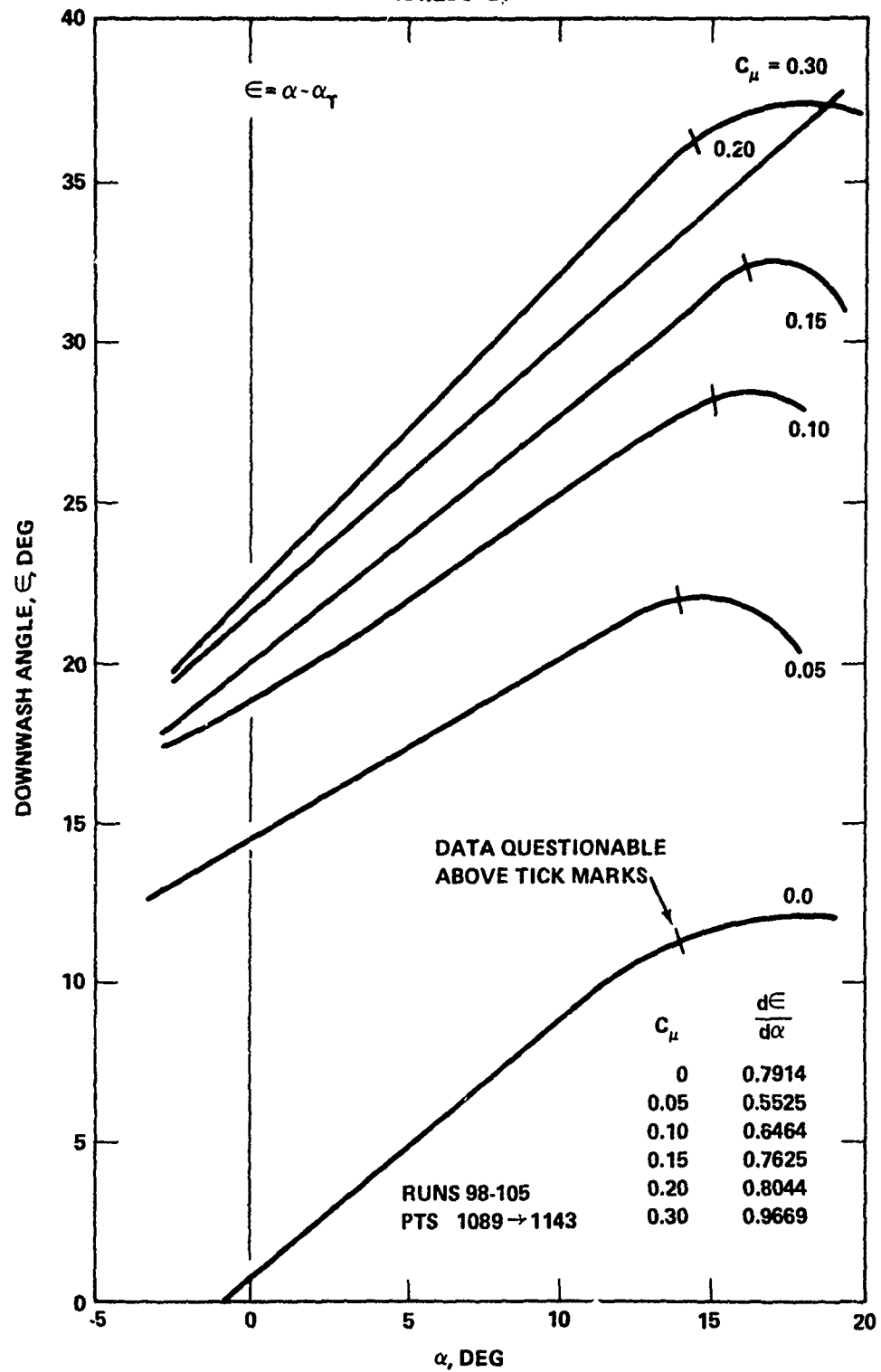


Figure 31a - Tail Tip, $y/0.5 b_T = 1.00$

Figure 31 (Continued)

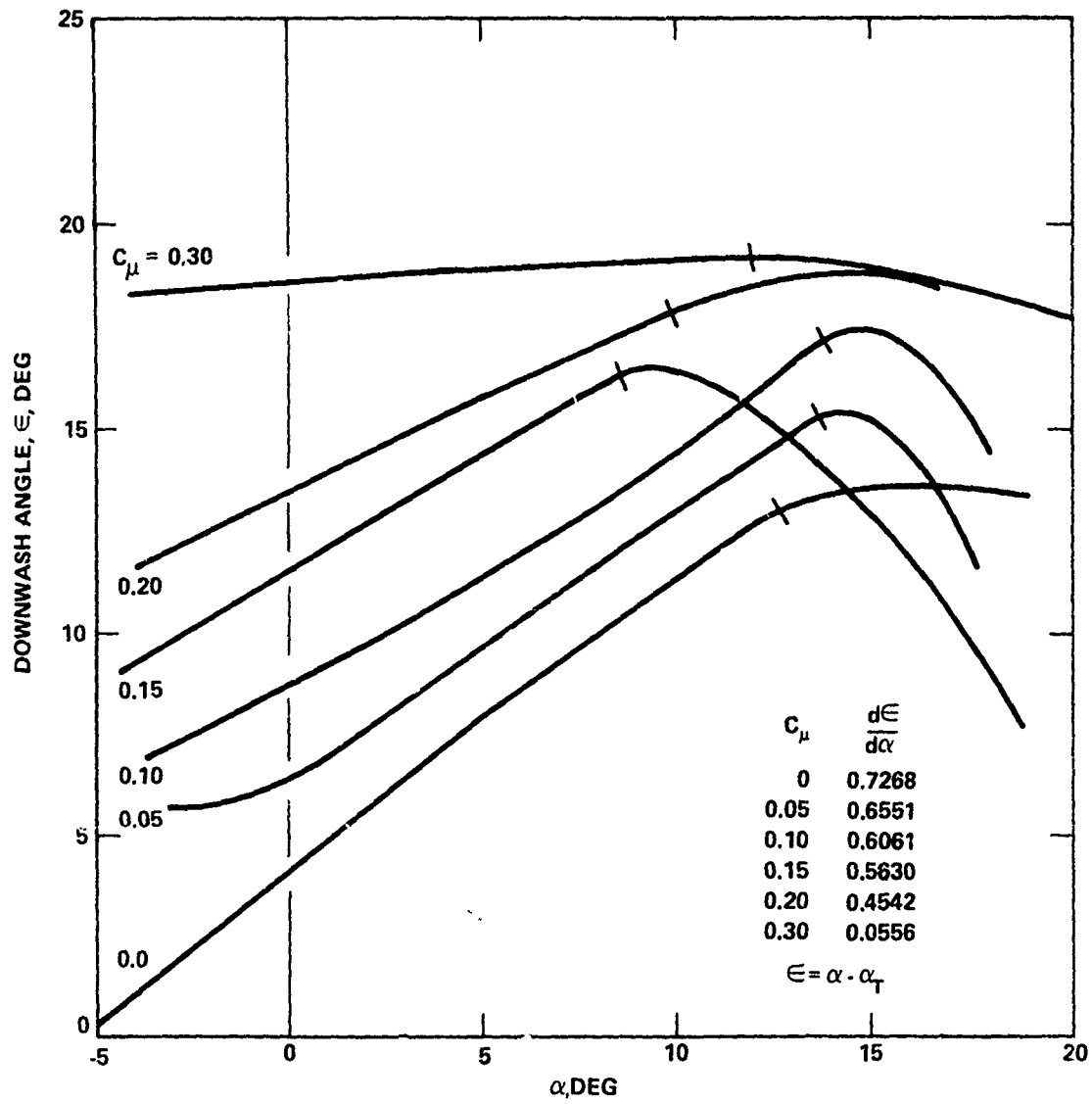


Figure 31b - Tail MAC, $y/0.15 b_T = 0.429$

Figure 31 (Continued)

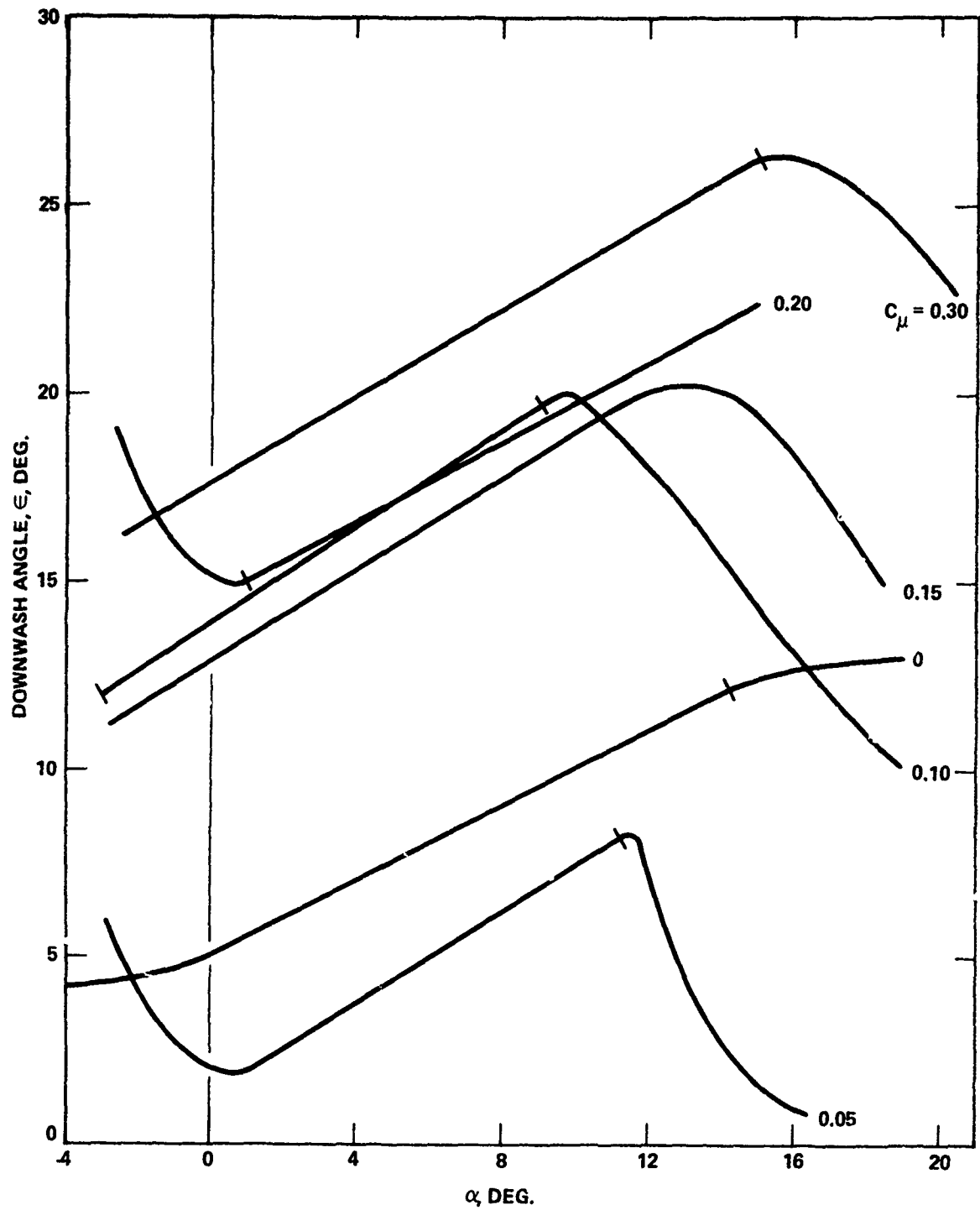


Figure 31c - $y/0.5 b_T = 0.200$

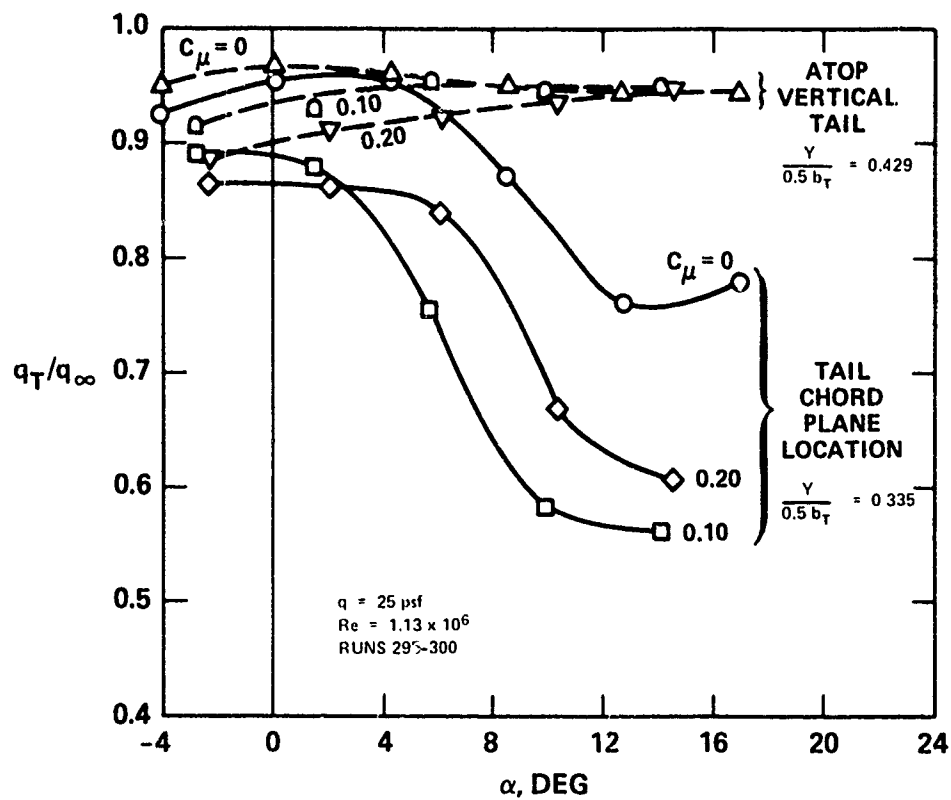
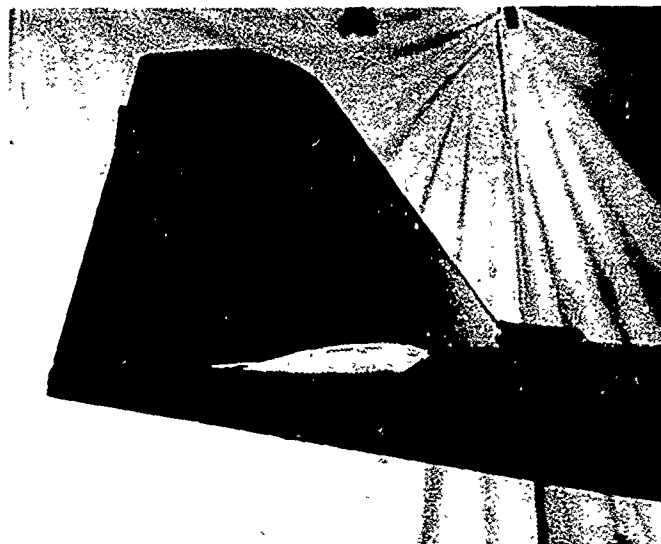
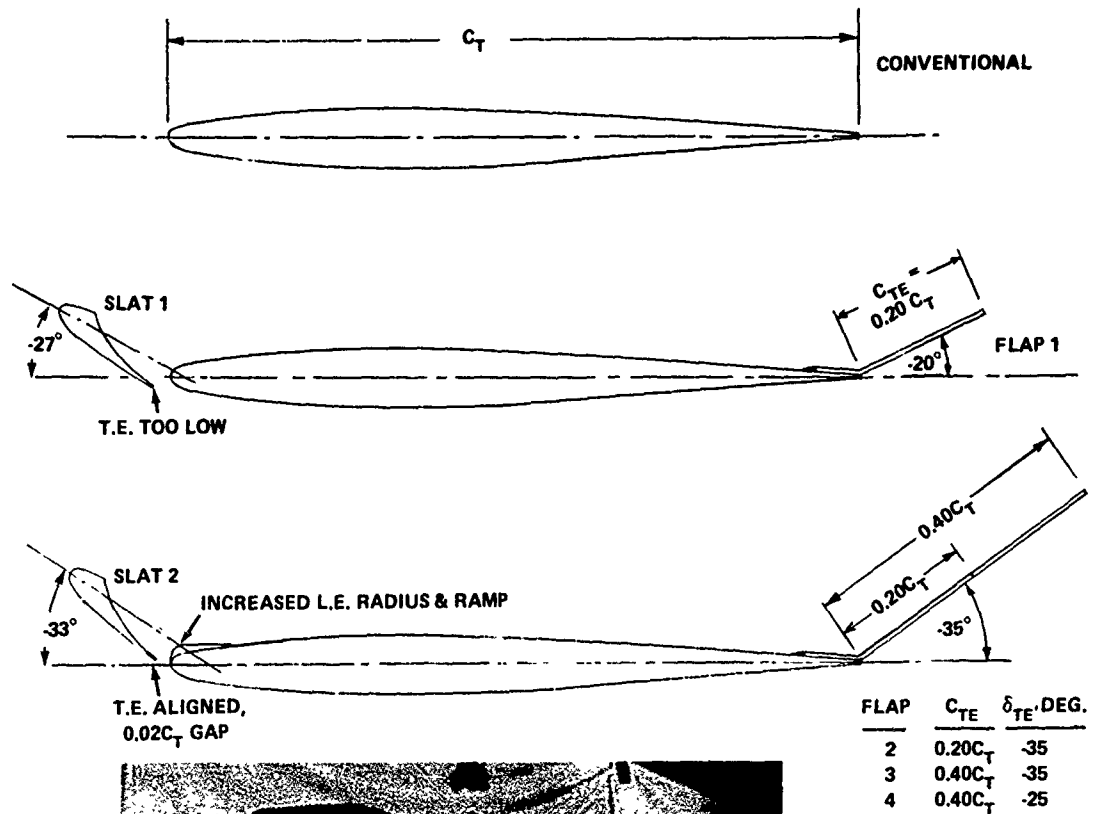


Figure 32 - Tail Dynamic Pressure Measurement (Phase I)

Figure 33 - Horizontal Tail Configurations
(Phase I)



FINAL PHASE I HORIZONTAL
STABILIZER (SLAT 2, FLAP 4,
TIP FAIRING & DROOP)

Figure 33a - Airfoil Sections

Figure 33 (Continued)

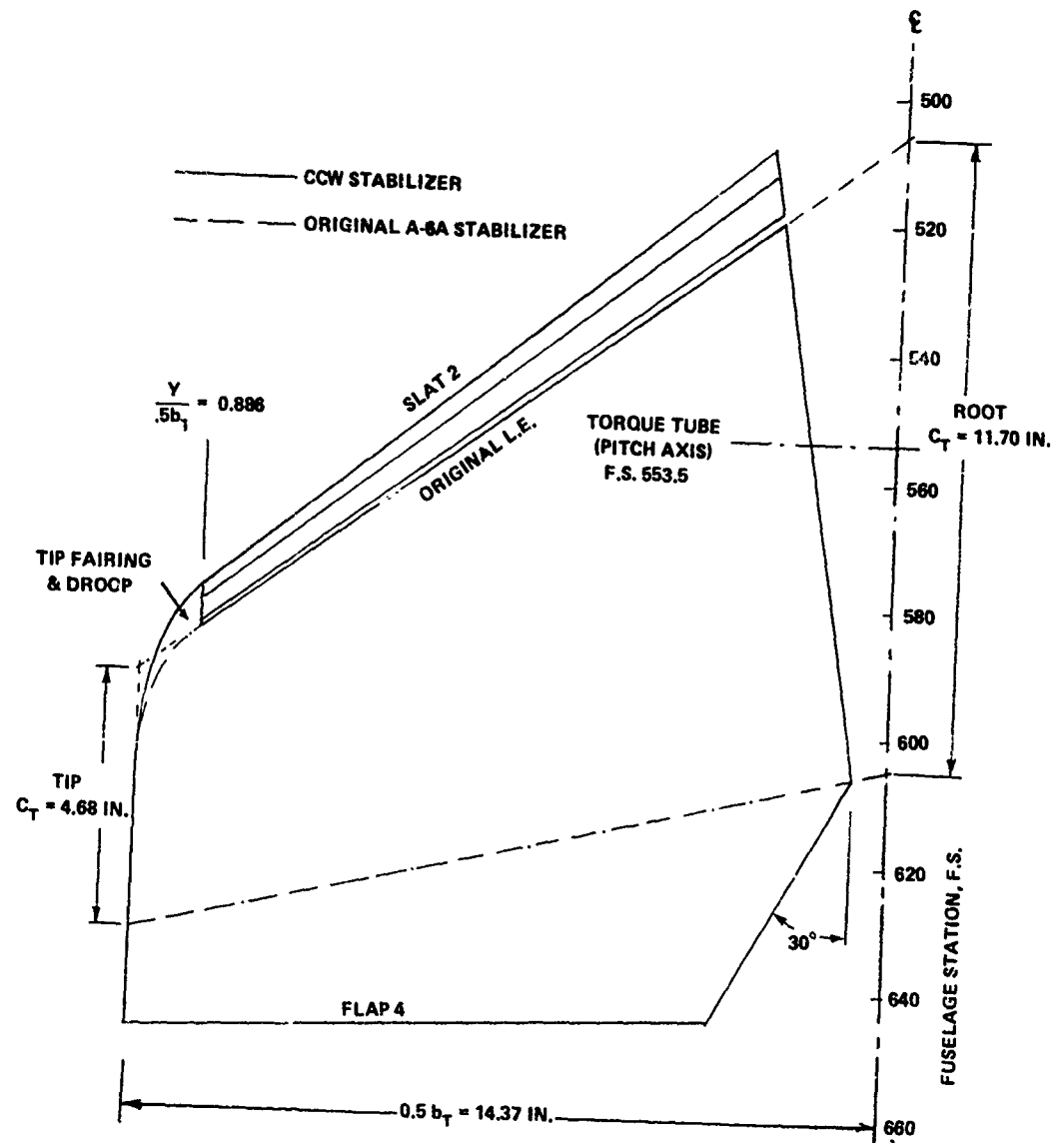


Figure 33b - Planform

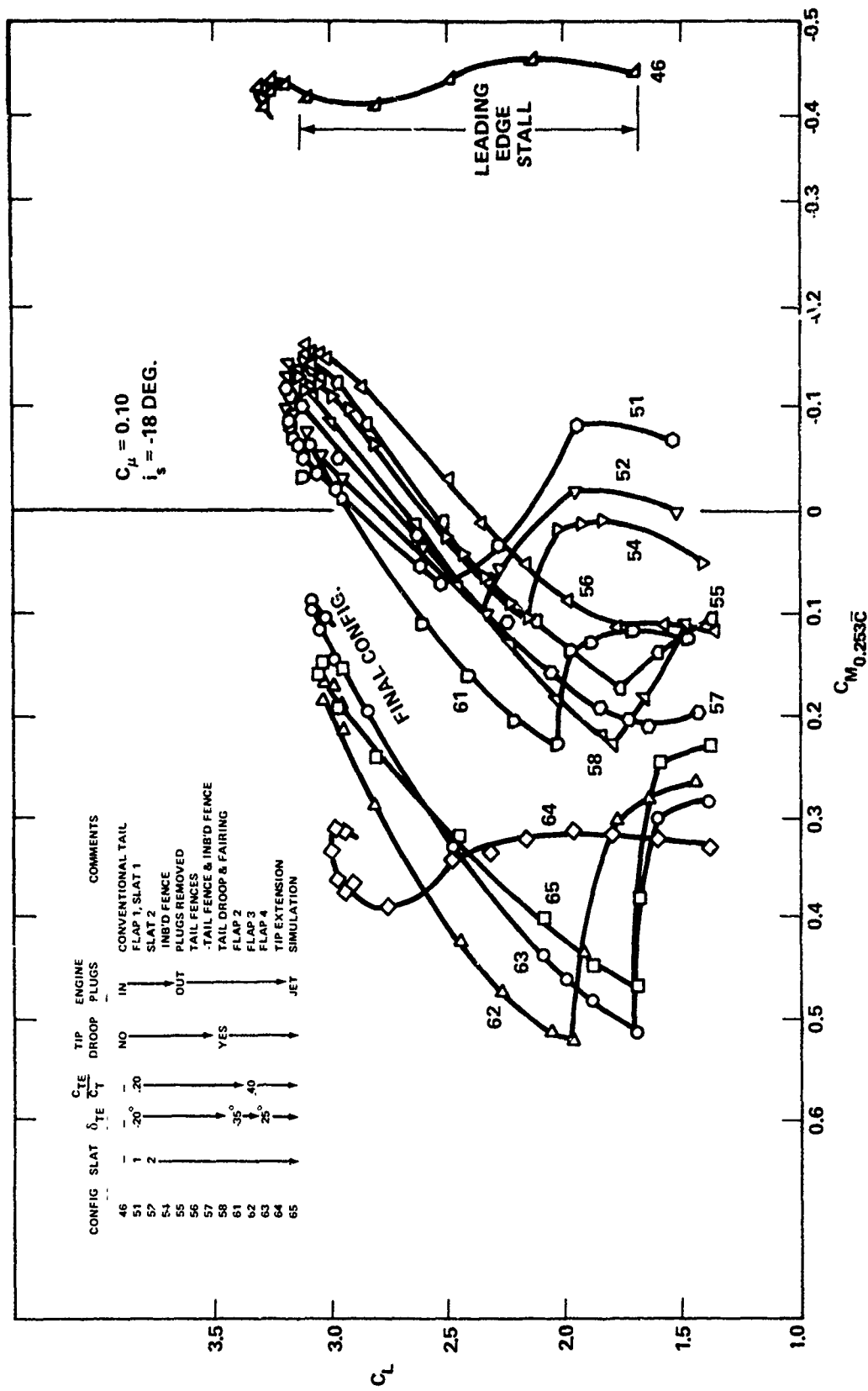


Figure 34 - Effect of Various Tail Configurations on Pitching Moment (Phase I, $C_{\mu} = 0.10$)

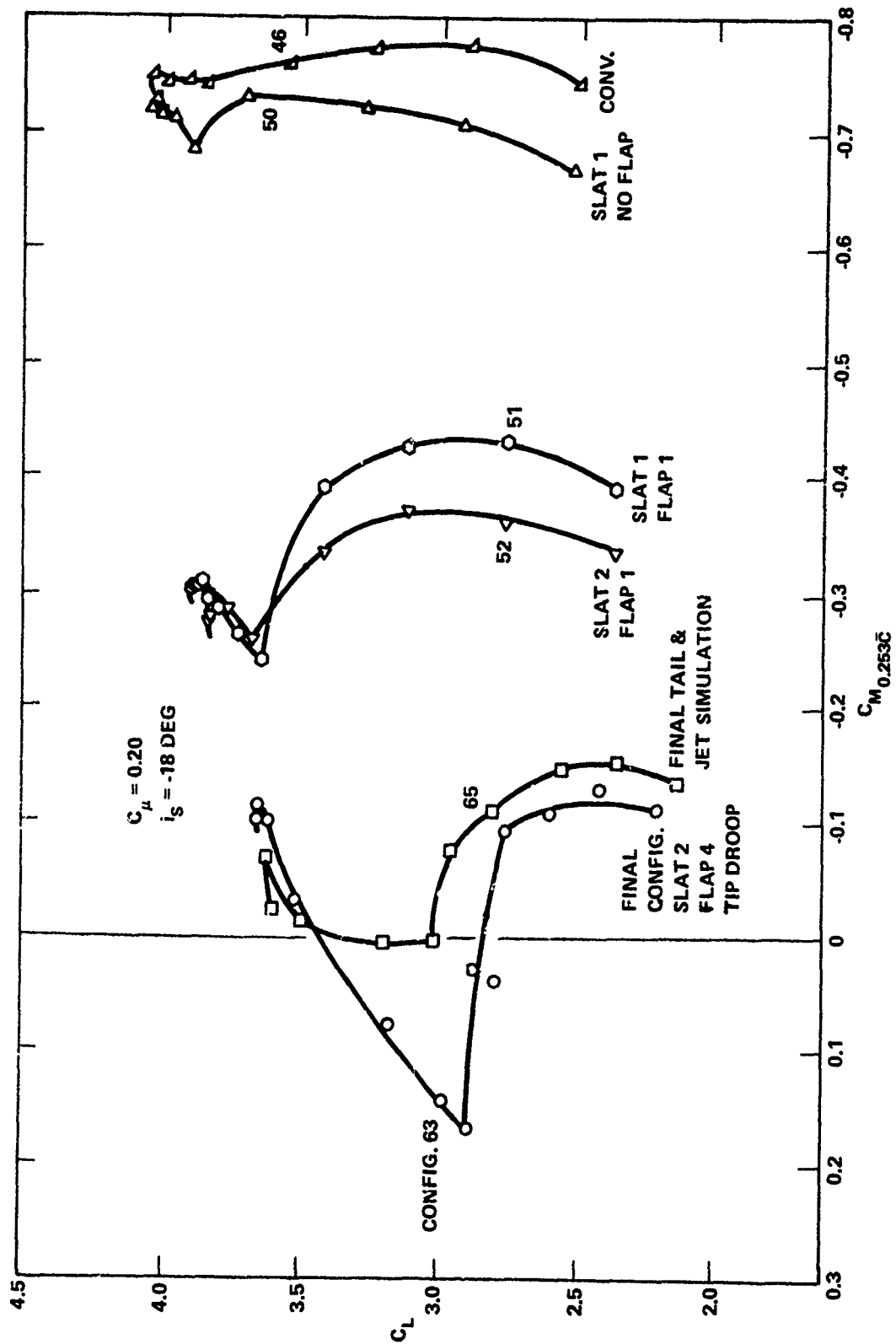


Figure 35 - Effect of Various Tail Configurations on Pitching Moment (Phase I, $C_\mu = 0.20$)

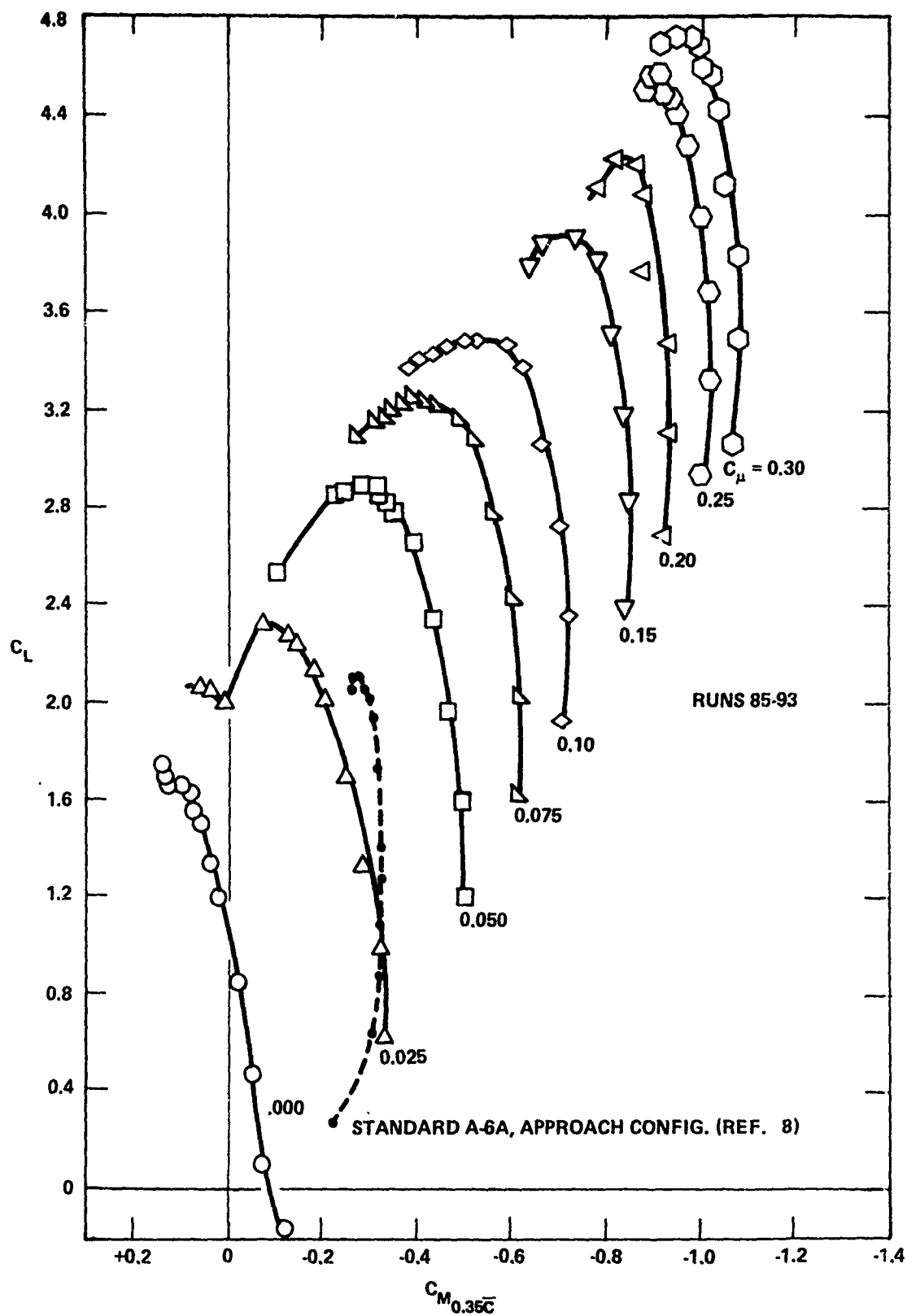


Figure 36 - Tail-Off Pitching Moment for the A-6/CCW Phase I Configuration of Figure 12, but with $X_{cg} = 0.35\pi$

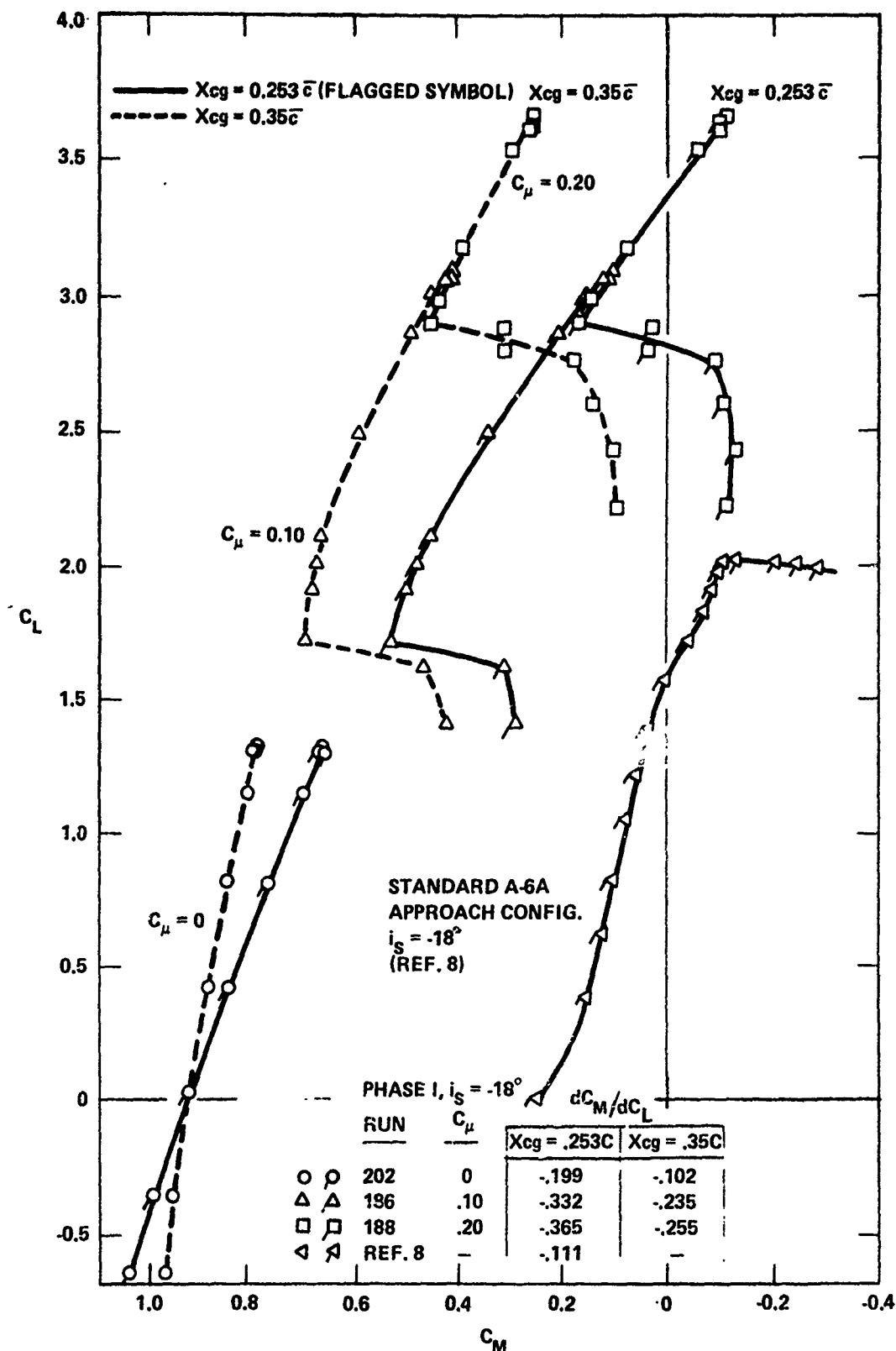


Figure 37 - Effect of Aft Center-of-Gravity Shift (Configuration 63, Phase I)

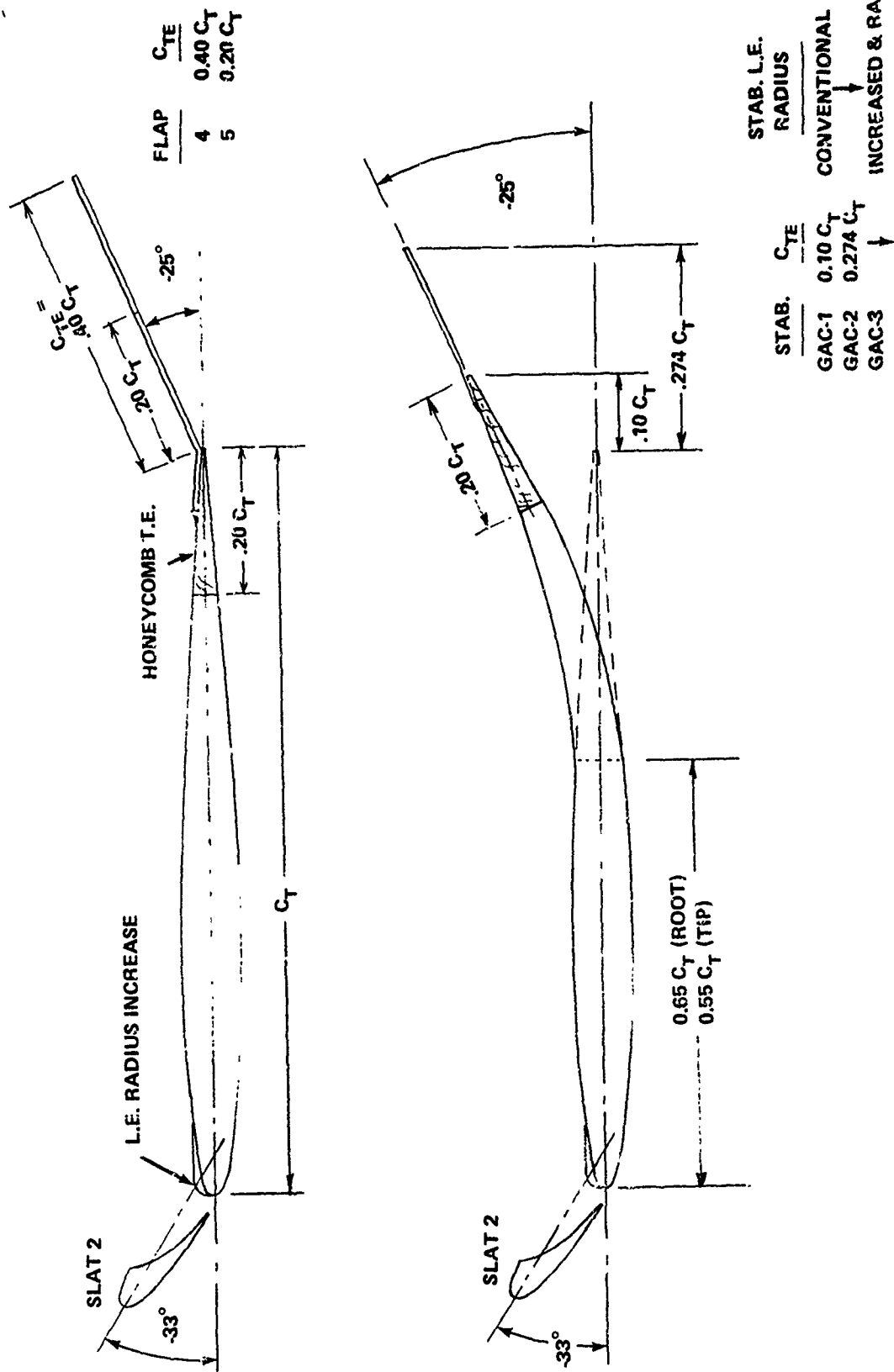


Figure 38 - Horizontal Stabilizer Configuration (Phase II)

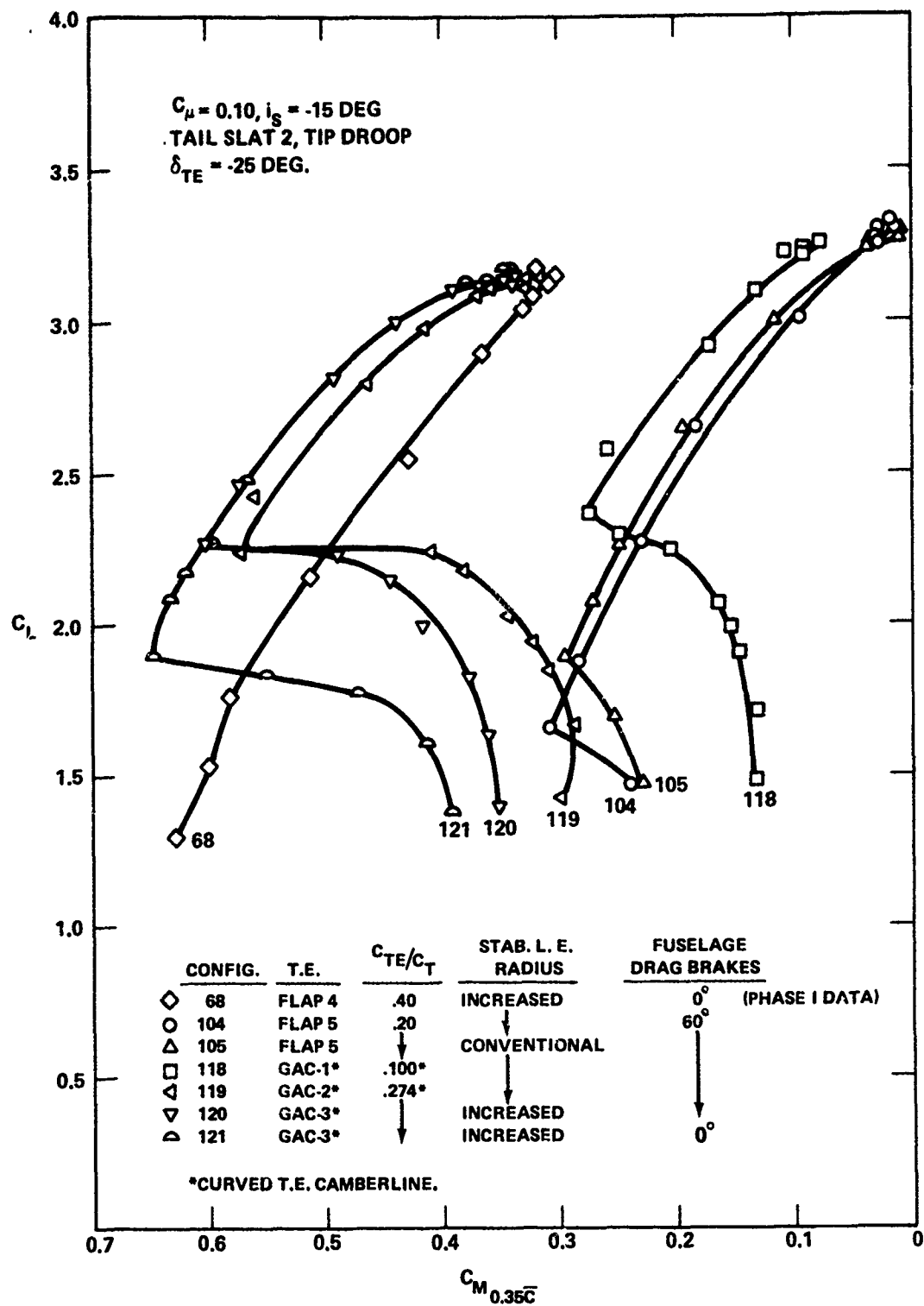


Figure 39 - Horizontal Tail Development,
 $C_{\mu} = 0.10$ (Phase II)

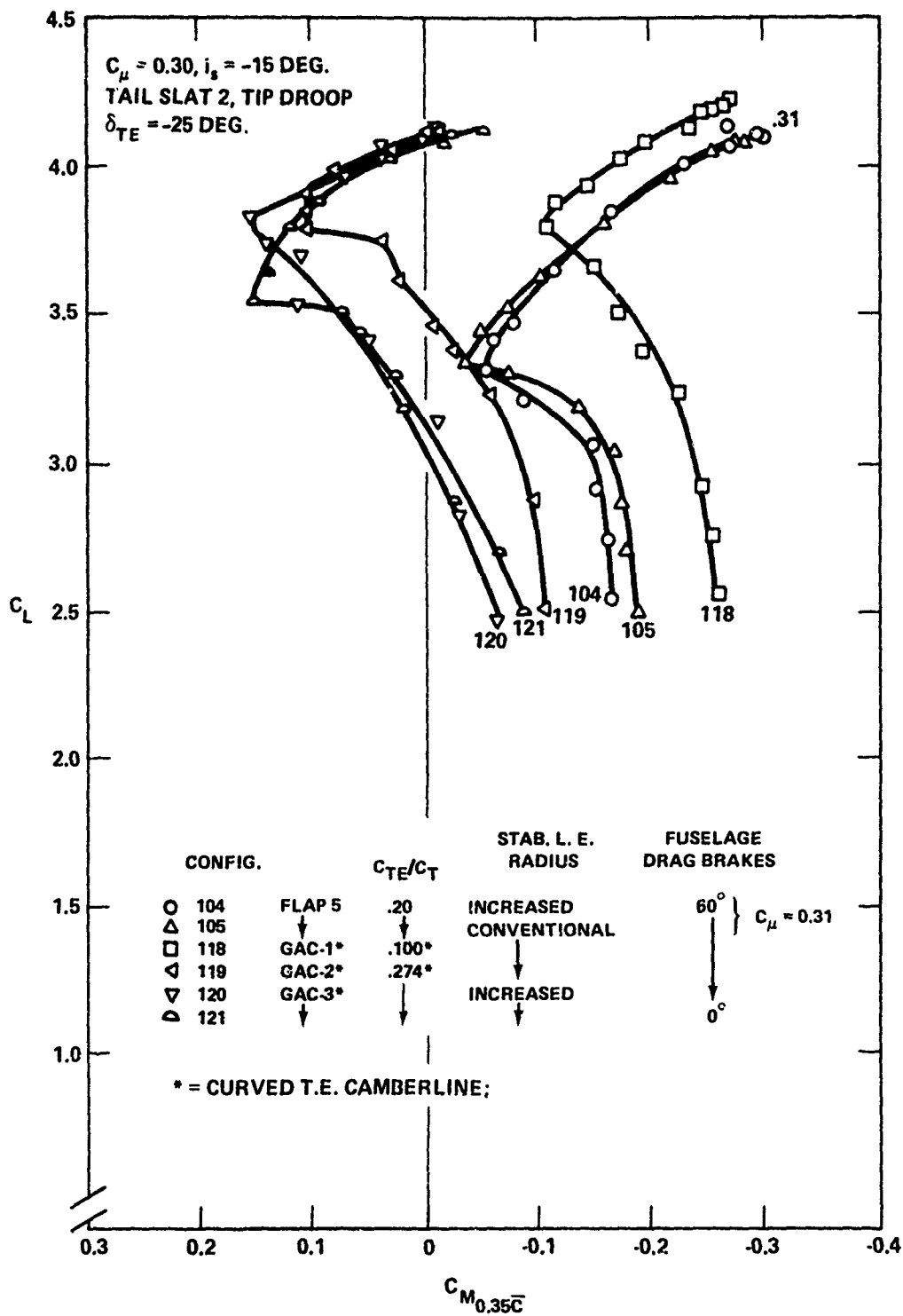


Figure 40 - Horizontal Tail Development,
 $C_{\mu} = 0.30$ (Phase II)

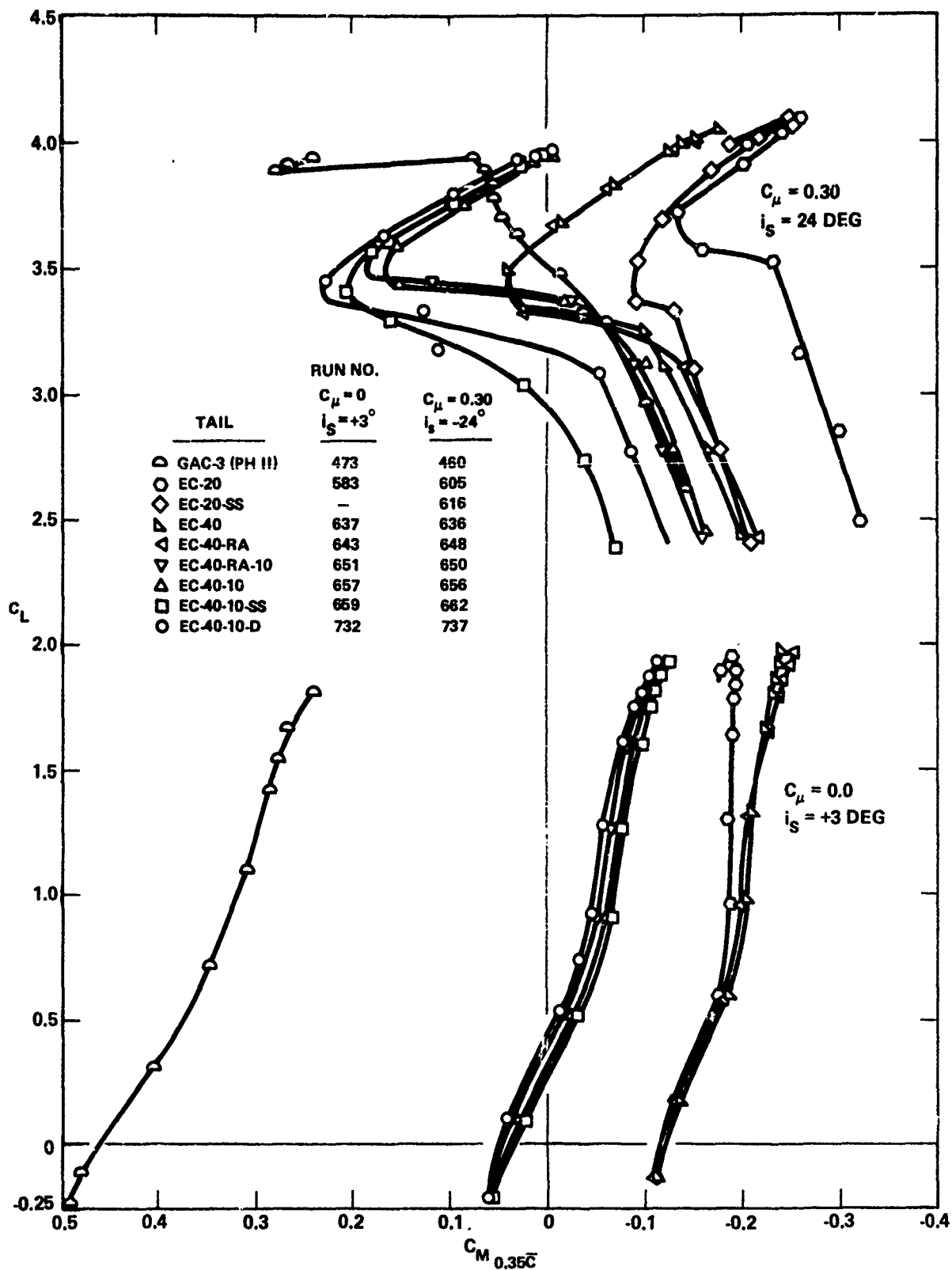


Figure 41 - Horizontal Tail Development
(Phase III)

Figure 42 - Horizontal Stabilizer Configurations
(Phase III)

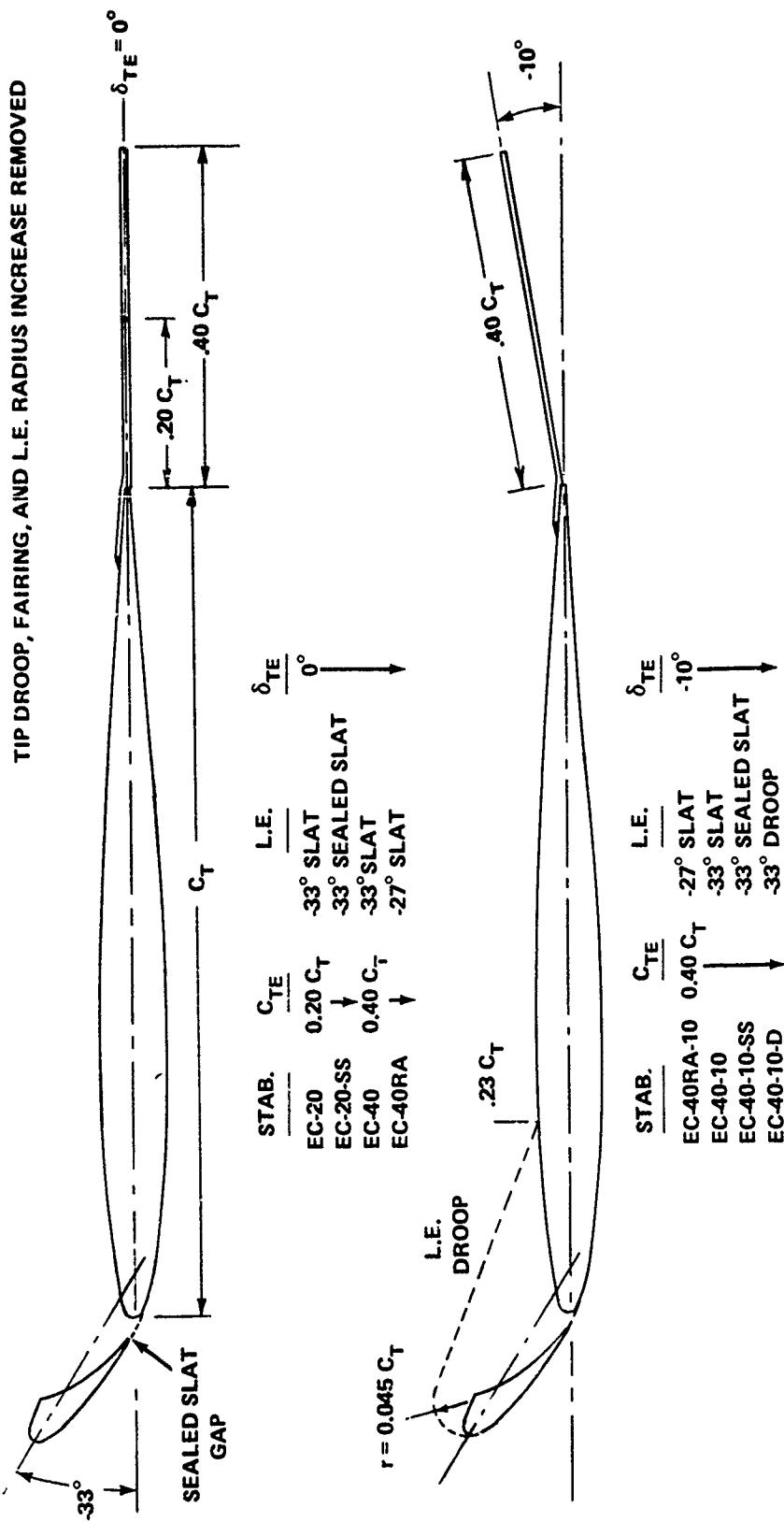


Figure 42a - Airfoil Sections

Figure 42 (Continued)

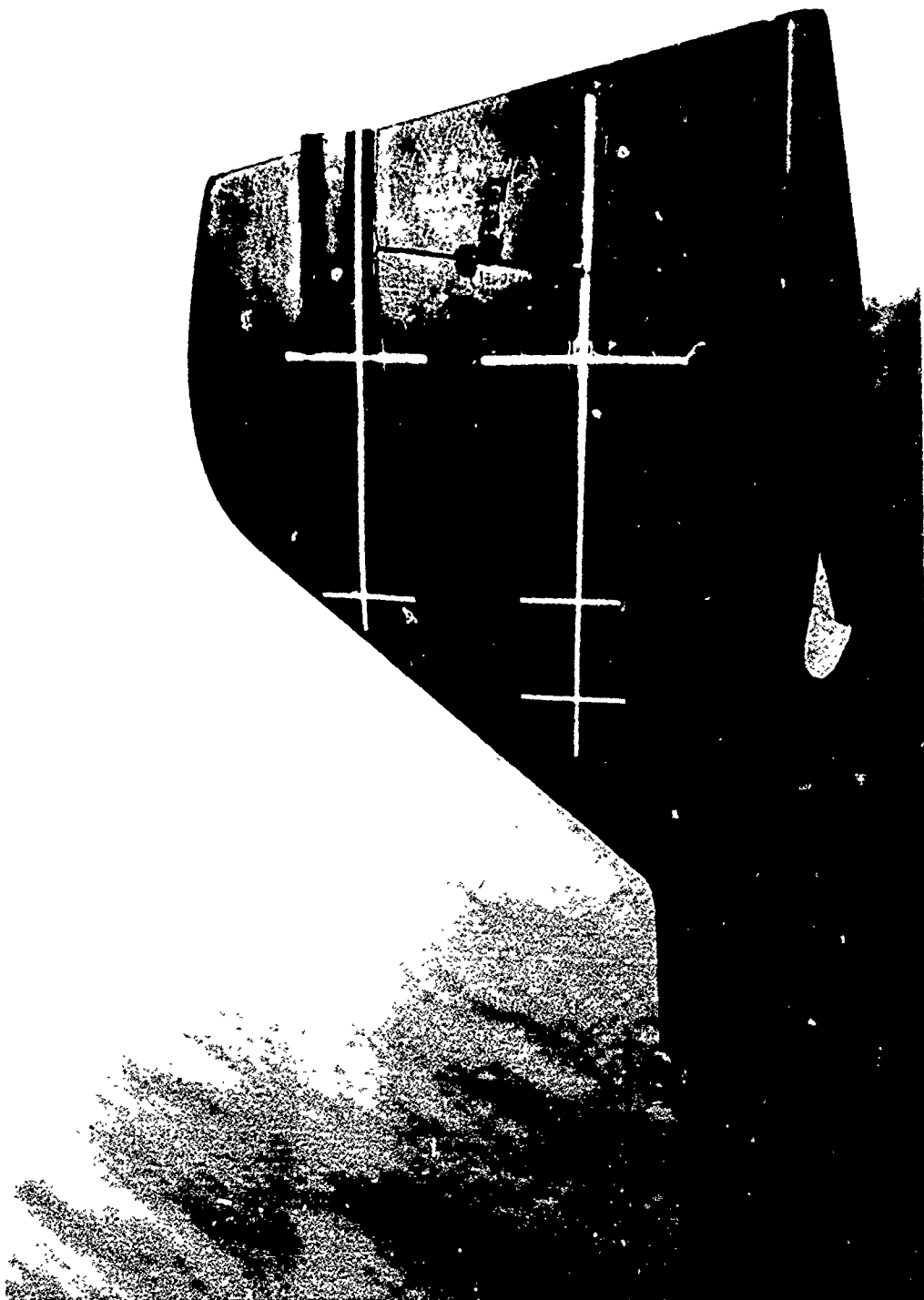


Figure 42b - Final Phase III Tail Configuration,
EC-40-10-D

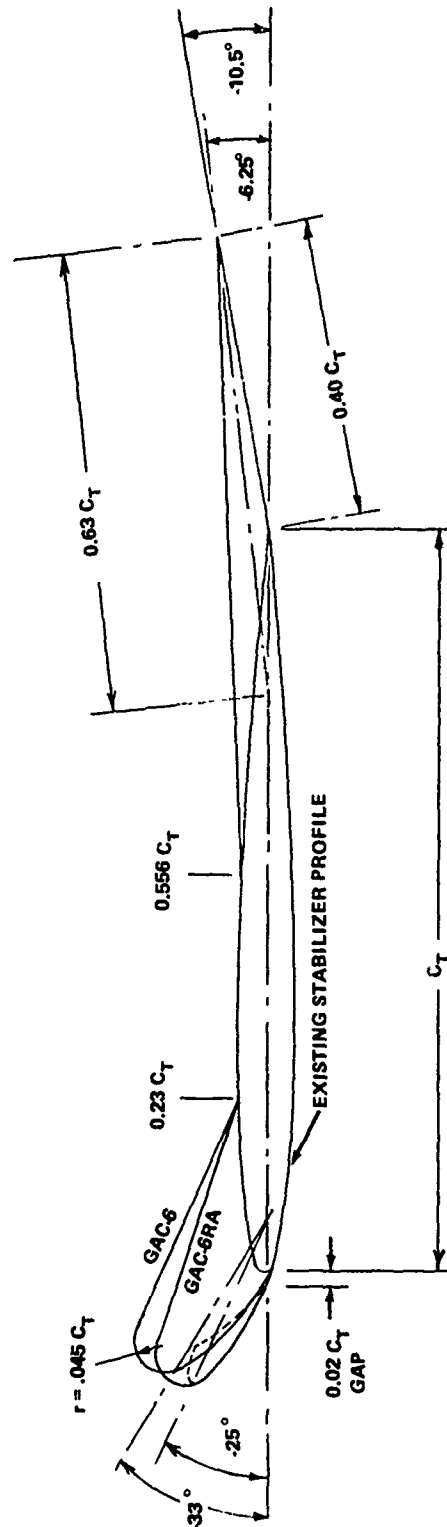


Figure 43 - Horizontal Stabilizer Configurations
(Phase IV)

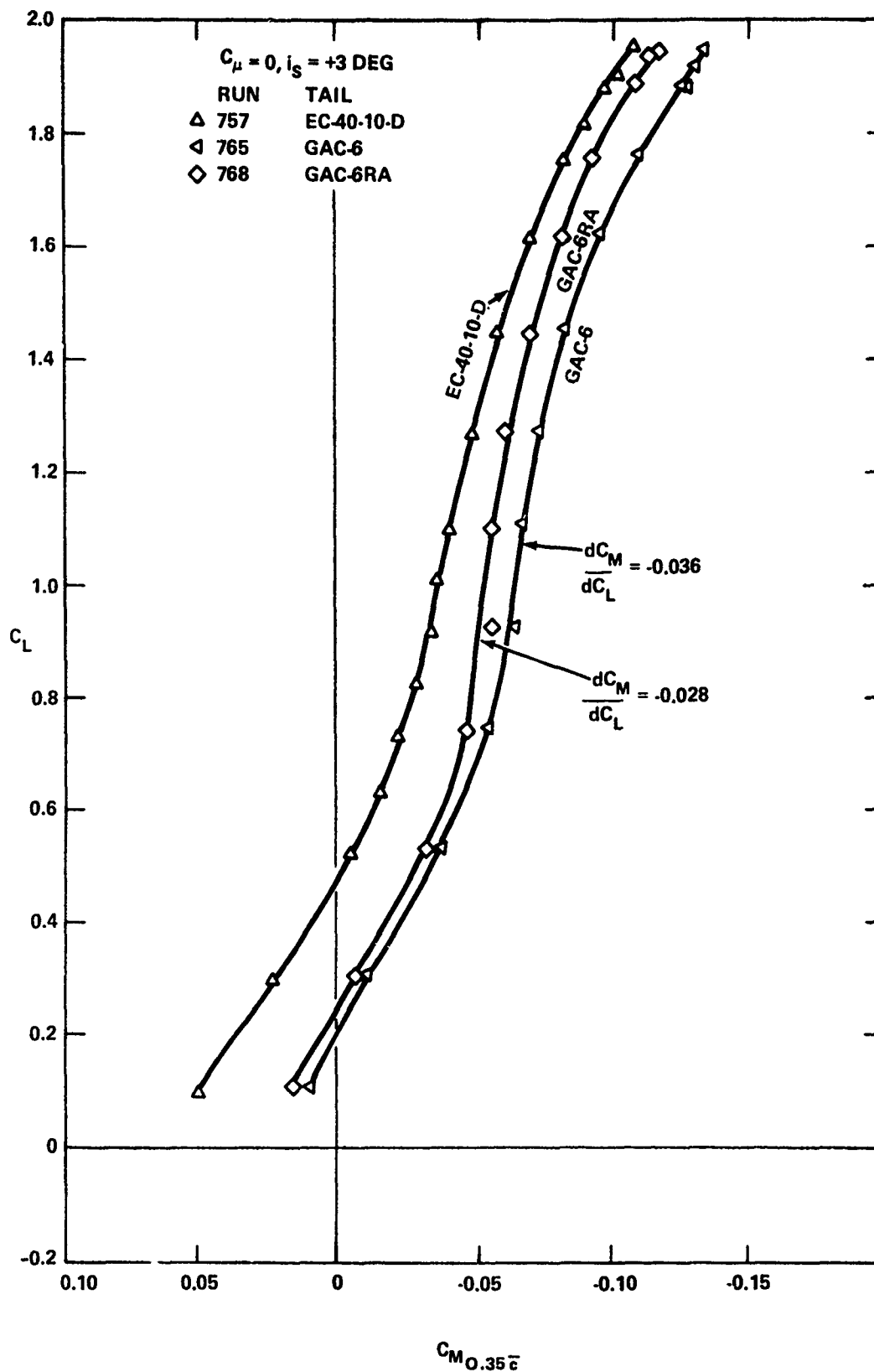


Figure 44 - Horizontal Tail Development,
 $C_{\mu} = 0$ (Phase IV)

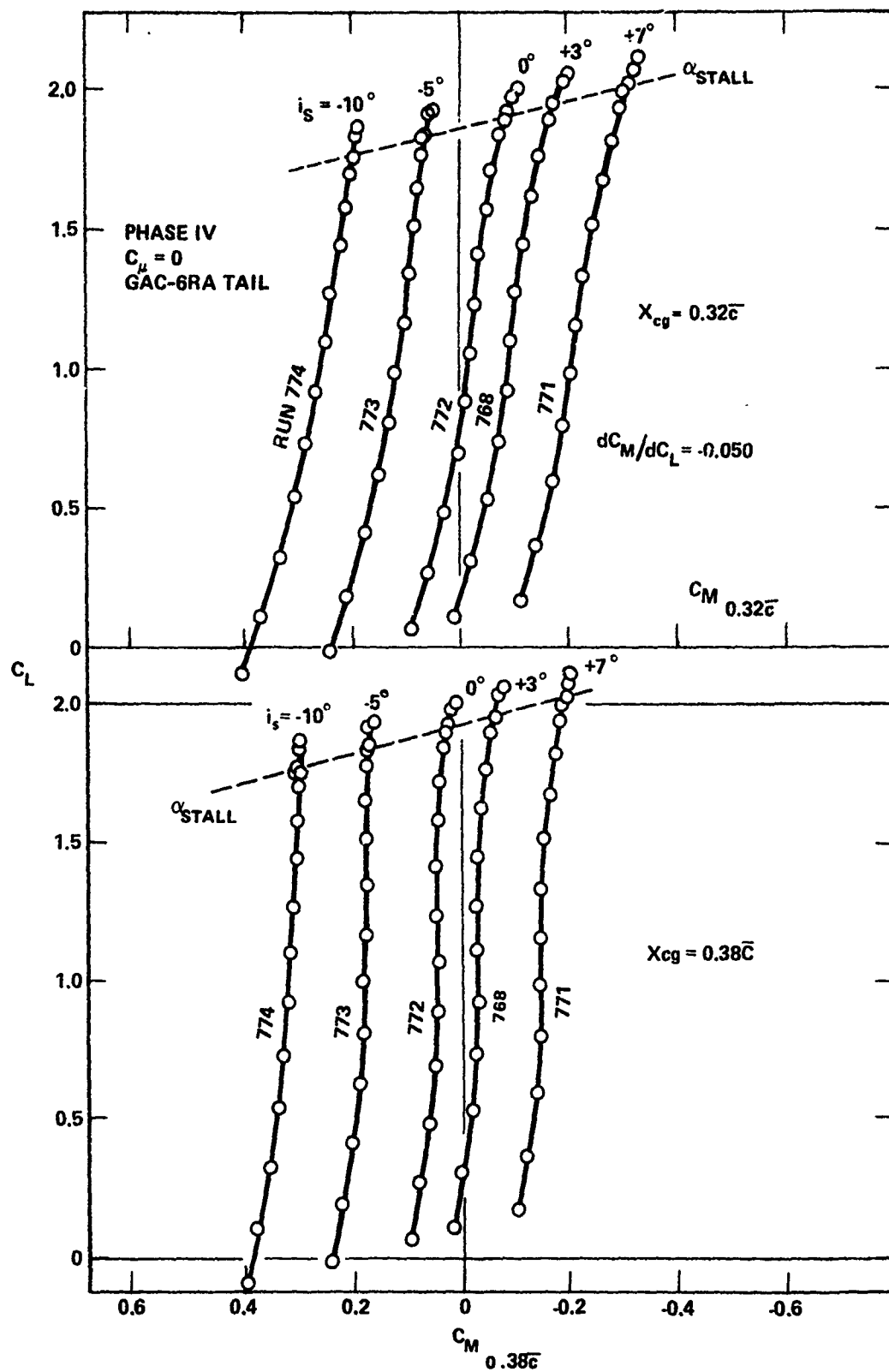


Figure 45 - Effect of Center-of-Gravity Location on Unblown Longitudinal Stability

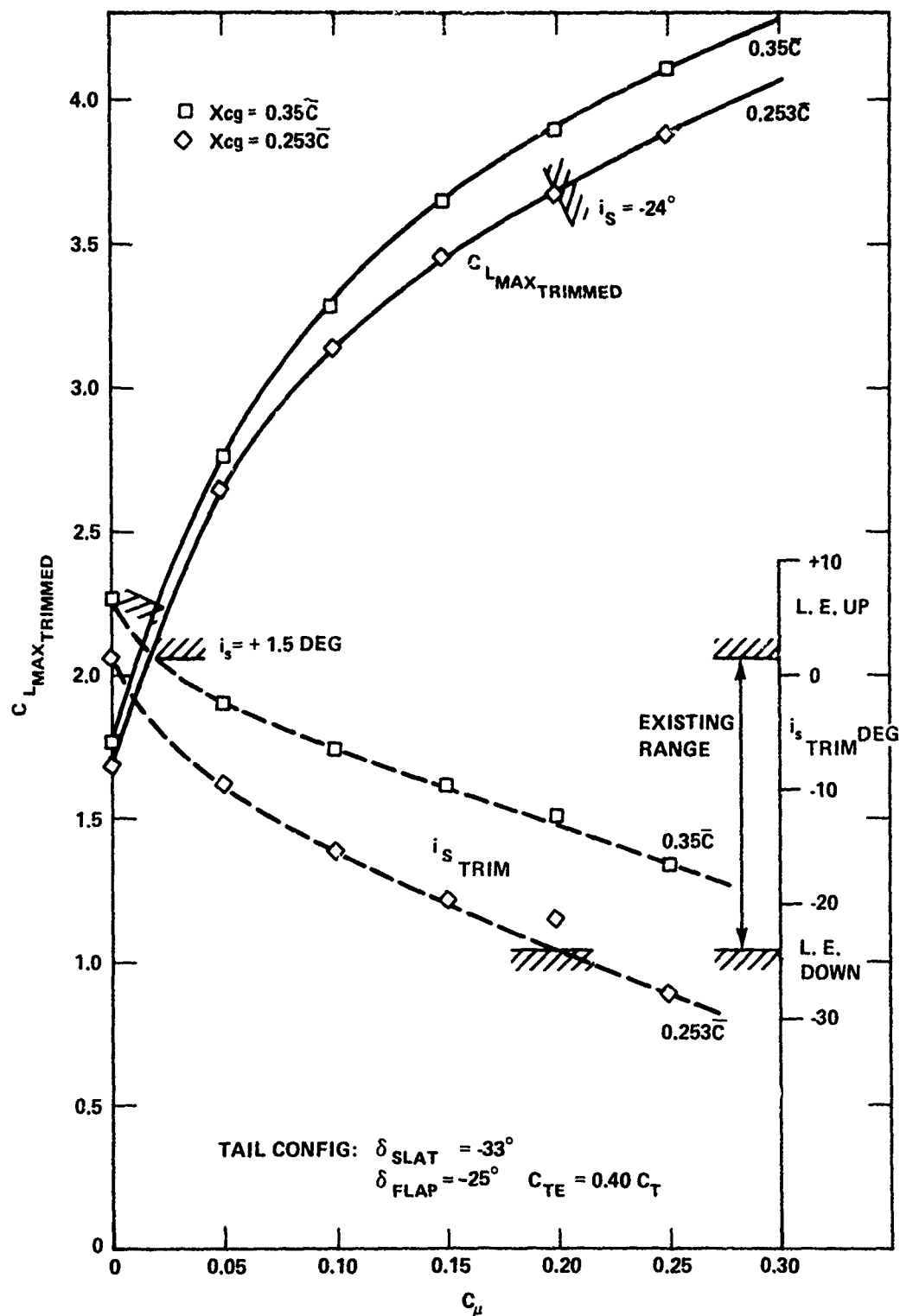


Figure 46 - Trimmed C_{Lmax} and Required Tail Incidence for Optimum Phase I Configuration

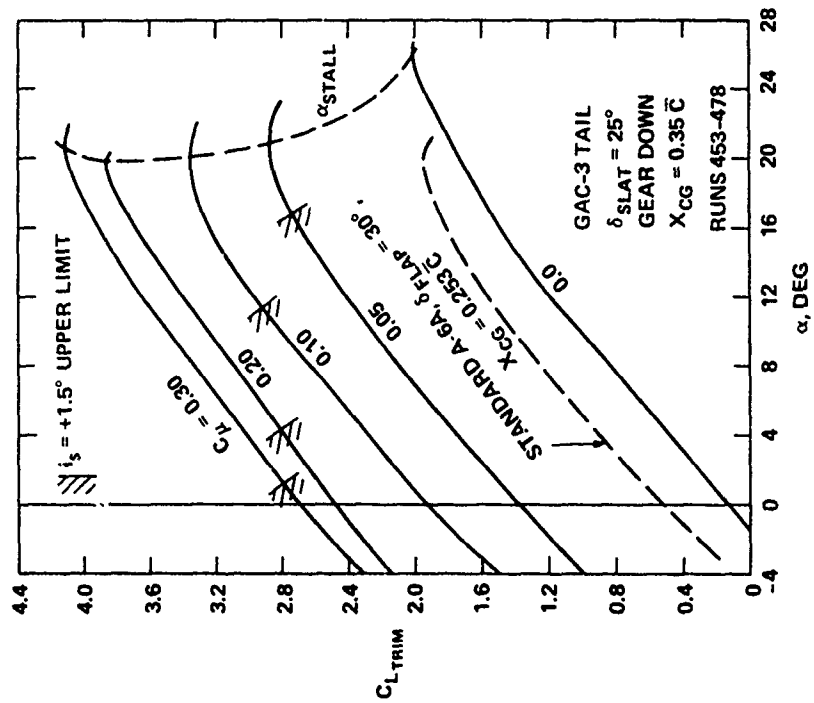
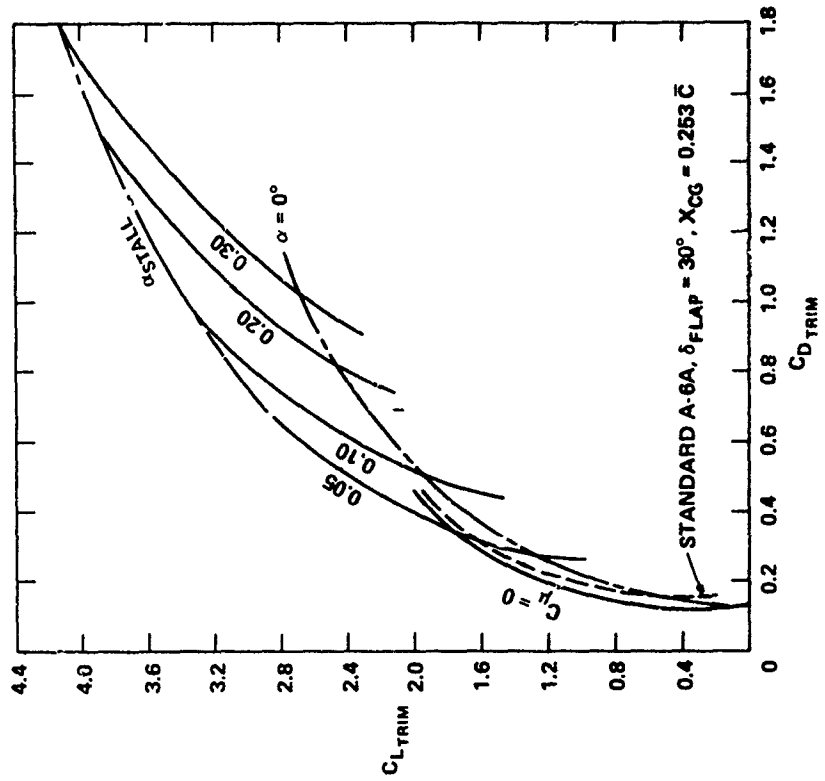


Figure 47 - Trimmed Aerodynamic Data for the Final Phase II Configuration

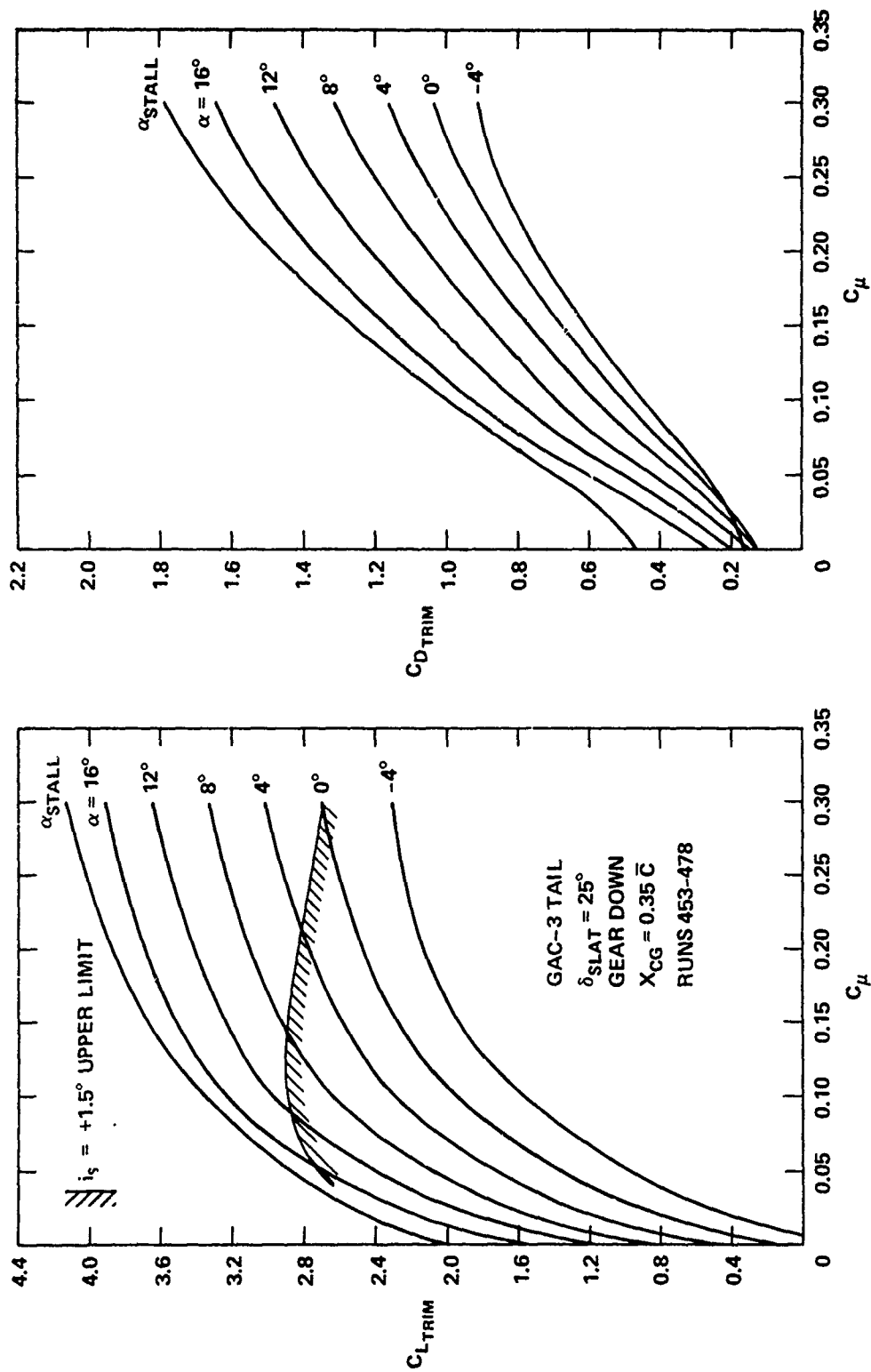


Figure 48 - Lift and Drag Coefficient Variation
with Blowing (Phase II)

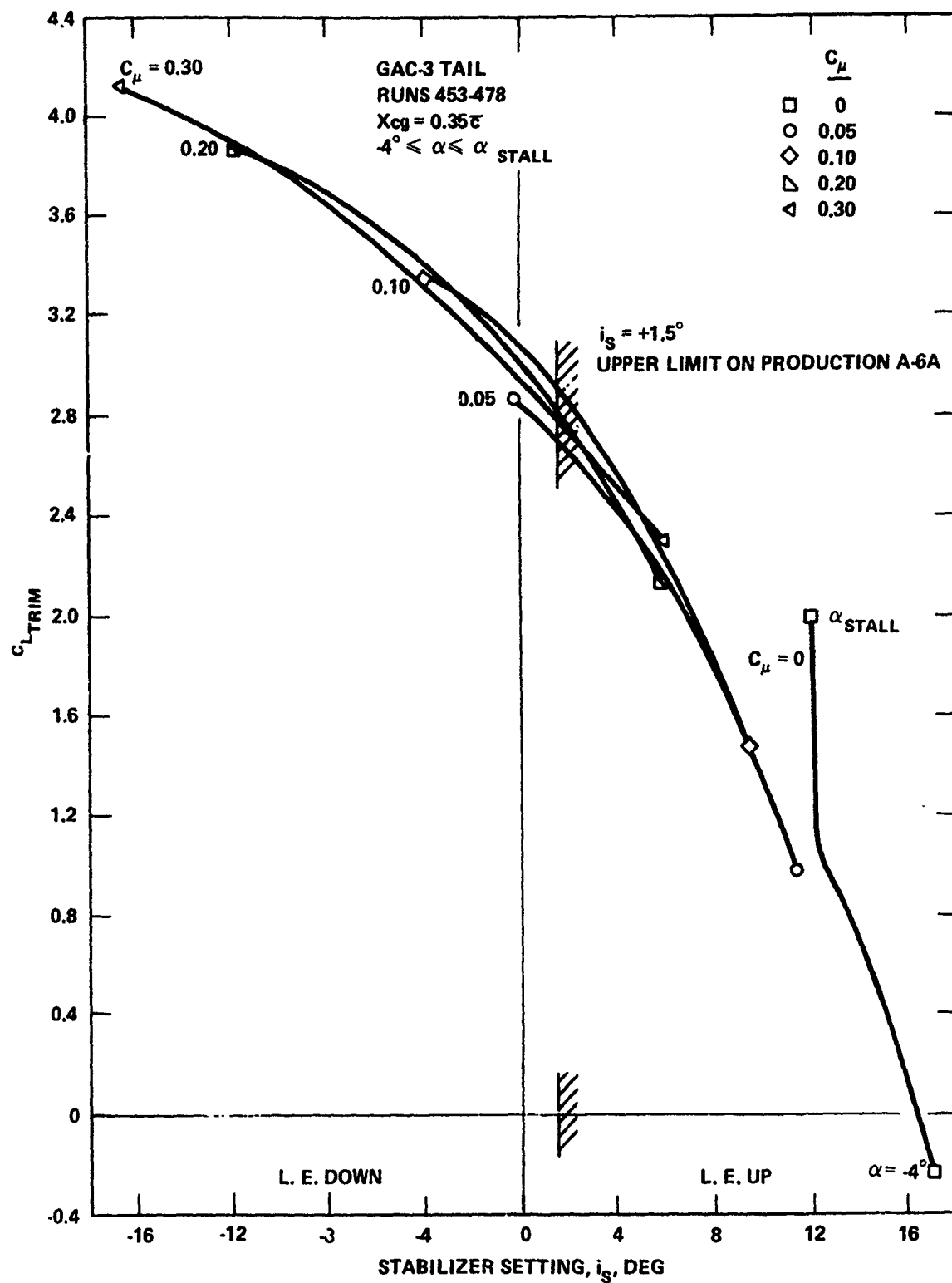


Figure 49 - Tail Incidence Required to Trim
Final Phase II Configuration

The figure consists of two graphs showing trim characteristics.

Top Graph: Plots $C_{L\text{TRIM}}$ (Y-axis, 0 to 4.0) versus $C_{D\text{TRIM}}$ (X-axis, 0 to 1.8). The graph shows curves for $\alpha = 0^\circ$ to 180° . The curves are labeled $\alpha = 0^\circ$, 10° , 20° , 30° , 40° , 50° , 60° , 70° , 80° , 90° , 100° , 110° , 120° , 130° , 140° , 150° , 160° , 170° , and 180° . The curves show a minimum $C_{D\text{TRIM}}$ value for each α . The graph is labeled "A-6A $\delta_t = 30^\circ$ (REF 12)" and "A-6A CLEAN (REF 12, 0.0165 ADDED TO CONVERT TO MODEL SCALE)".

Bottom Graph: Plots $C_{L\text{TRIM}}$ (Y-axis, 0 to 4.0) versus α , DEG (X-axis, -4 to 28). The graph shows curves for α STALL and $\alpha = 0^\circ$ to 10° . The curves are labeled $\alpha = 0^\circ$, 10° , 20° , 30° , 40° , 50° , 60° , 70° , 80° , 90° , 100° , 110° , 120° , 130° , 140° , 150° , 160° , 170° , and 180° . The graph is labeled "EC-40 - 10-D TAIL GEAR DOWN RUNS 732-752" and "A-6A CLEAN (REF 12) ADJUSTED TO $\alpha = 15^\circ$ LIMIT".

106

Figure 50 (Continued)

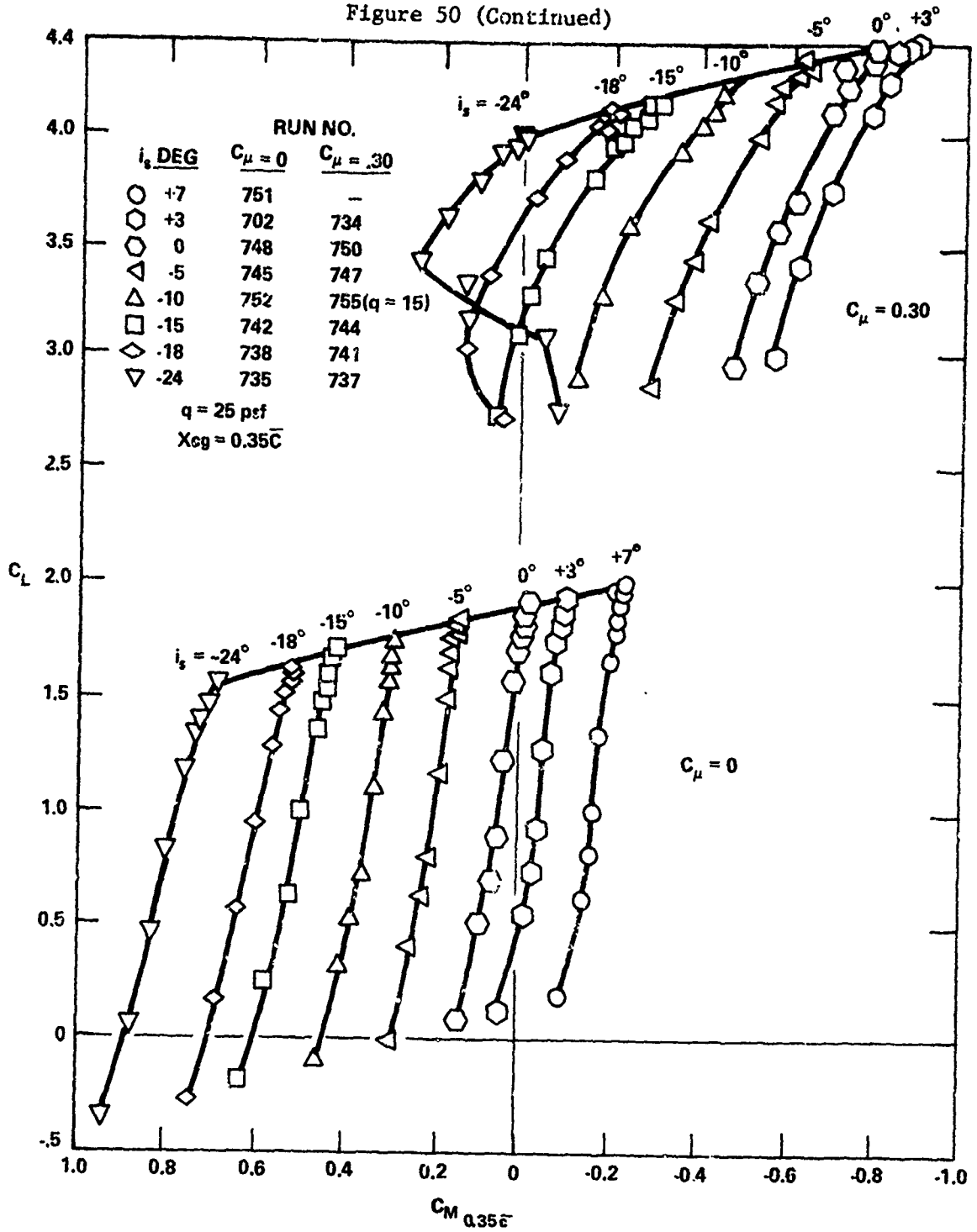


Figure 50b - Pitching Moment at $X_{cg} = 0.35\bar{c}$

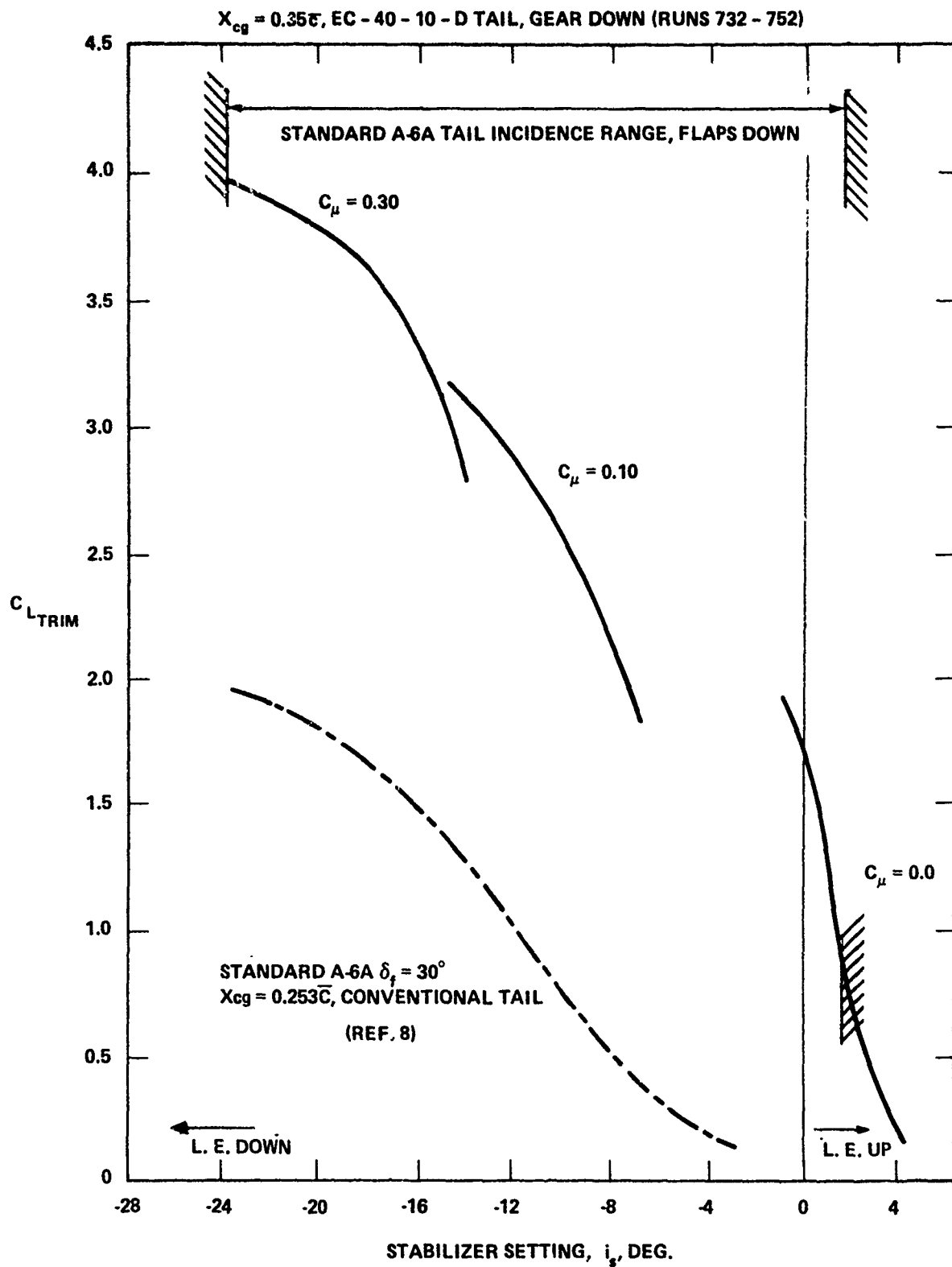


Figure 51 - Tail Incidence Required to Trim
 Final Phase III Configuration

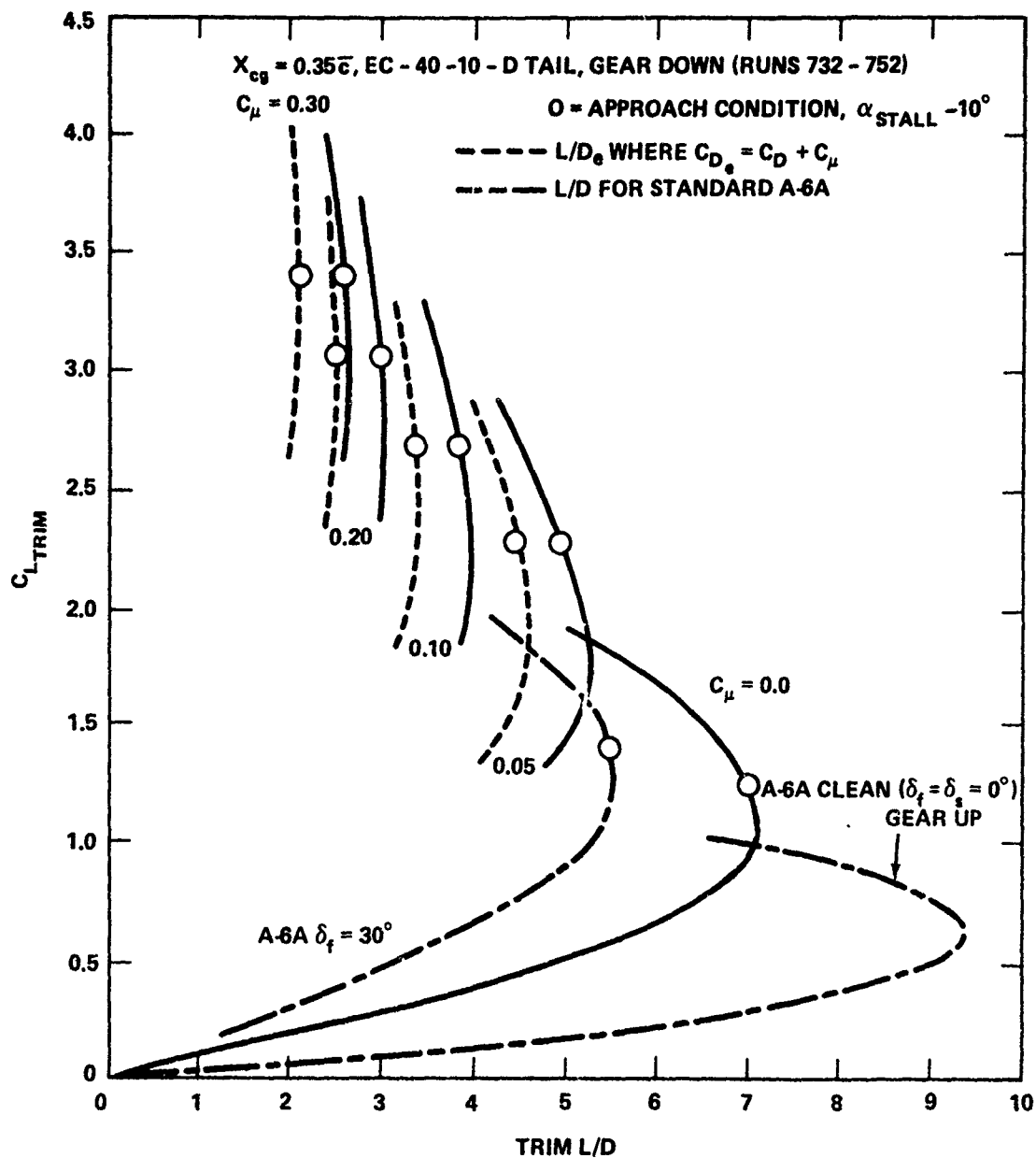


Figure 52 - Trim Lift-To-Drag Ratio for the Final Phase III Configuration

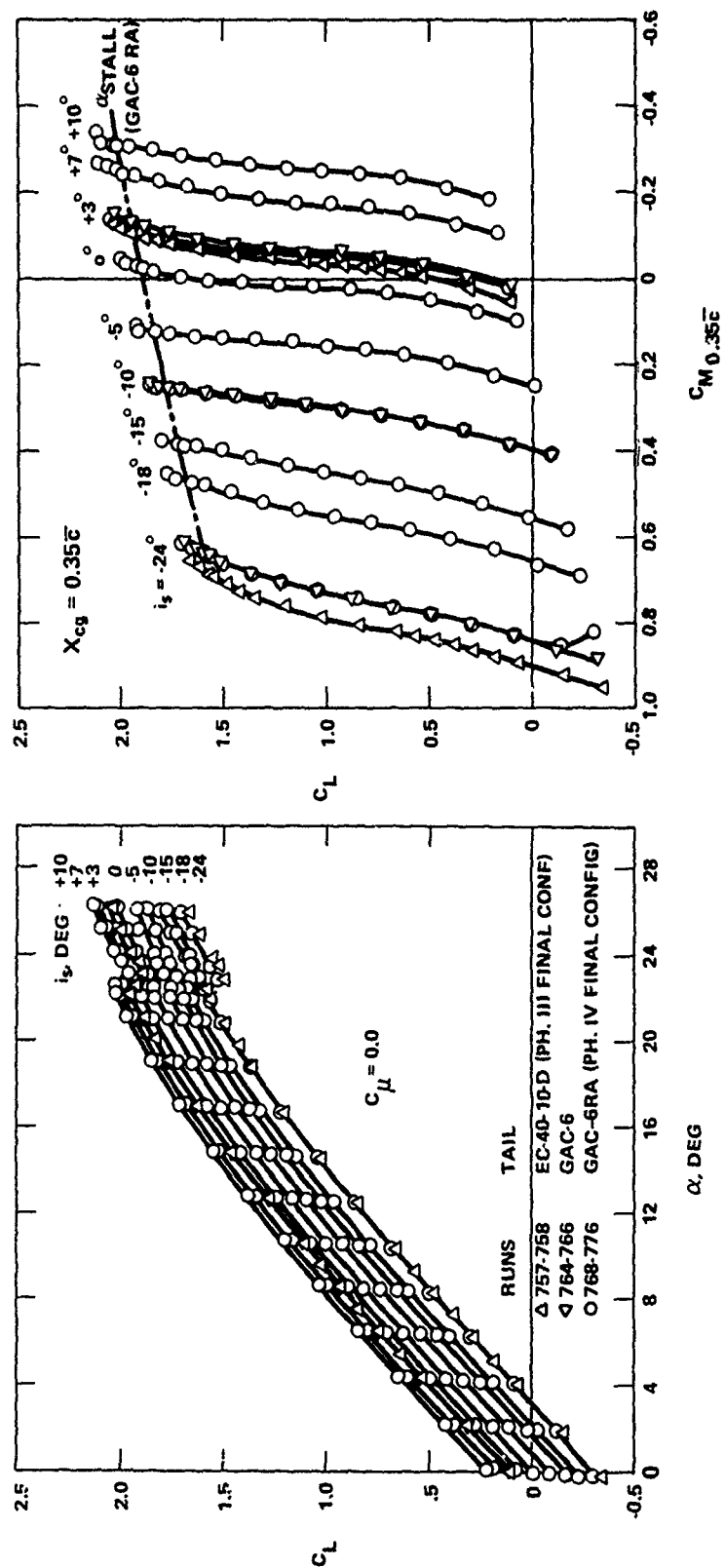


Figure 53 - Effect of Tail Incidence on the
Phase IV Configurations, $C_{\mu} = 0$

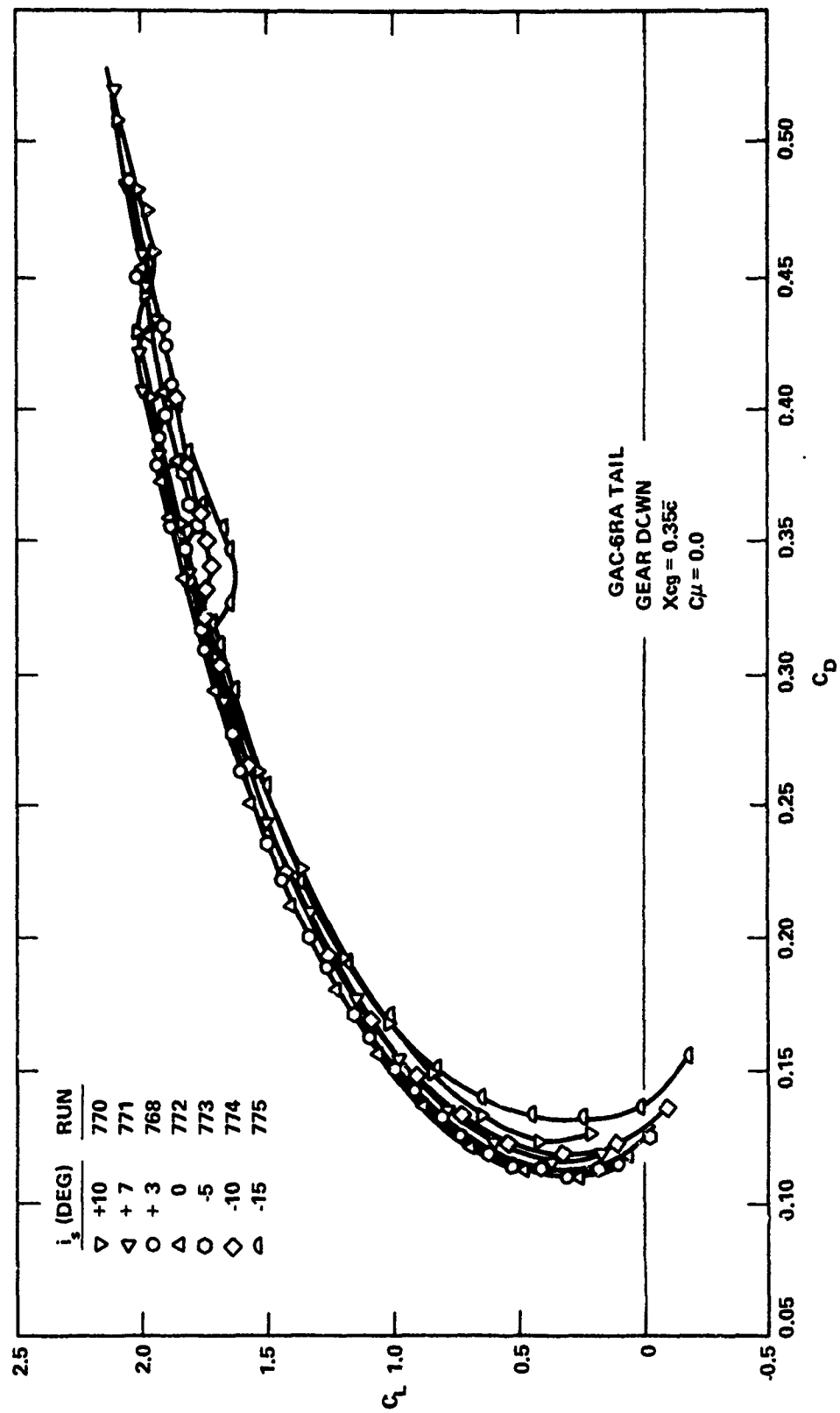


Figure 54 - Effect of Tail Incidence on Final Phase IV Configuration Drag Polars

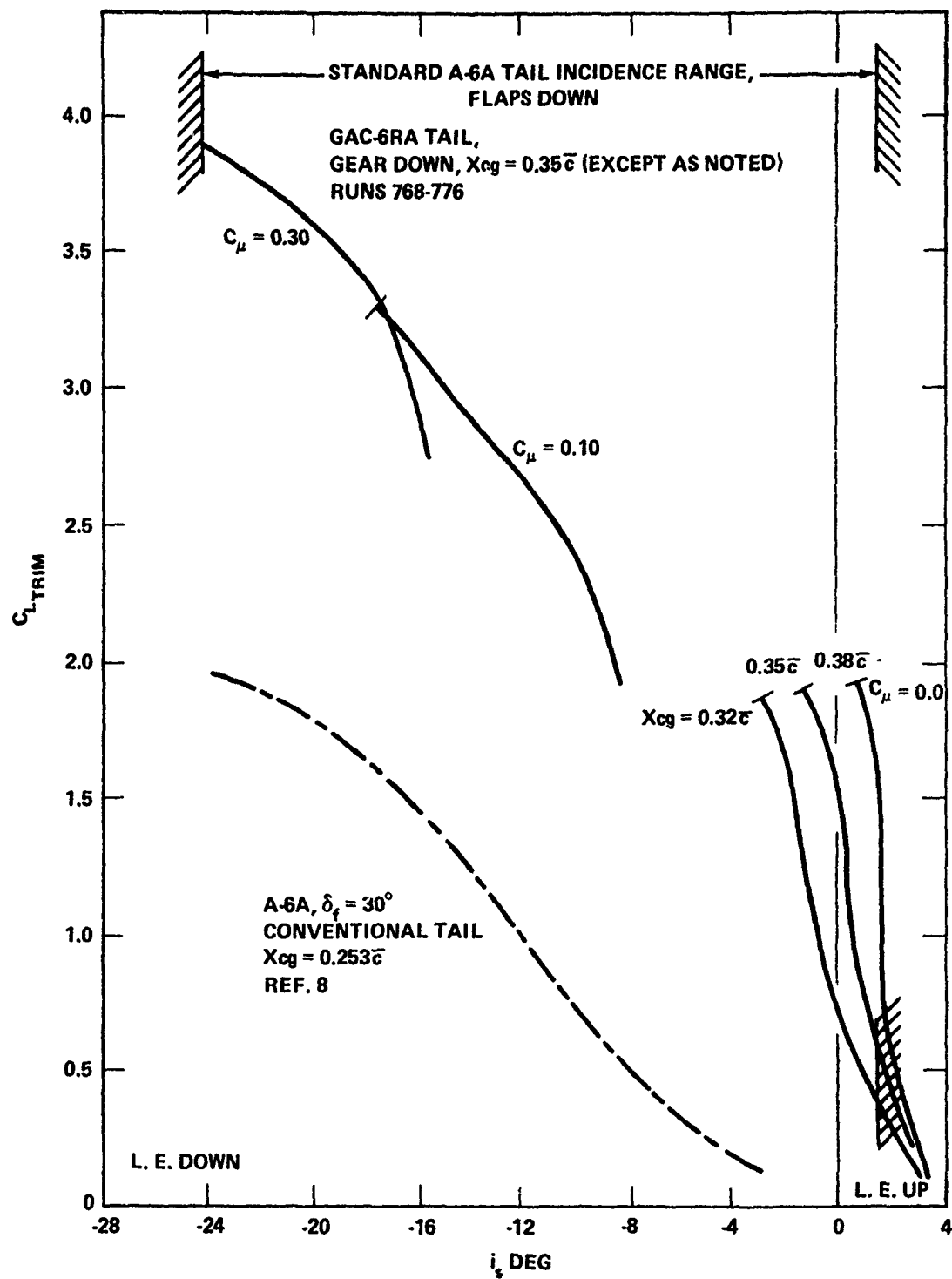


Figure 56 - Tail Incidence Required to Trim
Final Phase IV Configuration

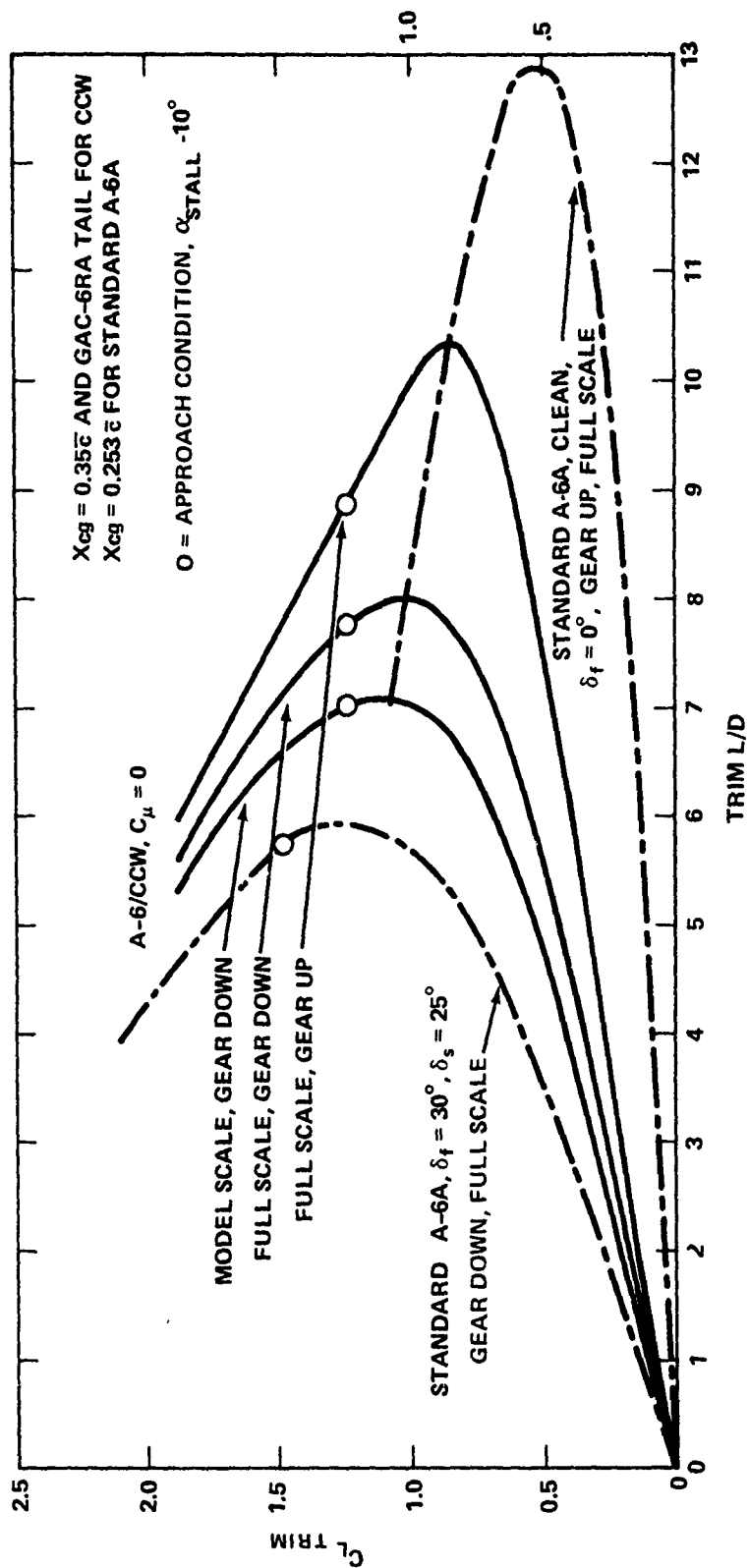


Figure 57 - Lift-to-Drag Ratio for the Final Phase IV Configuration, Unblown

Figure 58 - Effect of GAC-6RA Tail Deflection
on Final Phase V Flight Demonstrator
Configuration

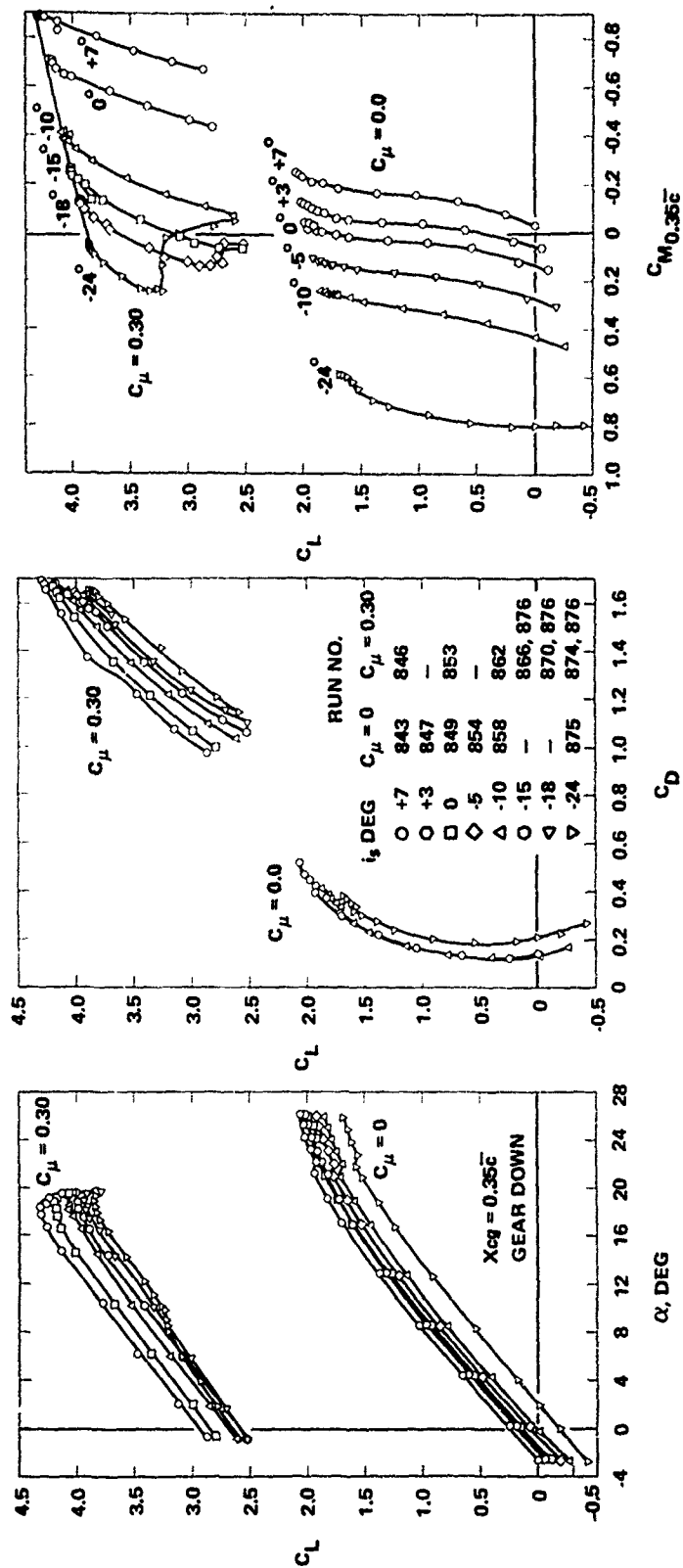


Figure 58a - $C_\mu = 0.0$ and 0.30

Figure 58 (Continued)

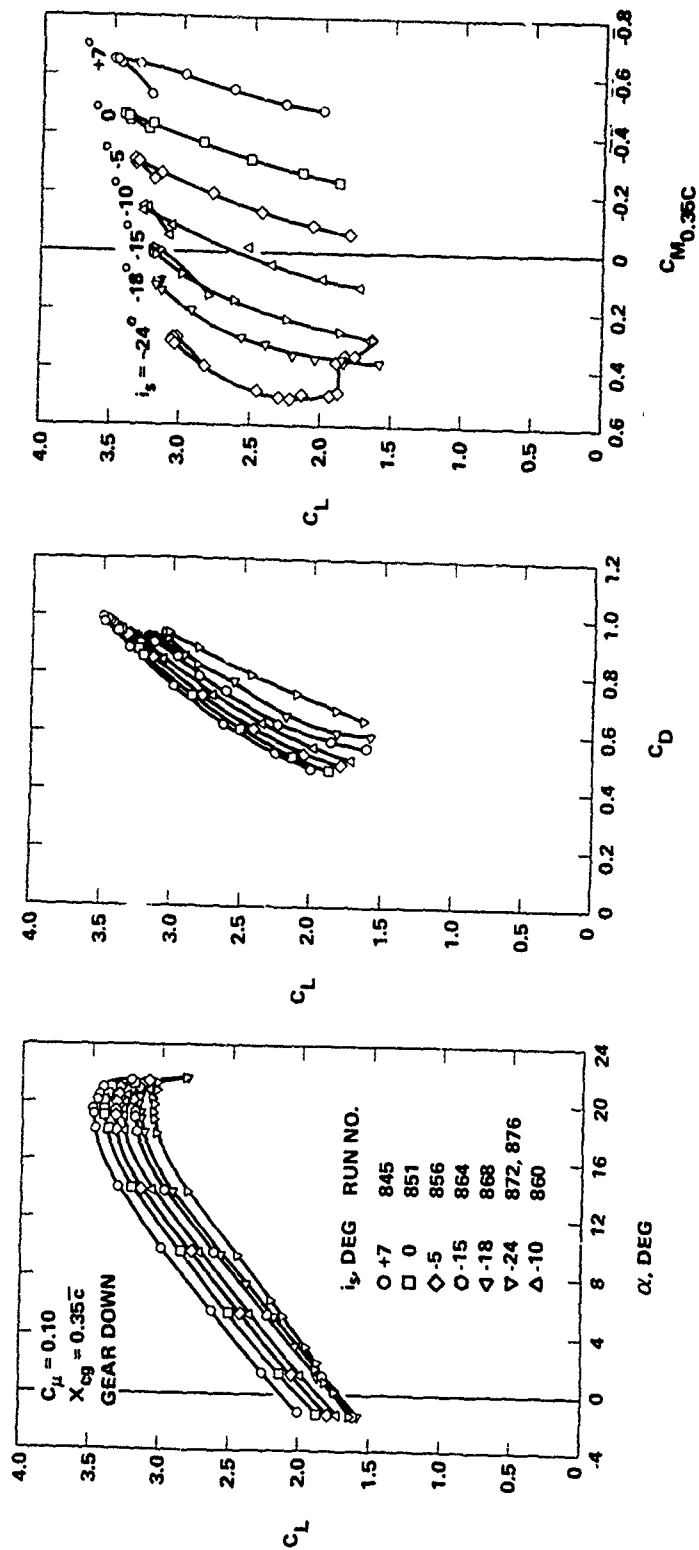


Figure 58b - $C_{\mu} = 0.10$

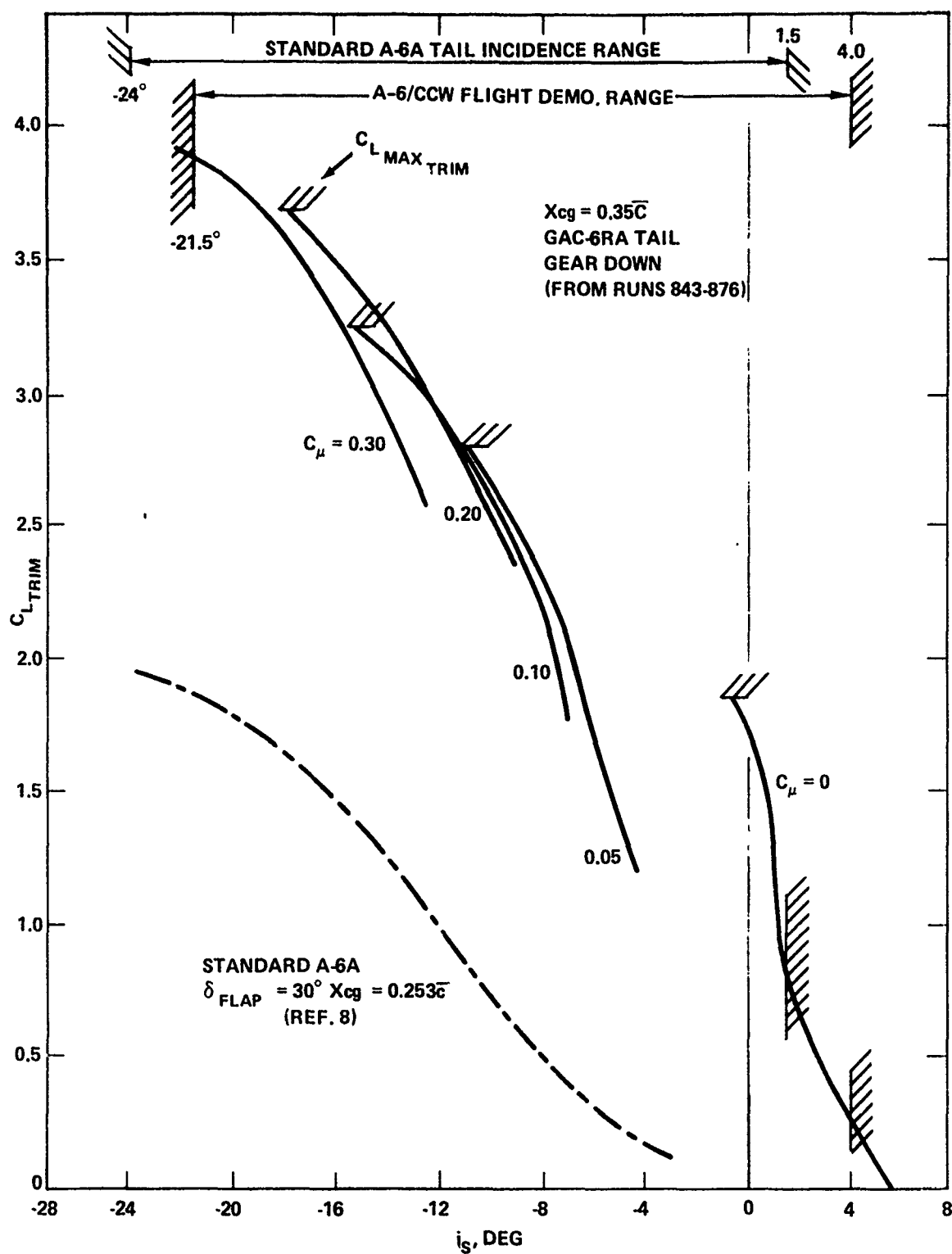


Figure 60 - Tail Incidence Required to Trim
Phase V Flight Demonstrator Configuration

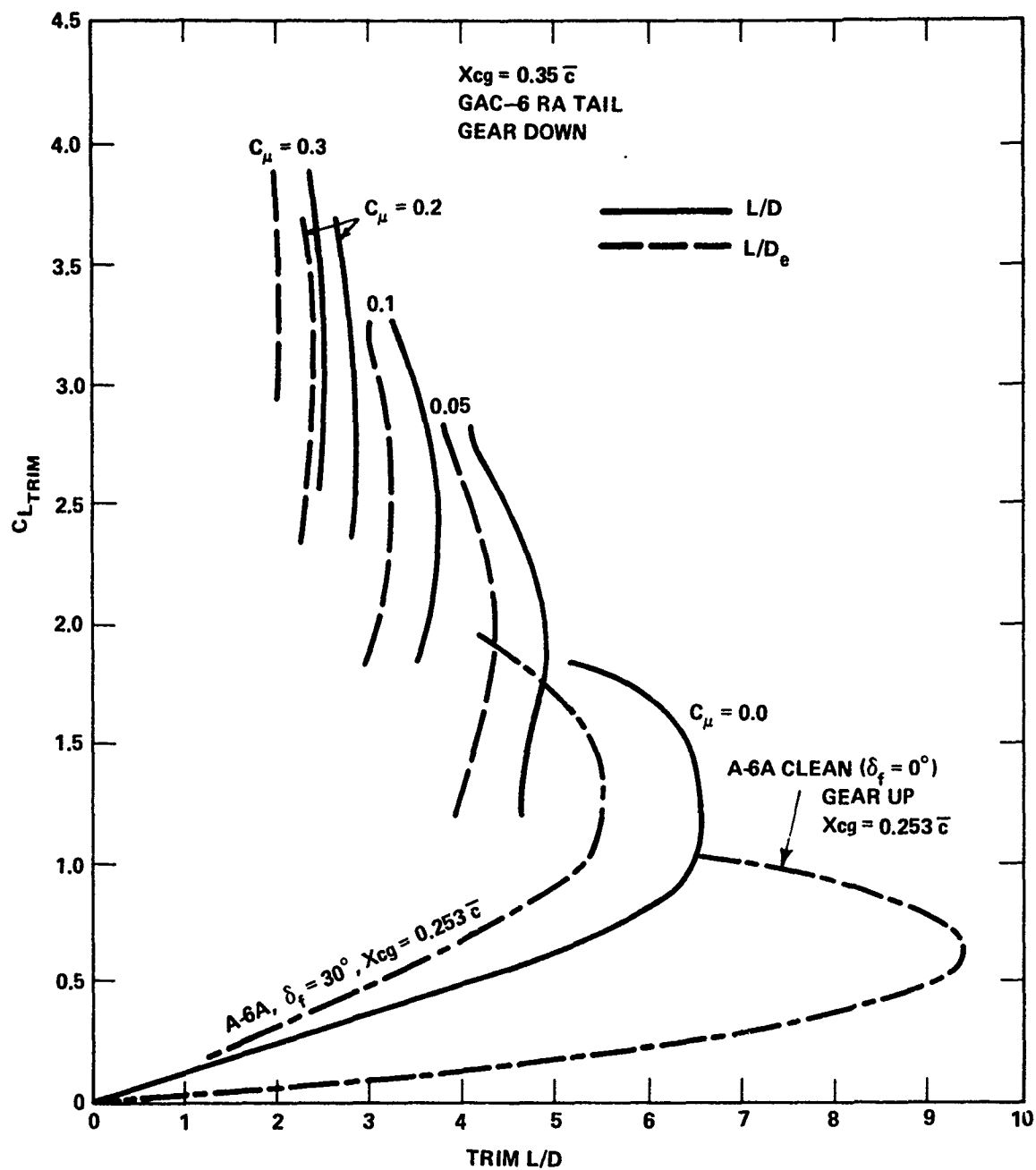
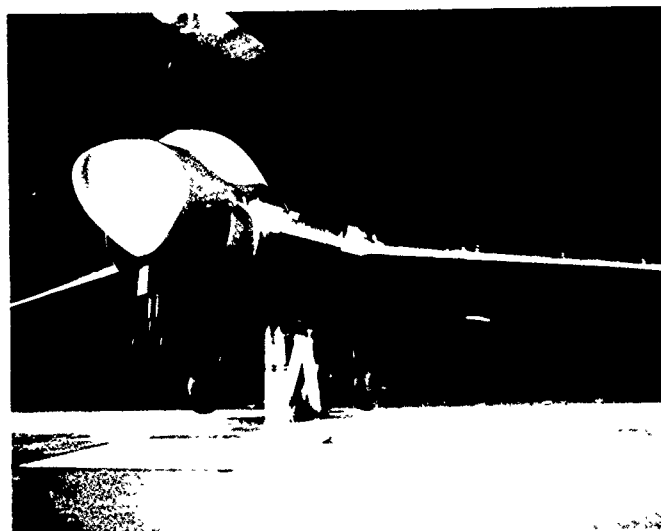
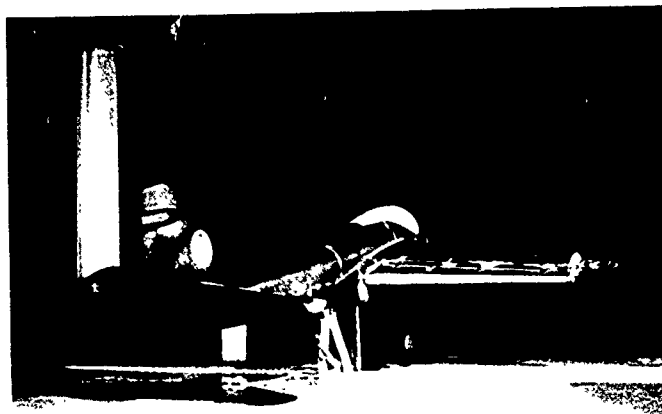
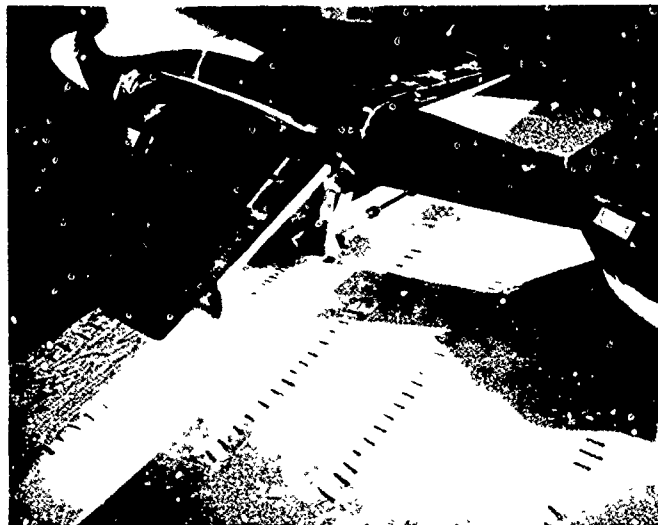


Figure 61 - Trim Lift-to-Drag Ratio for the Phase V Flight Demonstrator Configuration



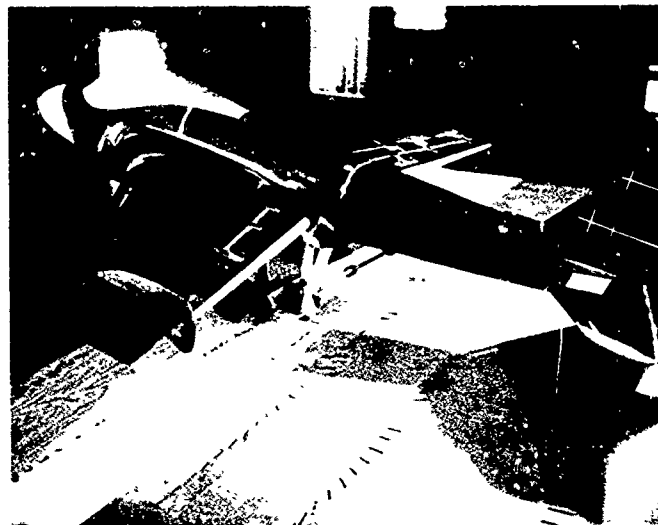
$\alpha_p = 13^\circ$
 $C = 15.388 \text{ IN.}$
 $h_g/z = 0.833$

Figure 62 - Ground Plane Installation in Phase II



$$C_{\mu} = 0 \quad C_L = 1.36 \quad C_D = 0.173$$

$$i_s = +10^\circ$$



$$C_{\mu} = 0.21 \quad C_L = 3.23 \quad C_D = 0.988$$

$$i_s = -10^\circ$$

$$\alpha_g = 13^\circ$$

$$\frac{h_g}{c} = 0.833$$

$$\frac{c}{c} = 15.388 \text{ IN.}$$

Figure 63 - Tuft Photographs of
Flow Over Ground Plane in
Phase II

Figure 64 - Trimmed Aerodynamic Data for
Final Phase II Configuration in
Ground Effect

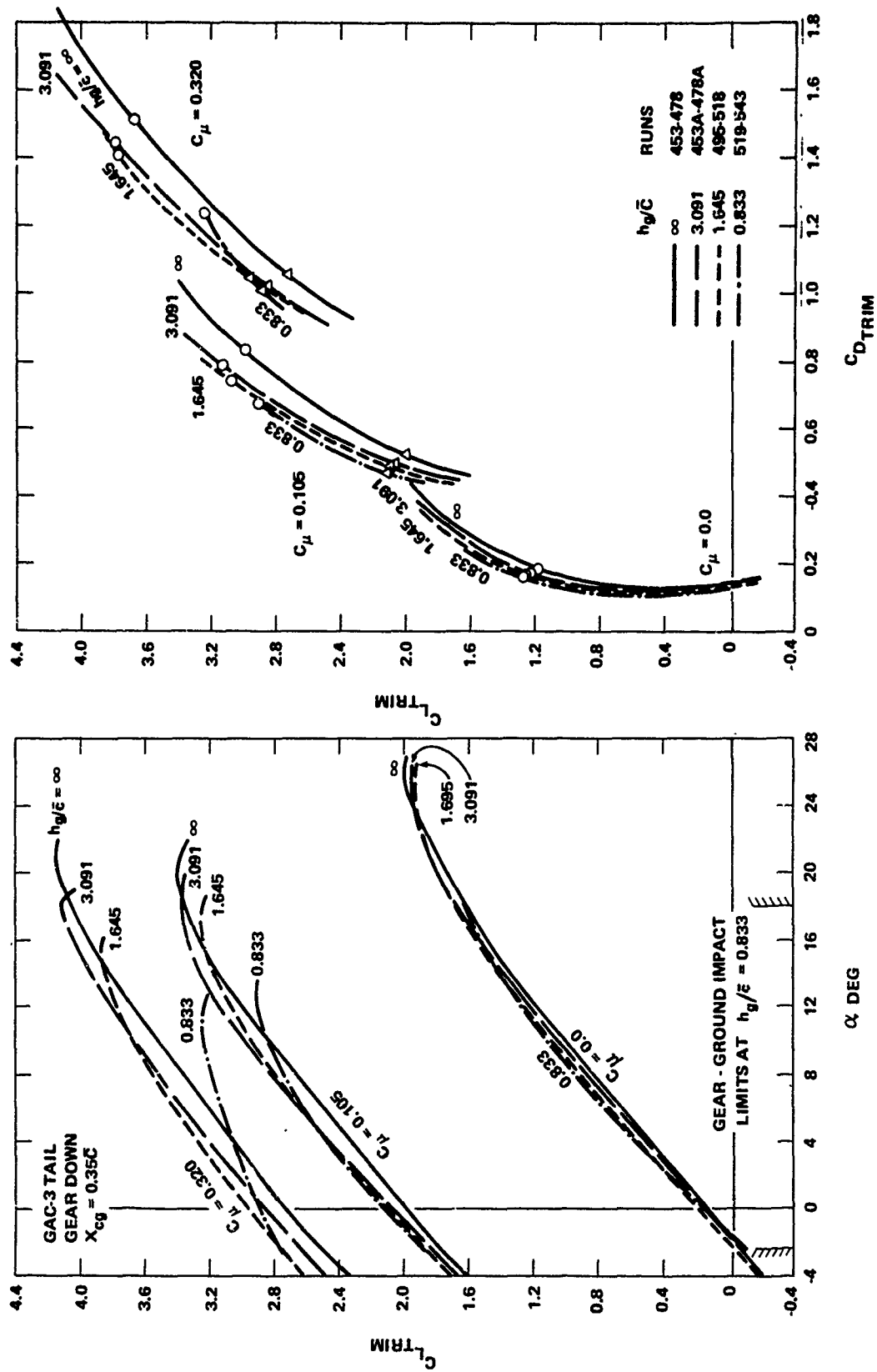


Figure 64a - $C_{\mu} = 0, 0.105$ and 0.320

Figure 64 (Continued)

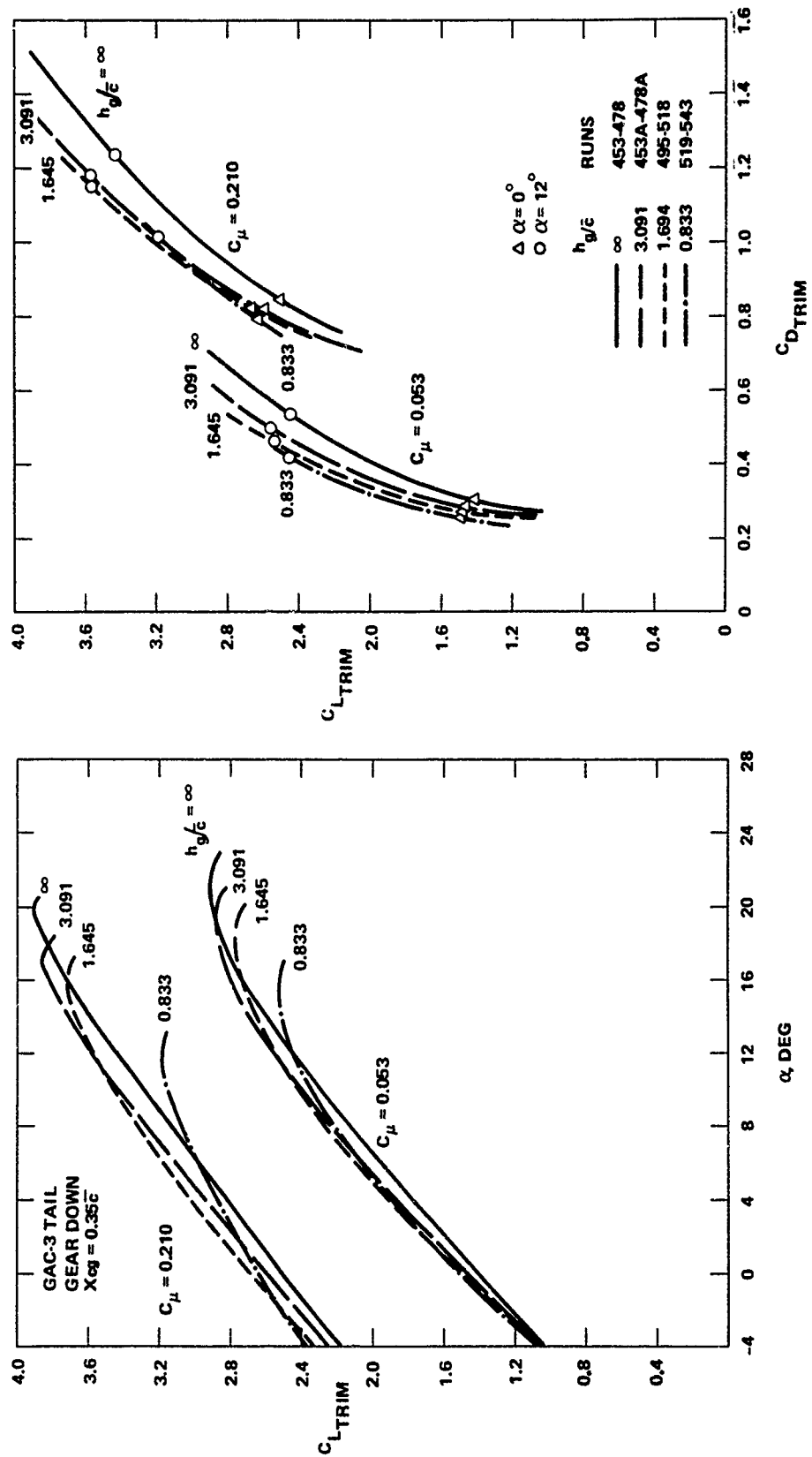


Figure 64b - $C_\mu = 0.053$ and 0.210

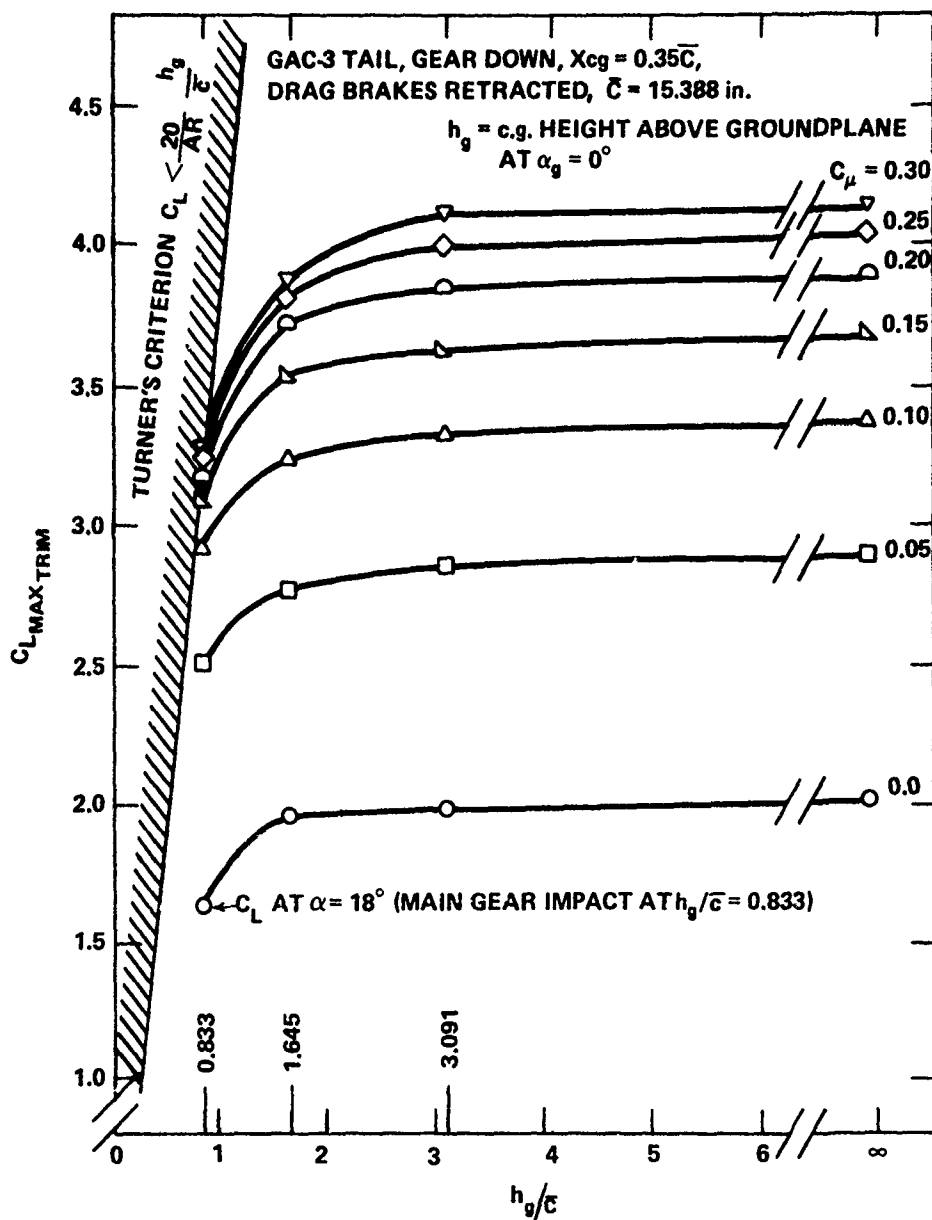


Figure 65 - Ground Effect on Trimmed Maximum Lift for the Final Phase II Configuration

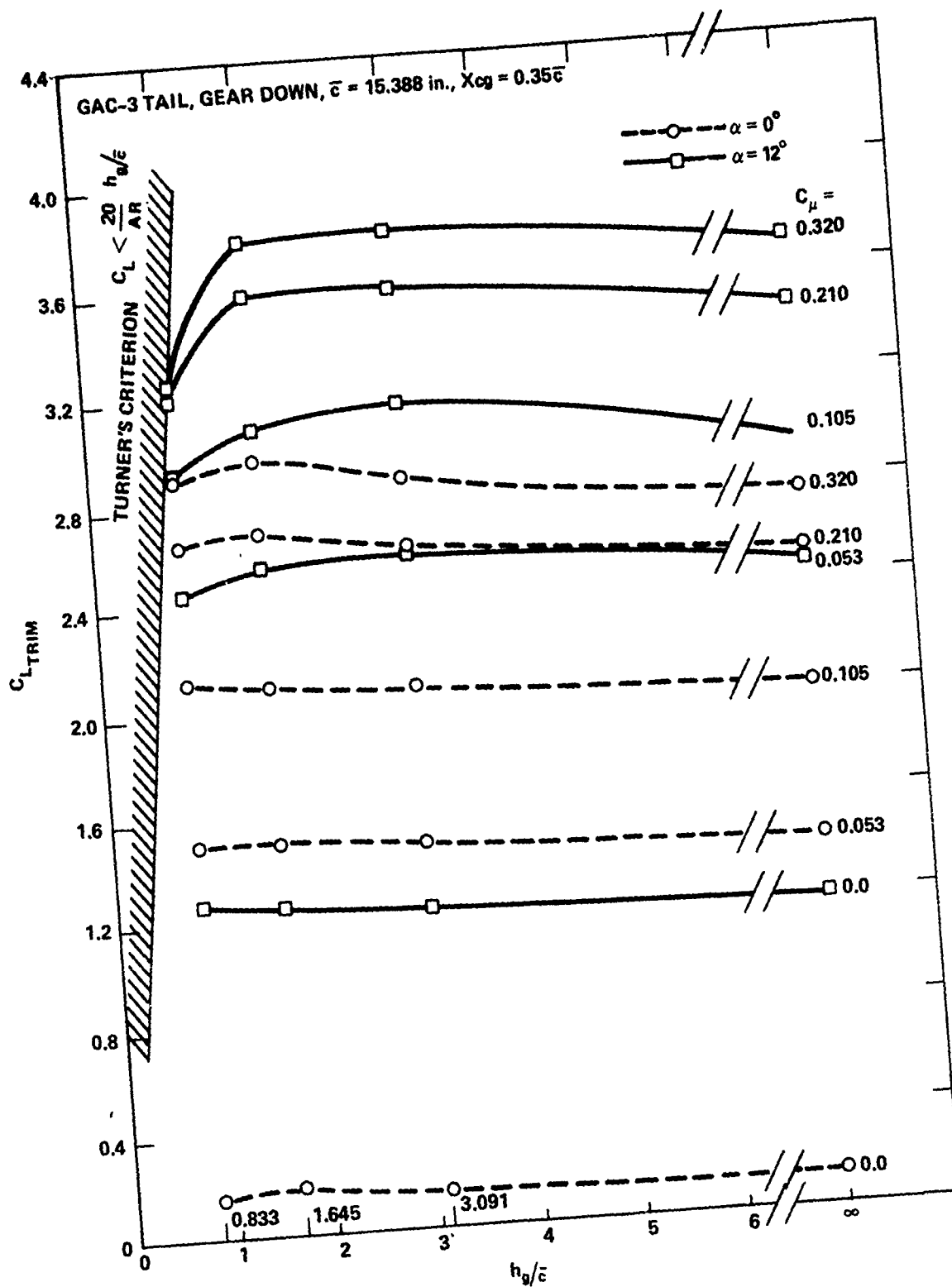


Figure 66 - Ground Effect on Trimmed Lift for Final Phase II Configuration

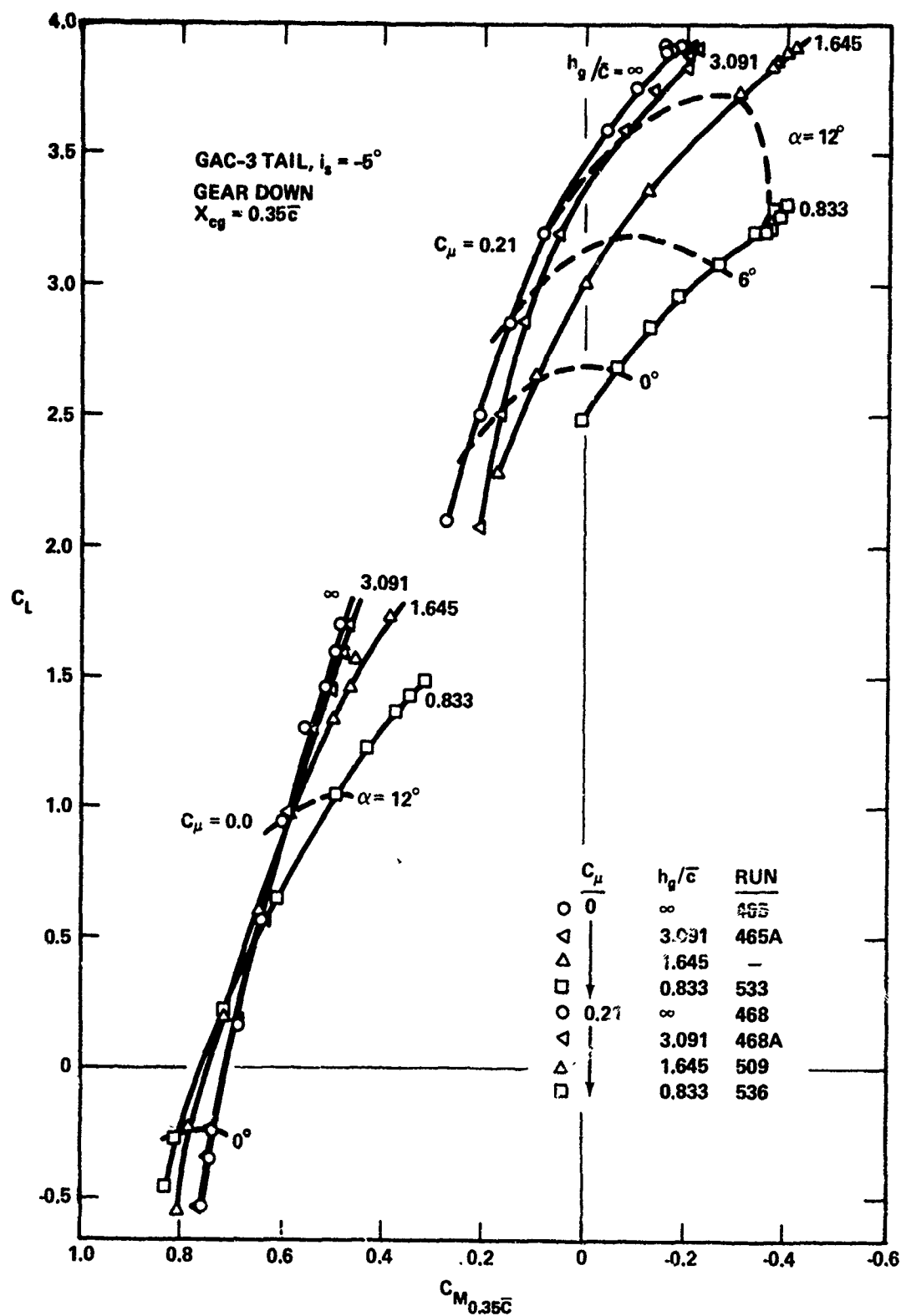


Figure 67 - Ground Effect on Pitching Moment
for Final Phase II Configuration

Figure 68 ~ Drag Generated by Final
Phase I Configuration

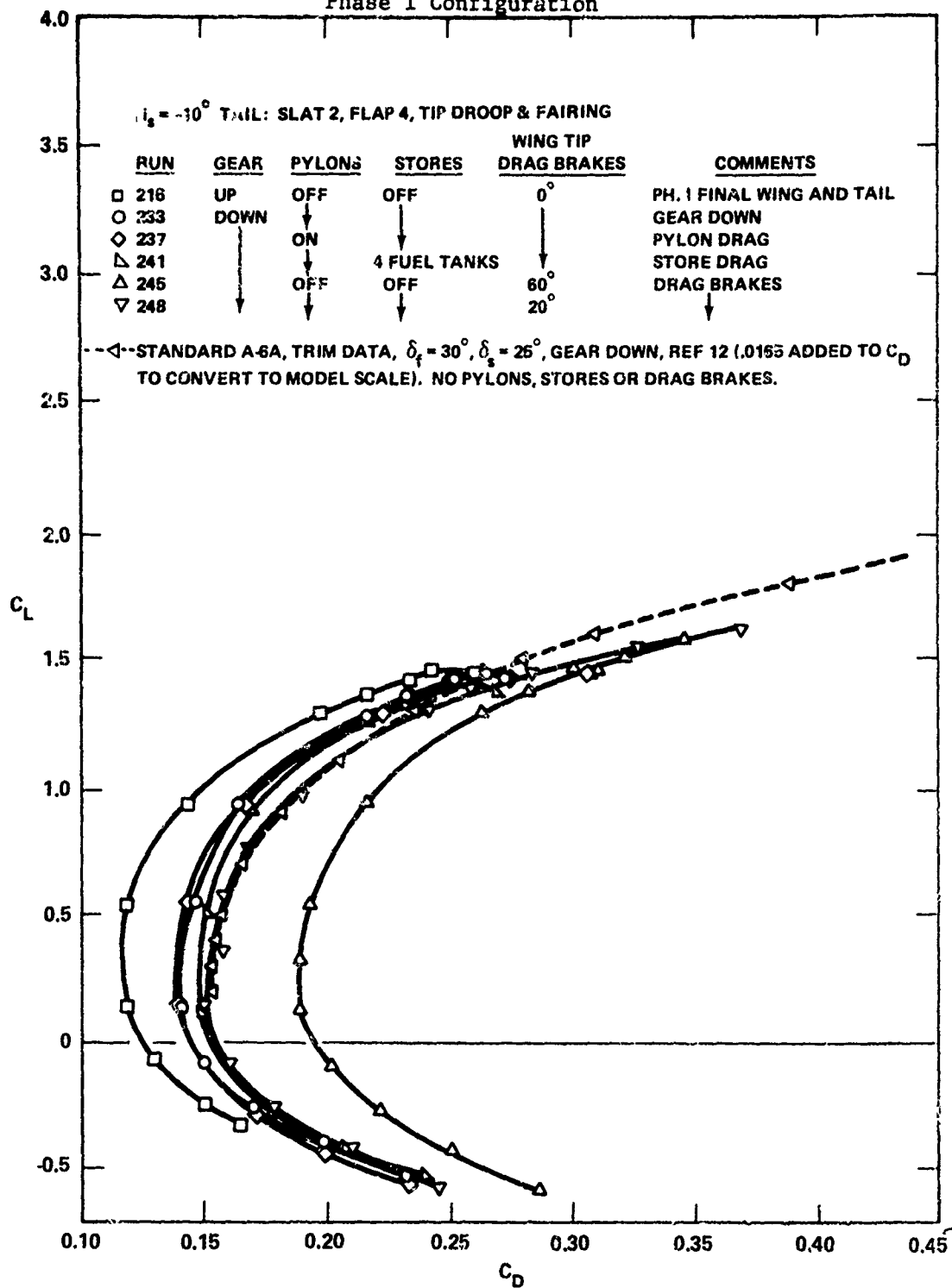


Figure 68a - $C_{\mu} = 0.0$

Figure 68 (Continued)

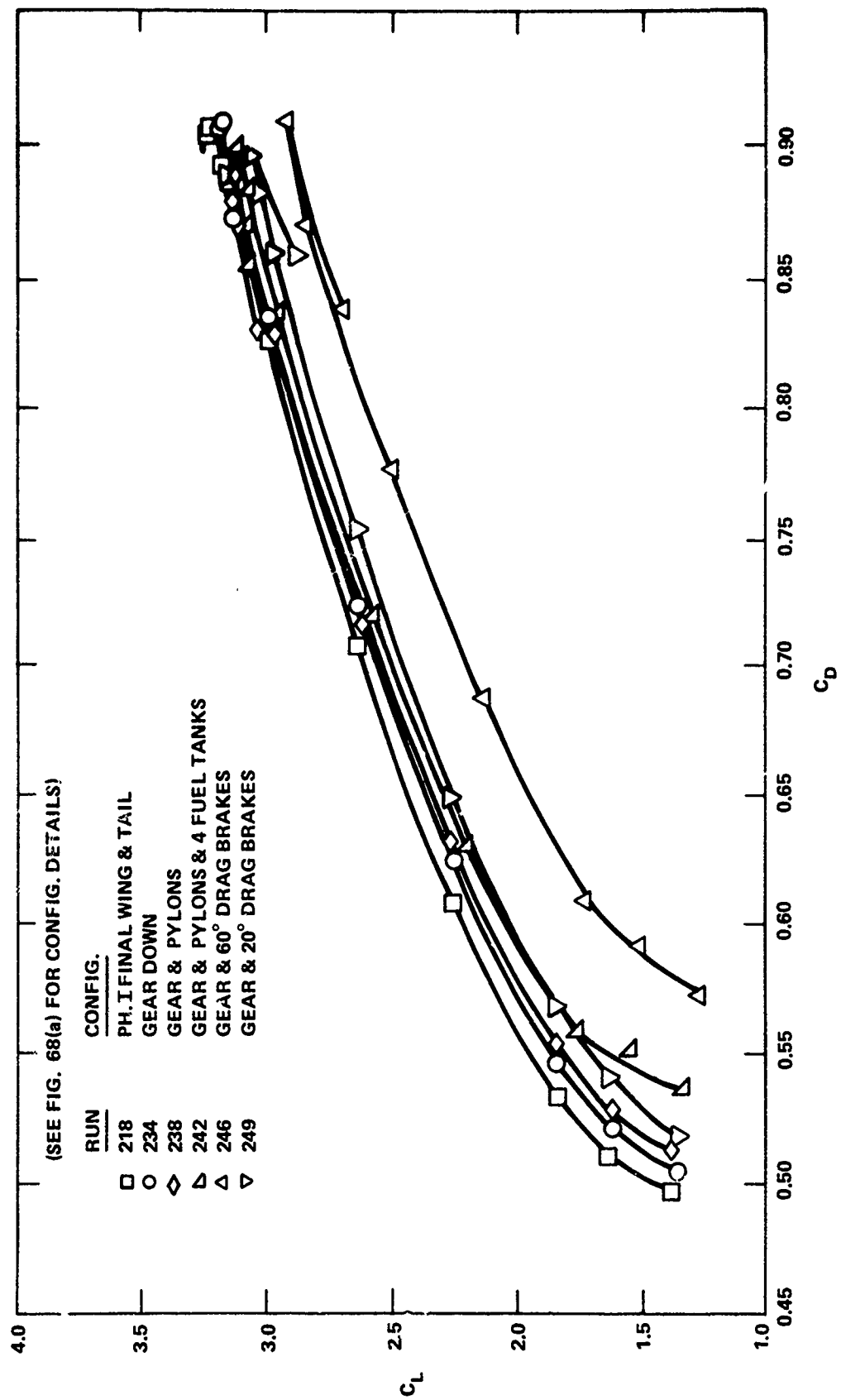


Figure 68b - $C_{\mu} = 0.10$

Figure 68 (Continued)

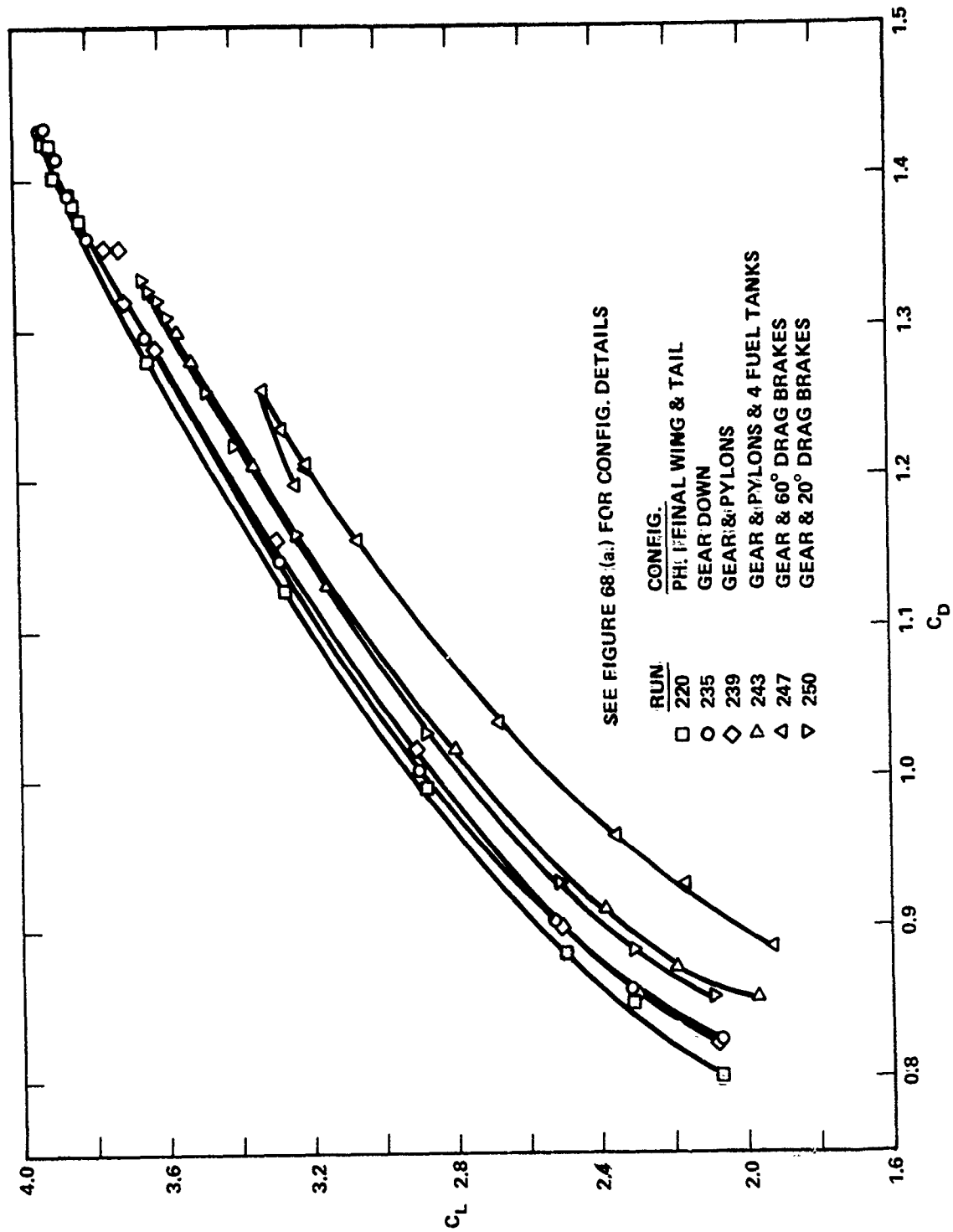


Figure 68c - $C_{\mu} = 0.20$

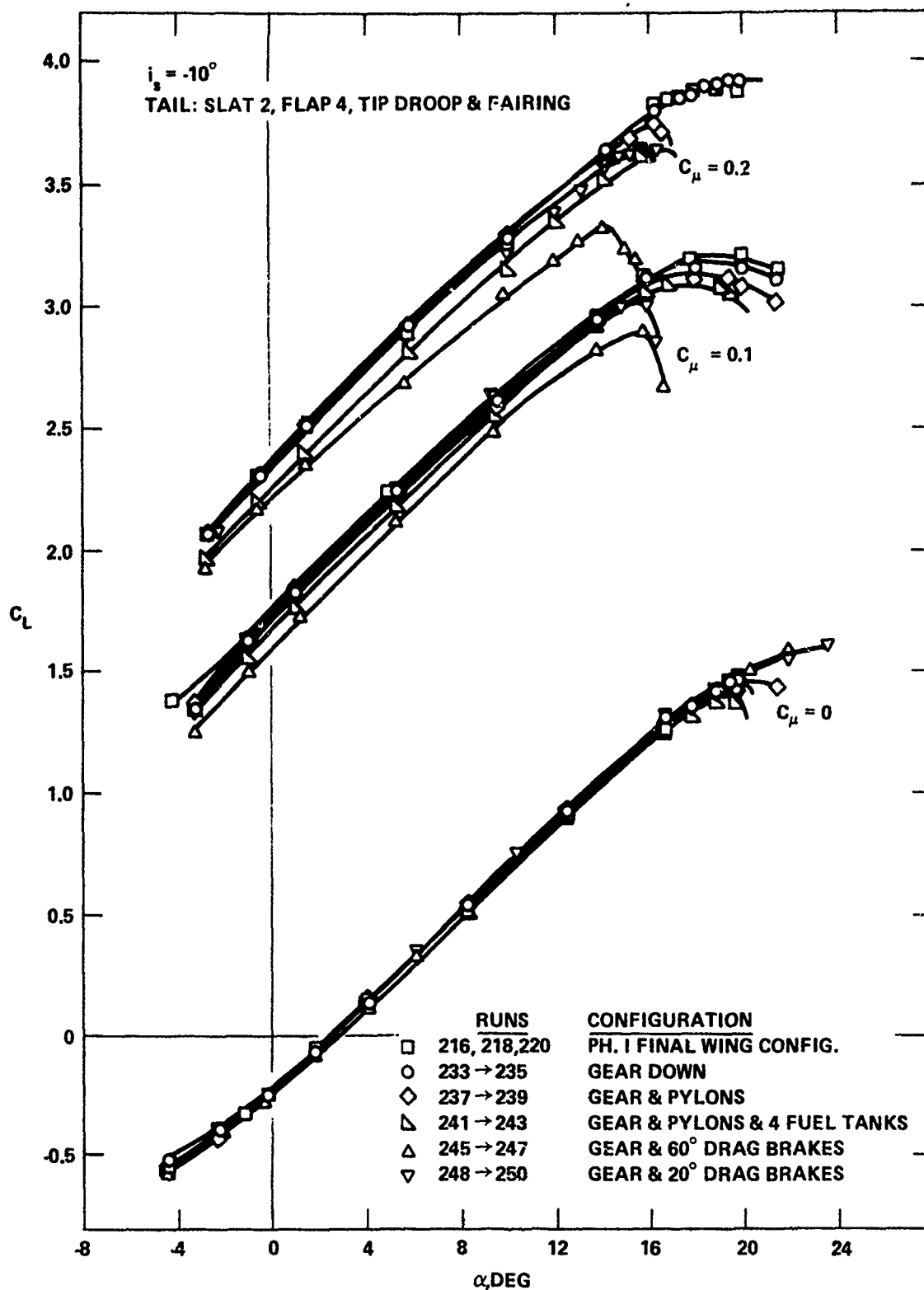


Figure 69 - Effects of Landing Gear, Pylons, Stores, and Wing Tip Speed Brakes on Lift (Phase I)

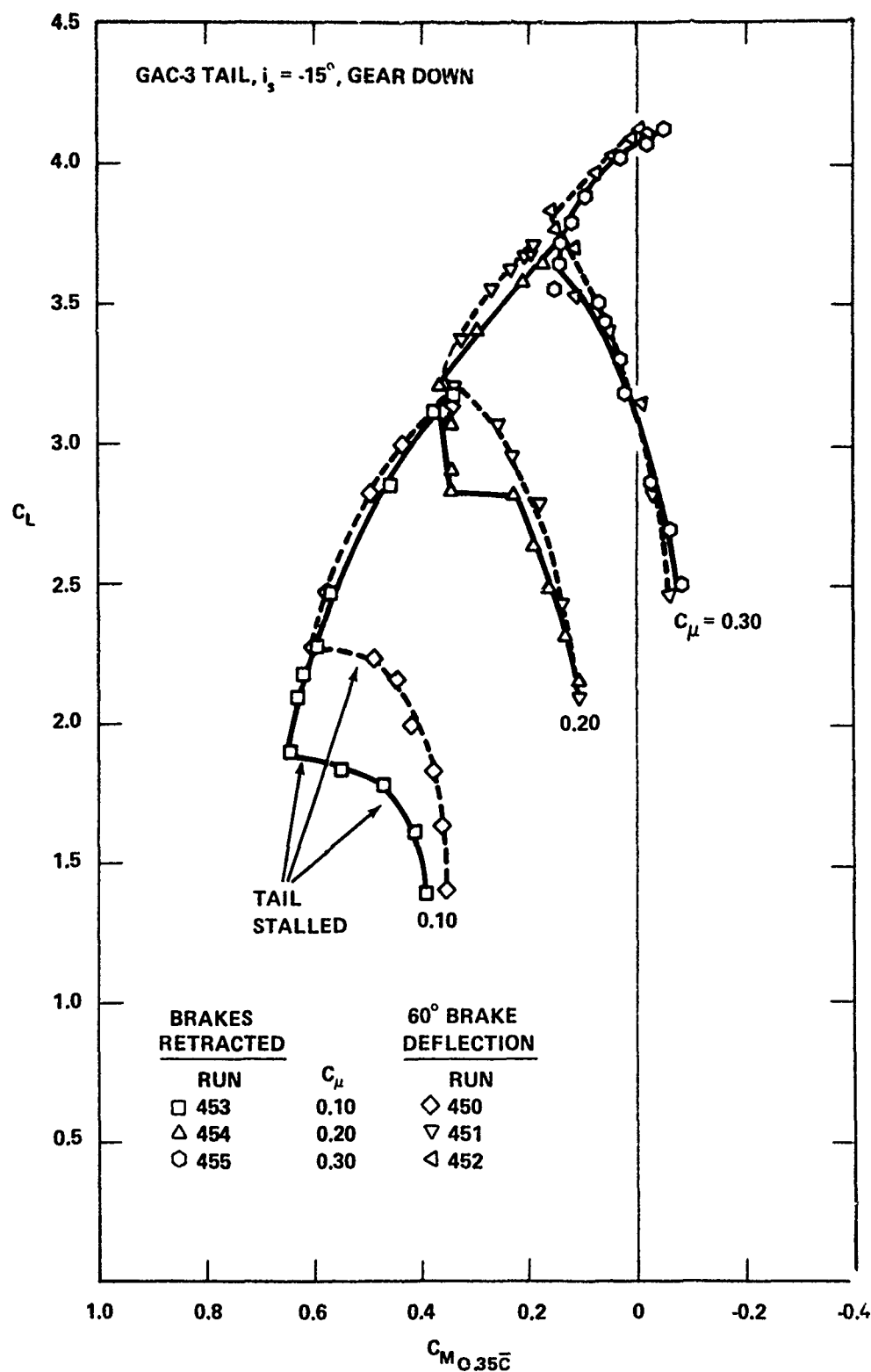


Figure 70 - Effects of Fuselage Speed Brakes on Pitching Moment (Phase II)

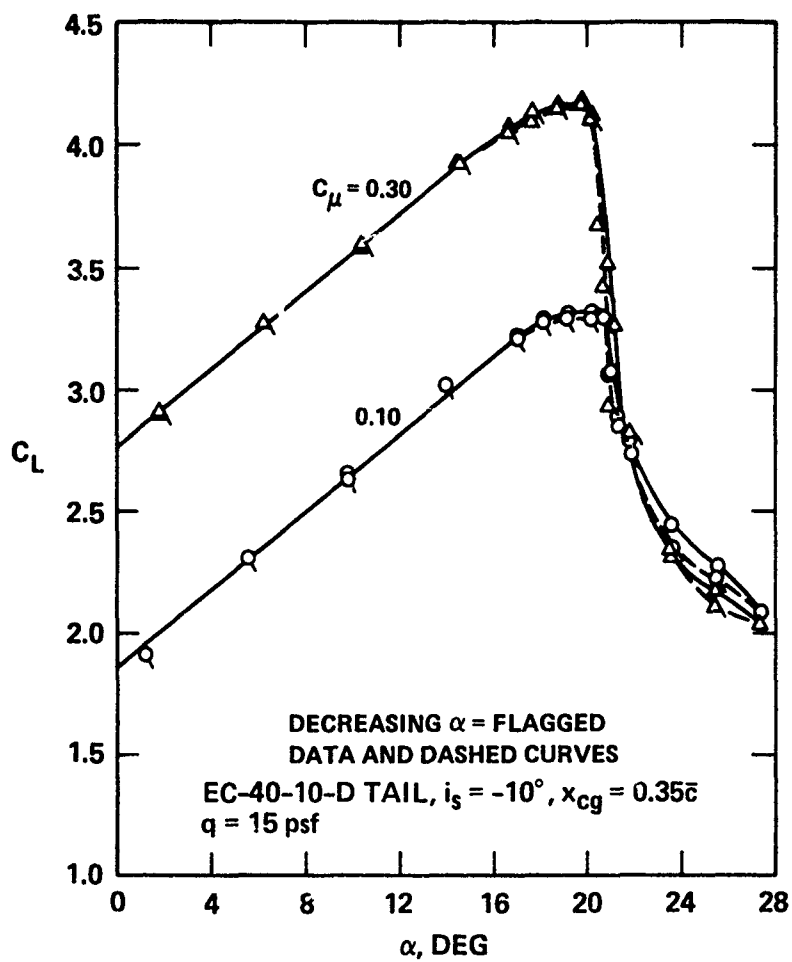


Figure 71 - Post-Stall and Stall Hysteresis Effects on Lift (Phase III)

EC-40-10-D TAIL, $i_s = -10^\circ$, $X_{cg} = 0.35\bar{c}$, $q = 15$ psf
 DECREASING $\alpha =$ FLAGGED DATA AND DASHED CURVES

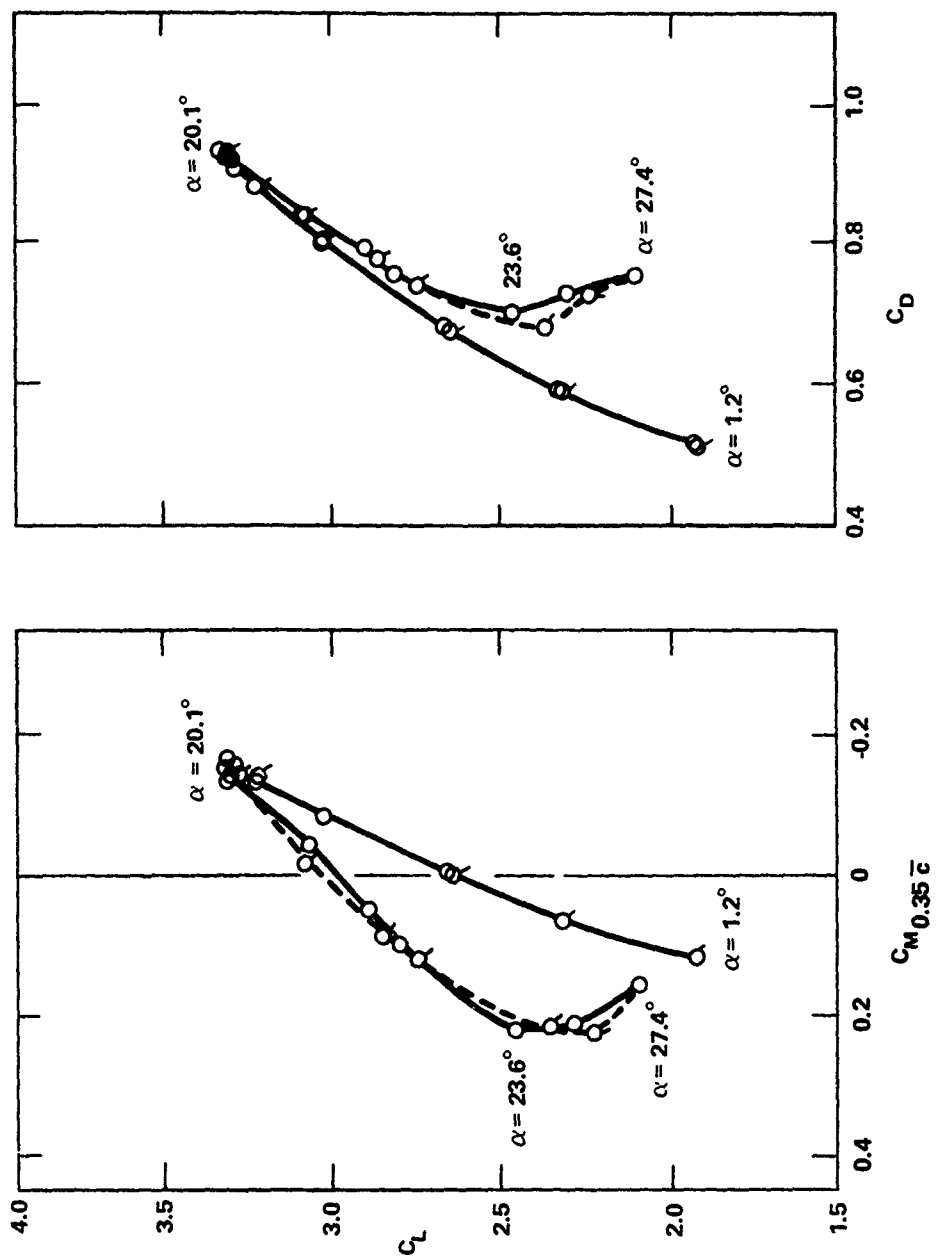


Figure 72 - Post-Stall and Stall Hysteresis
 Effects on Drag and Pitch,
 $C_\mu = 0.10$ (Phase III)

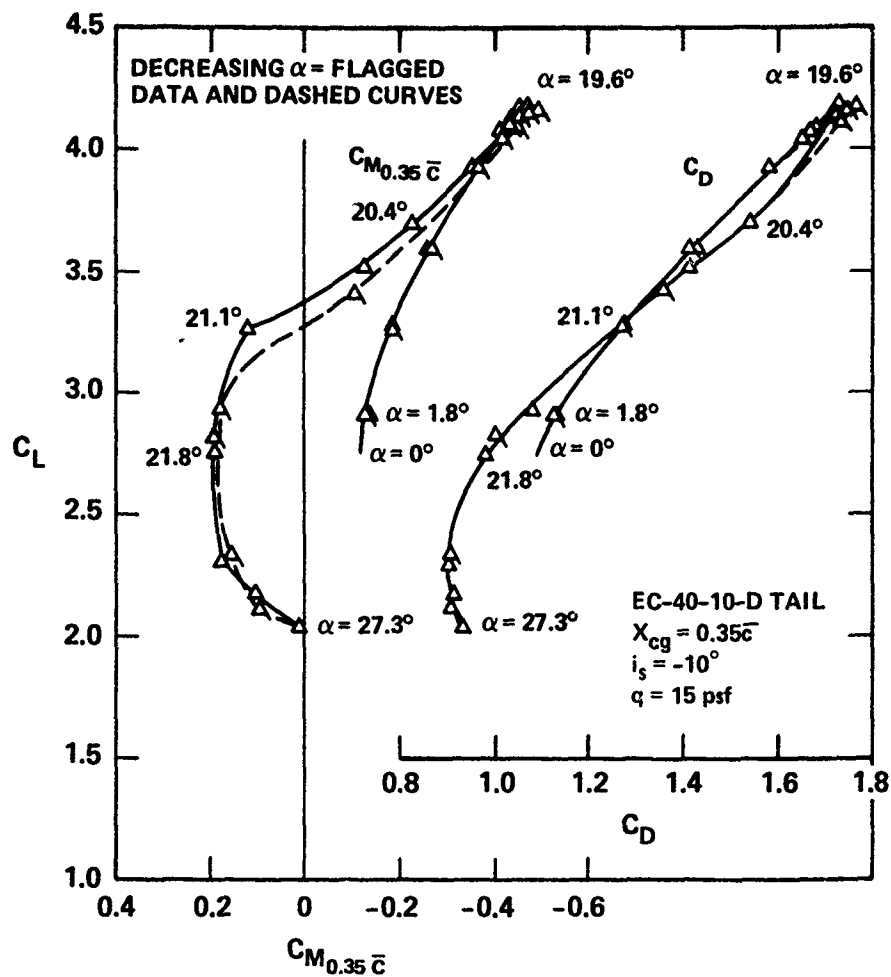


Figure 73 - Post-Stall and Stall Hysteresis
 Effects on Drag and Pitch,
 $C_\mu = 0.30$ (Phase III)

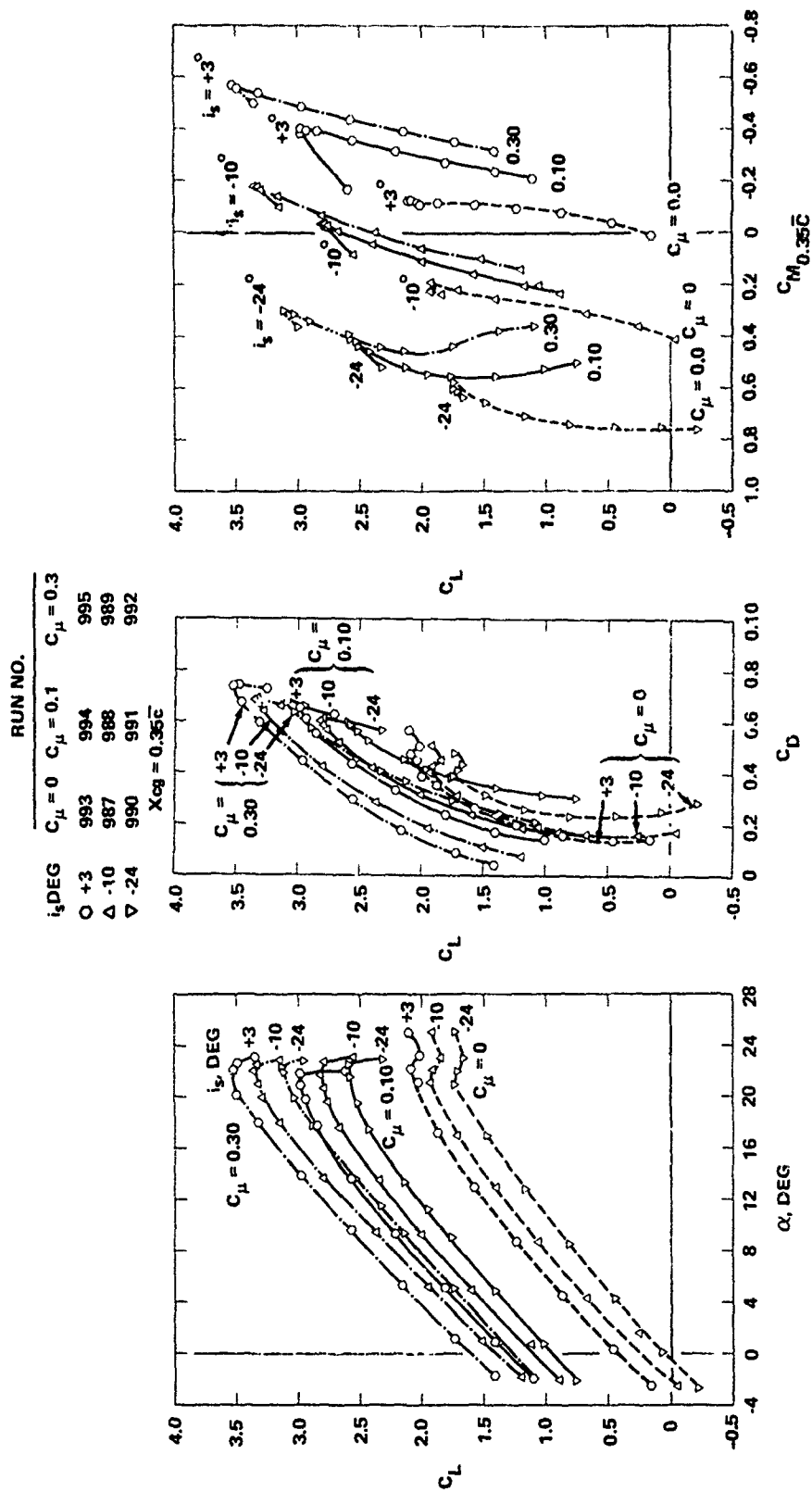


Figure 74 - Effect of Trailing Edge
Splitter Flap on the Final Phase IV
CCW Configuration
(Yaw Jets Removed)

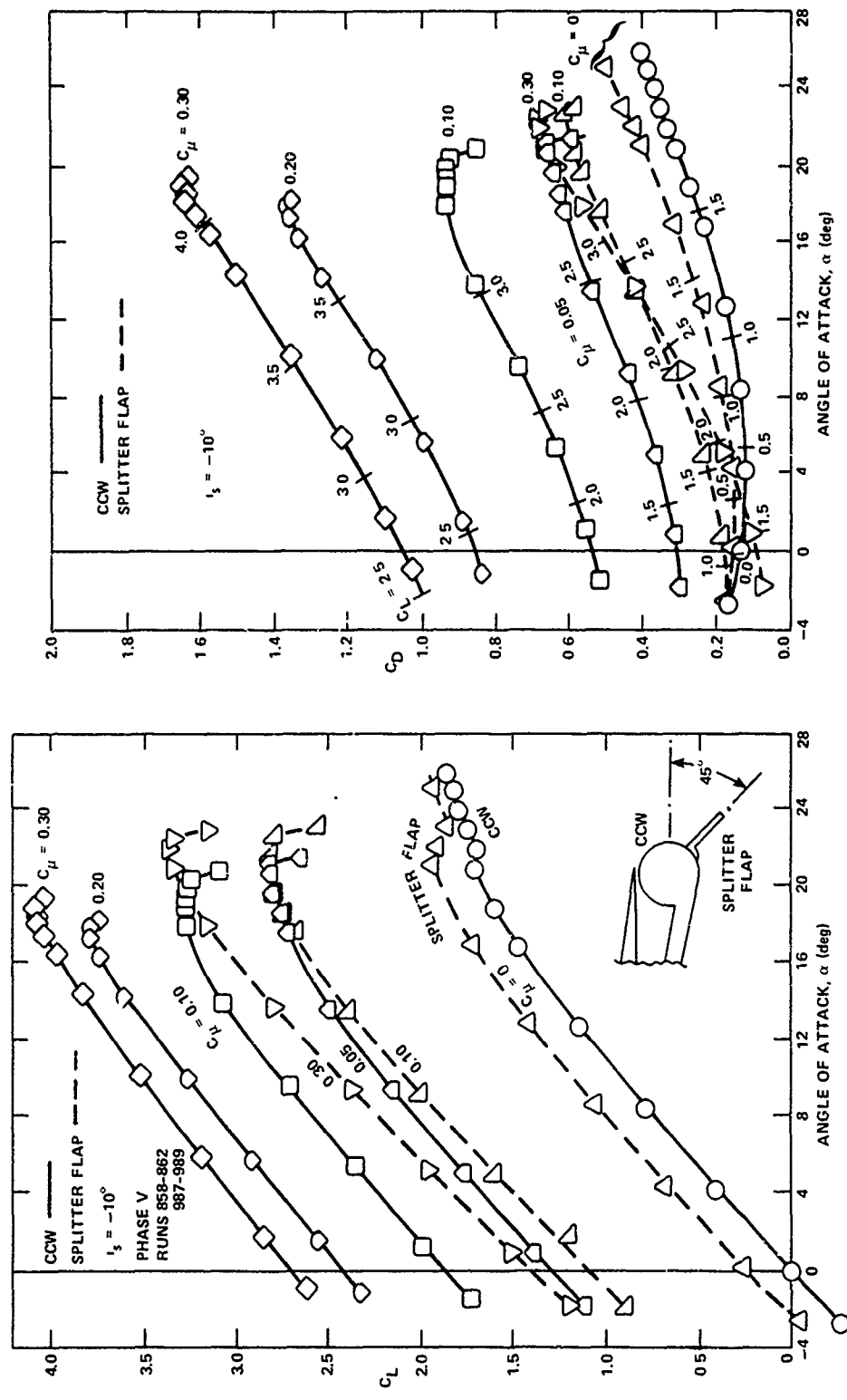


Figure 75 - Comparison of the CCW and Splitter Flap Phase V Configurations

Figure A.1 - 1/8.5-Scale A-6/CCW Model in Phase I Configuration



Figure A.1a - Side View Showing 300-Gallon
Fuel Tanks and Wing Fence Set 2A

Figure A.1 (Continued)

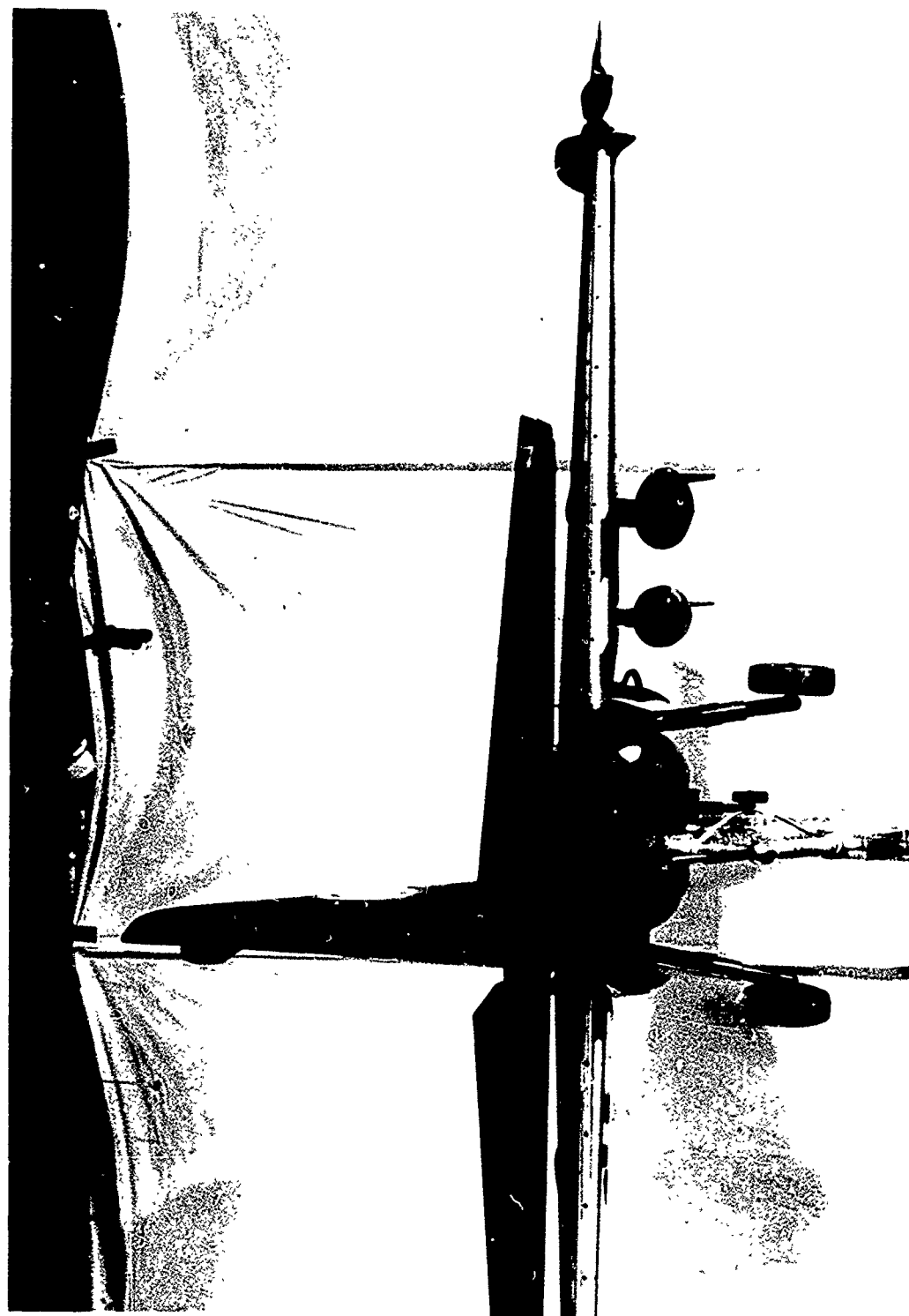


Figure A.1b - Aft View Showing Flow-Through Engine Ducting

Figure A.2 - 1/8.5-Scale A-6/CCW Model in Phase III Configuration



Figure A.2a - 3/4-Aft View

Figure A.2 (Continued)

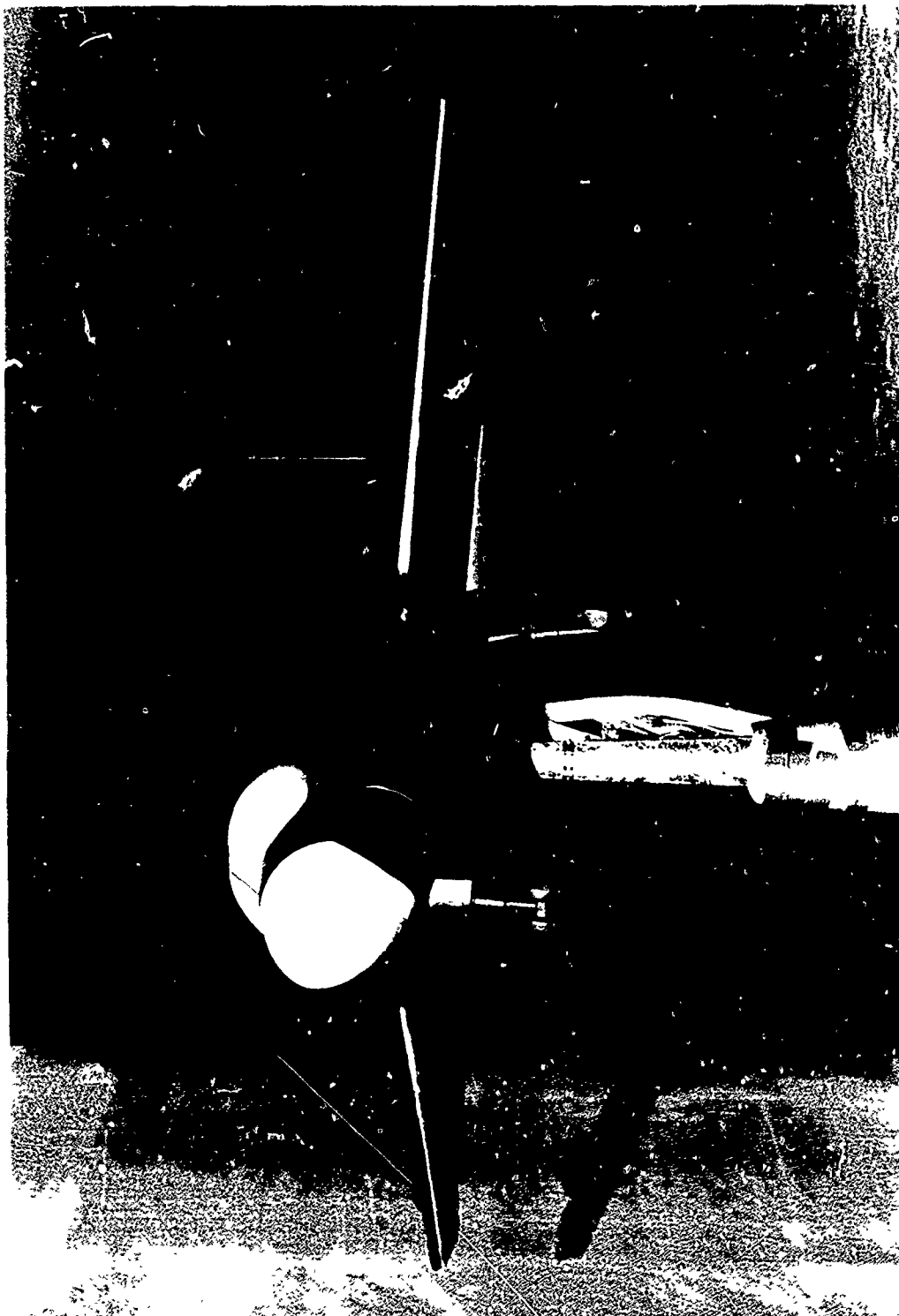


Figure A.2b - Front View

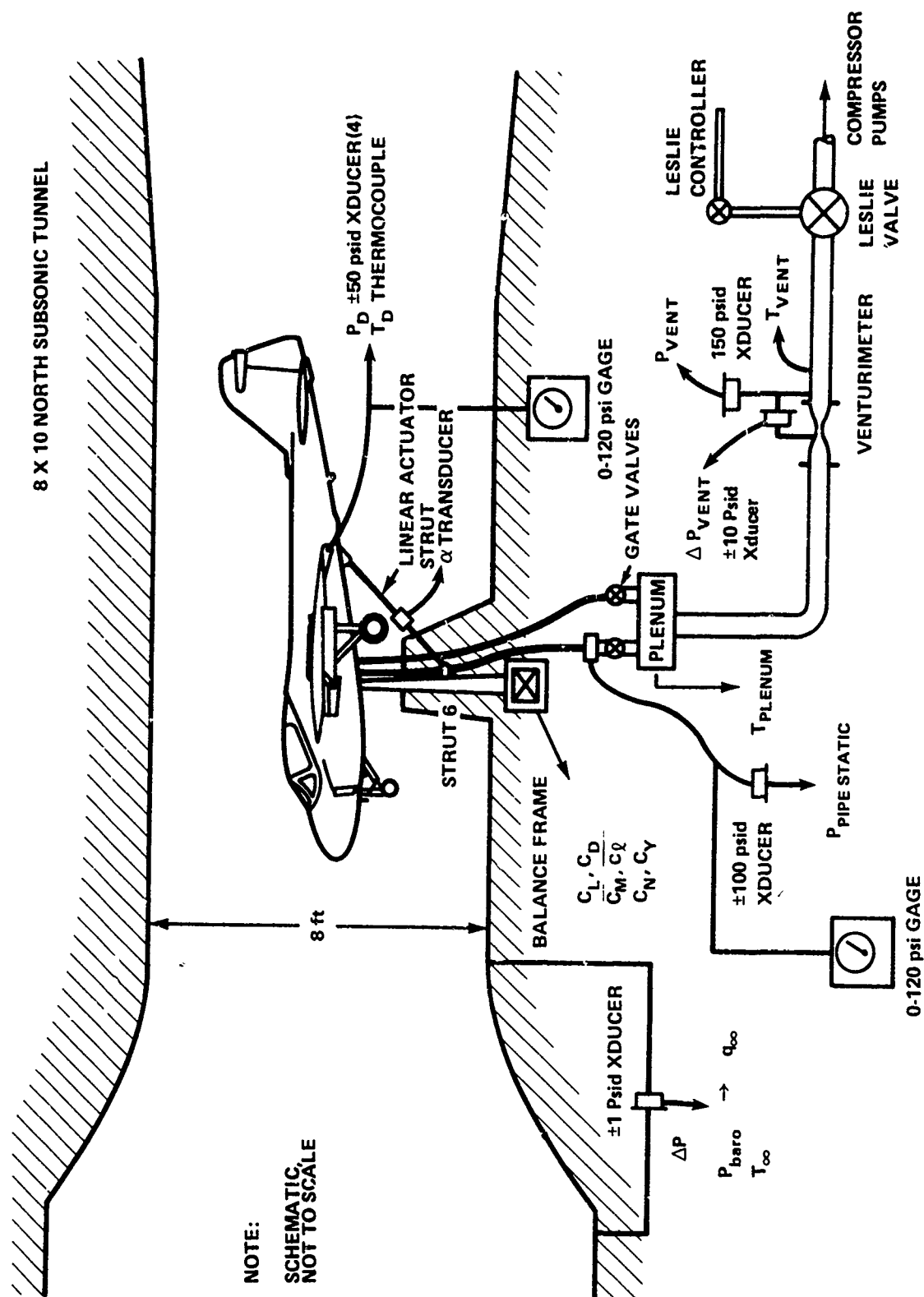


Figure A.3 - A-6/CCW Test Setup and Instrumentation

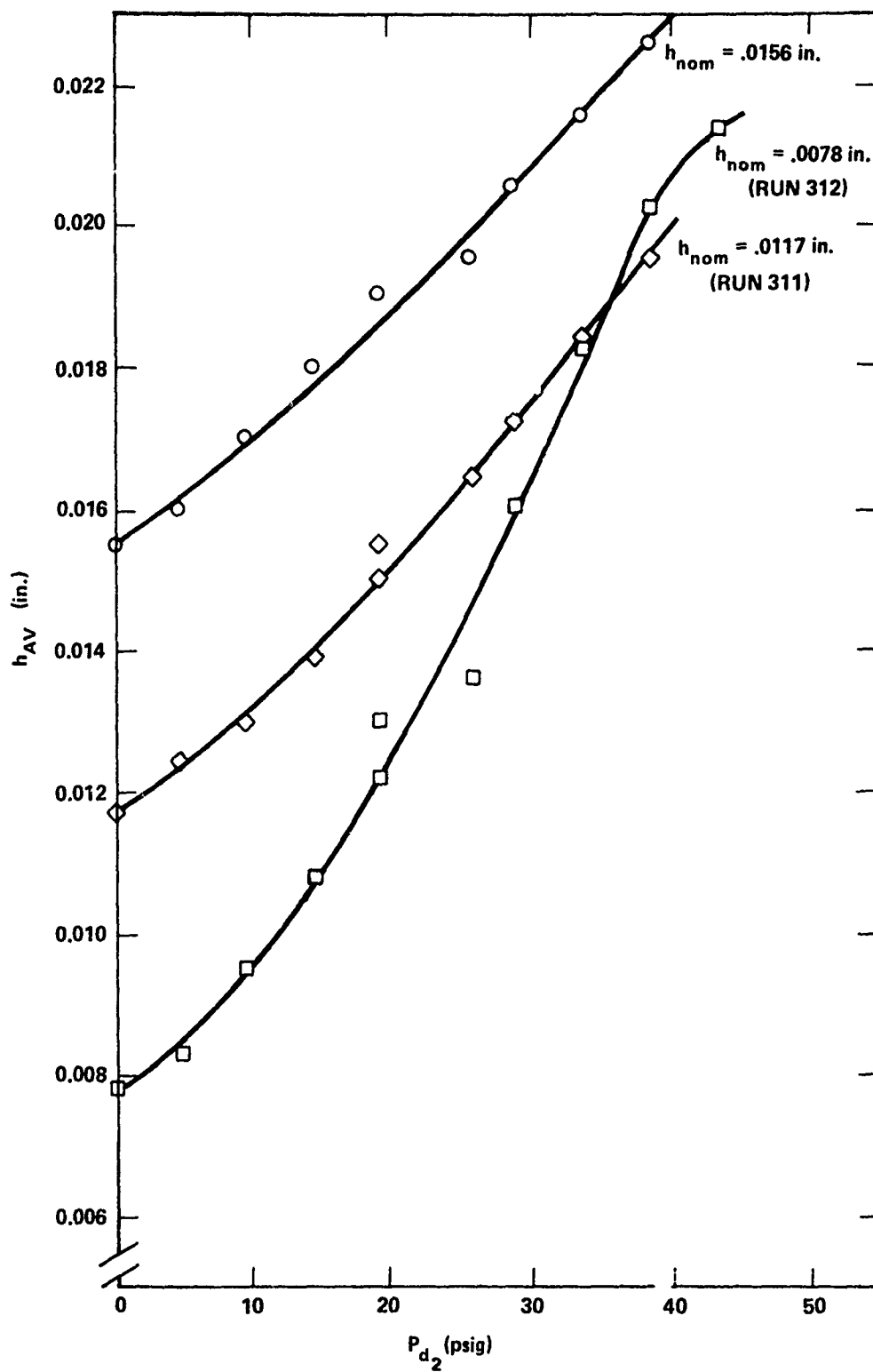


Figure A.4 - Static Calibration of Slot Height
as a Function of Duet Pressure (Phase I)

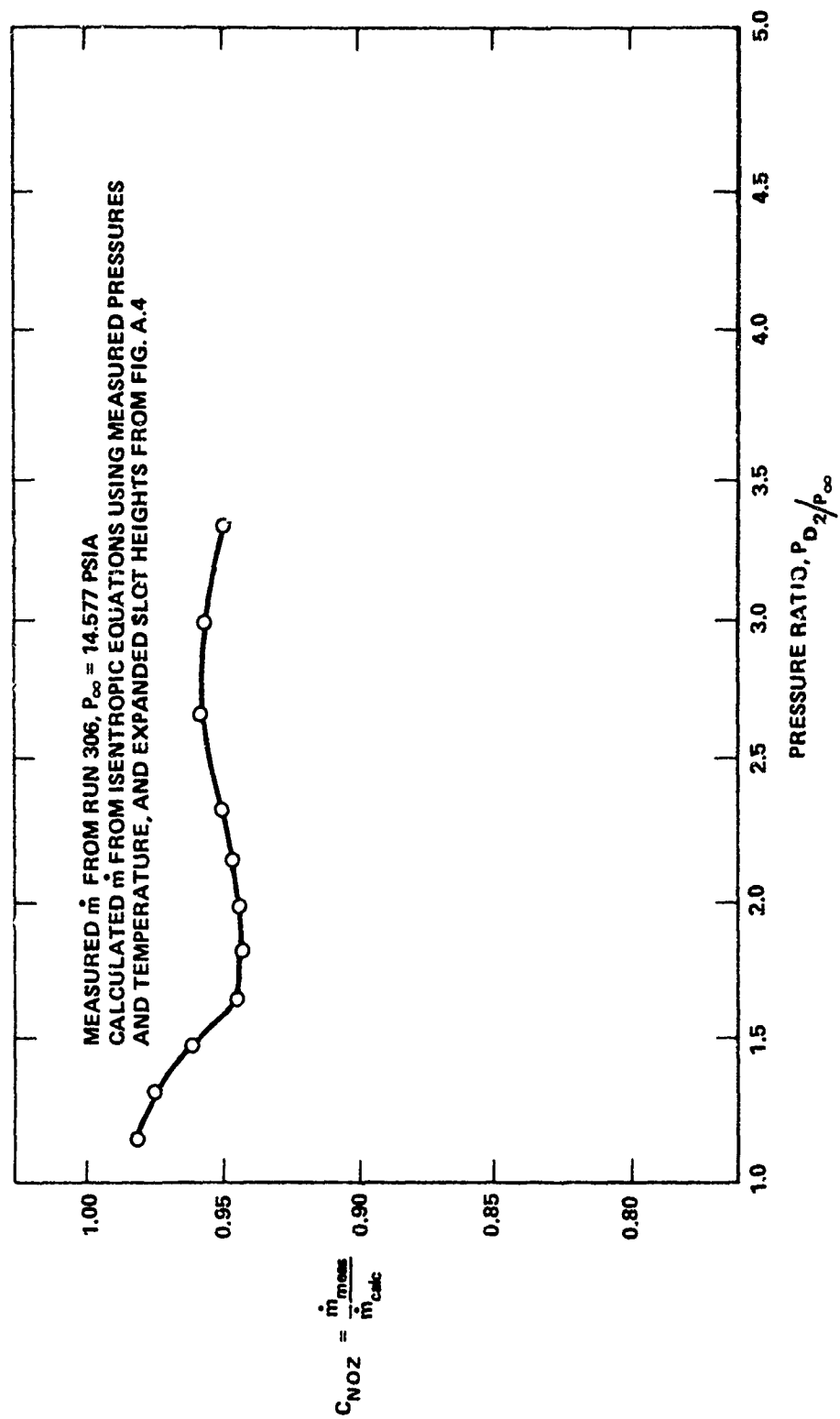


Figure A.5 - Coanda Nozzle Efficiency
 (Phase I)

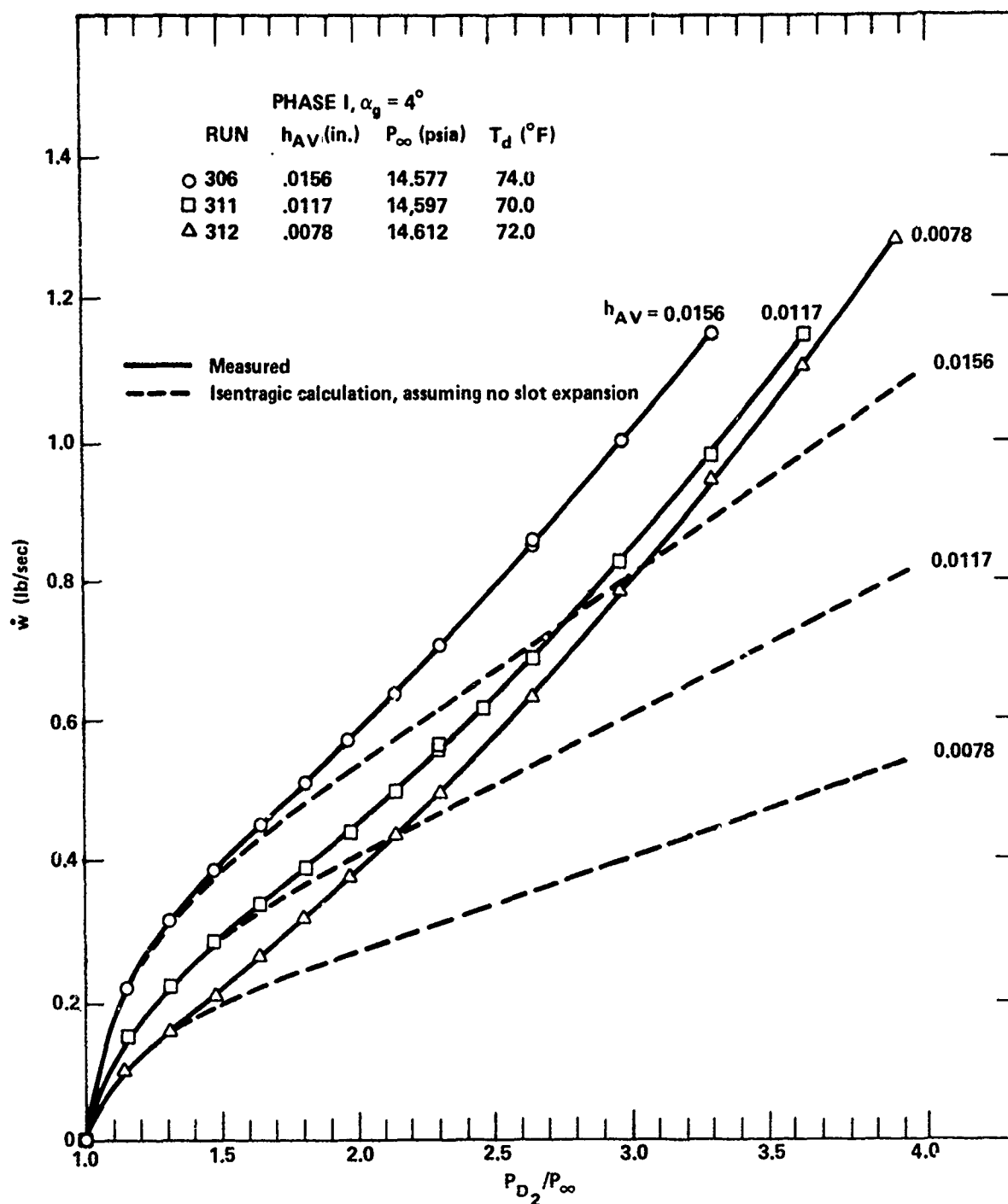


Figure A.6 - Measured and Isentropic Weight Flow as Functions of Slot Height and Pressure Ratio

DTNSRDC ISSUES THREE TYPES OF REPORTS

1. DTNSRDC REPORTS, A FORMAL SERIES, CONTAIN INFORMATION OF PERMANENT TECHNICAL VALUE. THEY CARRY A CONSECUTIVE NUMERICAL IDENTIFICATION REGARDLESS OF THEIR CLASSIFICATION OR THE ORIGINATING DEPARTMENT.
2. DEPARTMENTAL REPORTS, A SEMIFORMAL SERIES, CONTAIN INFORMATION OF A PRELIMINARY, TEMPORARY, OR PROPRIETARY NATURE OR OF LIMITED INTEREST OR SIGNIFICANCE. THEY CARRY A DEPARTMENTAL ALPHANUMERICAL IDENTIFICATION.
3. TECHNICAL MEMORANDA, AN INFORMAL SERIES, CONTAIN TECHNICAL DOCUMENTATION OF LIMITED USE AND INTEREST. THEY ARE PRIMARILY WORKING PAPERS INTENDED FOR INTERNAL USE. THEY CARRY AN IDENTIFYING NUMBER WHICH INDICATES THEIR TYPE AND THE NUMERICAL CODE OF THE ORIGINATING DEPARTMENT. ANY DISTRIBUTION OUTSIDE DTNSRDC MUST BE APPROVED BY THE HEAD OF THE ORIGINATING DEPARTMENT ON A CASE-BY-CASE BASIS.